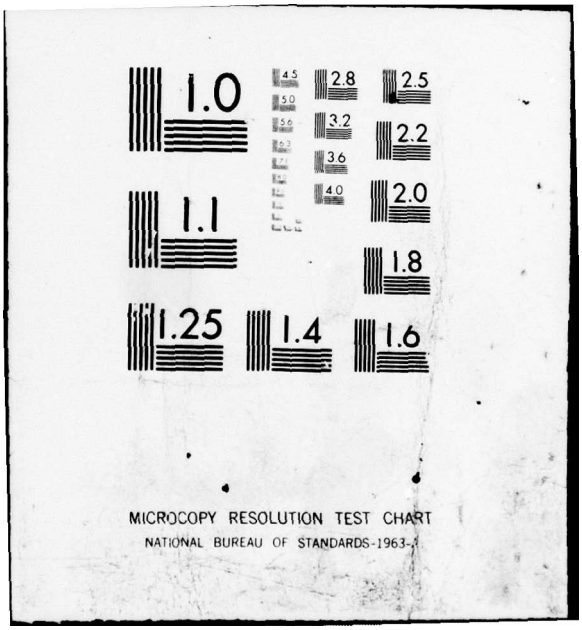
AD-A079 538 RUTGERS - THE STATE UNIV PISCATAWAY NJ COLL OF ENGIN--ETC F/G 11/6
DETERMINATION OF PREFRACTURE FATIGUE DAMAGE.(U)
JAN 80 R PANGBORN, S WEISSMANN, I R KRAMER N00600-77-C-1134
UNCLASSIFIED DTNSRDC-80/006 NL

1 OF 2
AD
A079538




1.0
1.1
1.25
1.4
1.6
1.8
2.0
2.2
2.5
2.8
3.2
3.6
4.0
4.5
5.0
5.6
6.3
MICROCOPY RESOLUTION TEST CHART
NATIONAL BUREAU OF STANDARDS-1963-A

LEVEL A

DTNSRDC-80/006

DAVID W. TAYLOR NAVAL SHIP RESEARCH AND DEVELOPMENT CENTER

Bethesda, Maryland 20084

AD A079538

DETERMINATION OF PREFRACTURE FATIGUE DAMAGE

by

Dr. Robert N. Pangborn
and
Dr. Sigmund Weissmann

College of Engineering
Rutgers University
Piscataway, New Jersey 08854

and

Dr. Irvin R. Kramer

DDC
RECEIVED
JAN 17 1980
A

APPROVED FOR PUBLIC RELEASE; DISTRIBUTION UNLIMITED

DDC FILE COPY

SHIP MATERIALS ENGINEERING DEPARTMENT
RESEARCH AND DEVELOPMENT REPORT

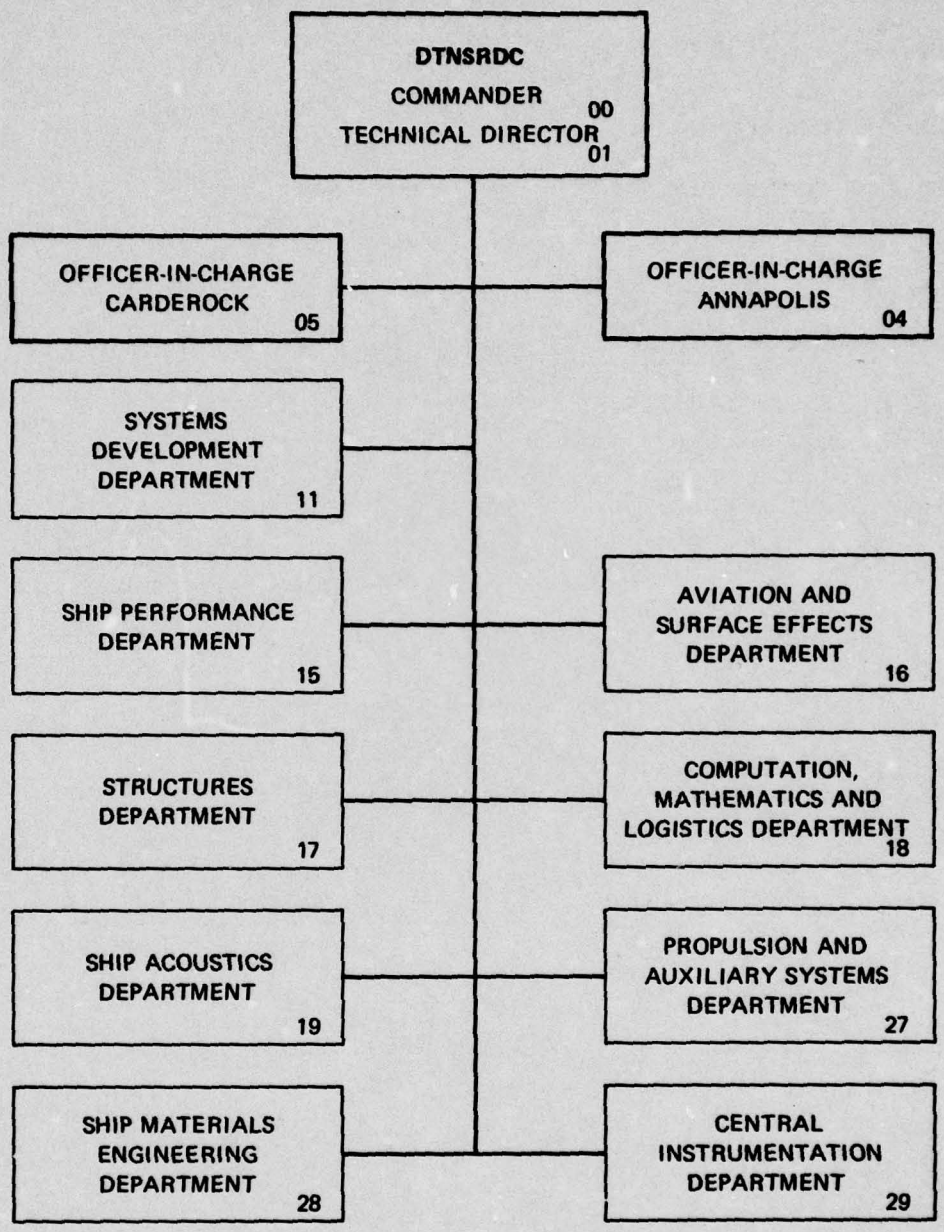
80 1 17 034

January 1980

DTNSRDC-80/006

DETERMINATION OF PREFRACTURE FATIGUE DAMAGE

MAJOR DTNSRDC ORGANIZATIONAL COMPONENTS



NDW-DTNSRDC 3960/43b (Rev. 3-78)
GPO 928 740

nc file

(19) UNCLASSIFIED

SECURITY CLASSIFICATION OF THIS PAGE (When Data Entered)

REPORT DOCUMENTATION PAGE	READ INSTRUCTIONS BEFORE COMPLETING FORM
(18) 1. REPORT NUMBER: DTNSRDC-80/006	2. GOVT ACCESSION NO. (9) 3. RECIPIENT'S CATALOG NUMBER
(6) 4. TITLE (and Subtitle): DETERMINATION OF PREFRACTURE FATIGUE DAMAGE.	5. TYPE OF REPORT & PERIOD COVERED: Research and Development rept.
	6. PERFORMING ORG. REPORT NUMBER
(10) 7. AUTHOR(s): Robert Sigmund Pangborn, Irvin Weissmann (Rutgers University), R. Kramer	(15) 8. CONTRACT OR GRANT NUMBER(s): N00600-77-C-1134 new
9. PERFORMING ORGANIZATION NAME AND ADDRESS: Rutgers University and David W. Taylor Naval Ship R&D Center	10. PROGRAM ELEMENT, PROJECT, TASK AREA & WORK UNIT NUMBERS: Project Element 61152N, Task Area Z40220101, Work Unit 2802-004
11. CONTROLLING OFFICE NAME AND ADDRESS: David W. Taylor Naval Ship R&D Center, Annapolis, Maryland 21402	(11) 12. REPORT DATE: January 1980
	13. NUMBER OF PAGES: 185
14. MONITORING AGENCY NAME & ADDRESS (if different from Controlling Office) (12) 186	15. SECURITY CLASS. (of this report): UNCLASSIFIED
	15a. DECLASSIFICATION/DOWNGRADING SCHEDULE

16. DISTRIBUTION STATEMENT (of this Report)

APPROVED FOR PUBLIC RELEASE; DISTRIBUTION UNLIMITED

(17) ZR0002010 1

17. DISTRIBUTION STATEMENT (of the abstract entered in Block 20, if different from Report)

(16) ZR00201

18. SUPPLEMENTARY NOTES

19. KEY WORDS (Continue on reverse side if necessary and identify by block number)

X-Ray Diffraction
Fatigue
Aluminum
Silicon

20. ABSTRACT (Continue on reverse side if necessary and identify by block number)

X-ray double crystal diffractometry and reflection topography were employed to examine the deformation response of single crystals and Al 2024 alloy specimens. A propensity for preferential work hardening of the surface layers compared to the bulk material was demonstrated for both tensile-deformed and fatigue-cycled metals. The cyclically induced defect distribution with depth from the specimen surface was also investigated as a function of the fraction of fatigue life. This led to a capability for predicting the fatigue life by

(Continued on reverse side)

DD FORM 1 JAN 73 1473 EDITION OF 1 NOV 65 IS OBSOLETE
S/N 0102-014-6601

UNCLASSIFIED
SECURITY CLASSIFICATION OF THIS PAGE (When Data Entered)

393 493

(Block 20 continued)

a nondestructive x-ray diffraction method.

Single crystals of silicon and aluminum pulled in tension exhibited a highly fragmented "debris" layer, extending to about 100 μm in depth, and a core region featuring a much lower excess dislocation density and considerably less lattice breakup and misorientation. A similar decreasing gradient in the excess dislocation density from the surface to the bulk material was obtained for plastically deformed gold monocrystals for which no oxide layer is formed. Aluminum monocrystals cycled in the push-pull fatigue mode revealed a work-hardened surface layer and a transitional subsurface region between the surface layer and the core material. At sufficiently low stress amplitudes, no cyclic damage was introduced in the bulk despite the rapid generation and interaction of dislocations in the surface layer.

Fatigued Al 2024 specimens also exhibited preferential work hardening in the surface layers. The change in excess dislocation densities for the grains located near the surface was shown to follow a three-stage sequence during the fatigue life: an initial rapid increase comprising the first 20 to 25 per cent of the life, a long intermediate period featuring very little change, and a final rapid enhancement during the last 5 to 10 per cent of the life, coinciding with crack initiation and growth. A critical excess dislocation density was associated with fatigue fracture. This critical value was independent of the stress amplitude and varied according to a Petch-type relationship for different grain sizes of the same alloy.

An in-depth analysis, carried out by stepwise removal of the surface layers of cycled specimens, disclosed a plastic response for the grains located in the bulk after about 5 per cent of the fatigue life. The defect structure in the specimen core developed gradually during the cycling. The excess dislocation density for the bulk increased almost linearly as a function of the fatigue life, with a terminal value at failure similar to the critical excess dislocation density for surface grains. The fatigue process was interpreted as a rapid work hardening of the surface to form a barrier to dislocation egression and rearrangement. The dynamic interplay between the surface barrier and the eventual plastic response activated in the bulk leads to a critical defect accumulation at the surface and incipient cracking.

When the fatigue process was interrupted prior to failure and the surface layer was removed, a striking recovery phenomenon was observed throughout the specimen cross section during subsequent cycling. The bulk defect structure was thus shown to be extremely unstable in the absence of the restraining influence imposed by the work-hardened surface layer. The extension of the fatigue life of metals by judicious surface removal was ascribed primarily to the elimination of the surface barrier rather than to the removal of microcracks.

The fatigue response at various depths from the surface was also investigated nondestructively by employing x-ray radiations with differing penetration capabilities. The excess dislocation density of grains located up to 300 μm in depth was examined using molybdenum radiation and found to vary linearly with the fatigue life. This steep linear dependence, in conjunction with the early life saturation behavior of surface-grain densities measured with copper radiation, provided a new criterion for predicting accurately the fatigue life and failure.

TABLE OF CONTENTS

	Page
LIST OF FIGURES	v
LIST OT TABLES	ix
ABSTRACT	1
ADMINISTRATIVE INFORMATION	2
1. INTRODUCTION	3
A. AN HISTORICAL PERSPECTIVE	3
1. Evidence of Surface Layer Work Hardening	5
2. Role of the Surface Layer in Metal Fatigue	11
3. Prediction of Fatigue Failure	27
B. X-RAY DEFECT ANALYSIS AND APPLICATIONS TO FATIGUE	31
1. A "Microstructural" Approach to Fatigue Life Prediction	32
2. Double Crystal Diffractometry and Topographic Techniques	37
II. OBJECTIVES	40
A. MICROSTRUCTURAL CONFIRMATION OF SURFACE LAYER WORK HARDENING	40
B. TESTING THE "SURFACE BARRIER MODEL" FOR FATIGUE DEFORMATION	41
C. DEVELOPMENT OF NEW CRITERIA FOR FATIGUE FAILURE PREDICTION	42
III. EXPERIMENTAL PRODEDURE	43
A. SINGLE-CRYSTAL STUDIES	43
1. Tensile Deformation	43
2. Dynamic Testing	45
3. X-ray Diffraction Analysis	47
B. Al 2024 ALLOY STUDIES	51
1. Incremental Fatigue Cycling	51
2. Damage Gradients from Surface to Bulk	53
3. Surface Removal and Recycling	54
4. X-ray Diffraction and Surface Microscopy	54
5. Nondestructive X-ray Analysis in Depth	60

Page

IV. RESULTS 63

A. SINGLE-CRYSTAL STUDIES 63

1. X-ray Rocking Curves of Tensile Deformed Si, Al, and Au crystals 63

2. Rocking Curves and Topography of Tensile Deformed Al Crystals 69

3. Measurement and Characterization of Fatigue Damage in Al Crystals 71

B. Al 2024 ALLOY STUDIES 73

1. Rocking Curve Analysis of the Surface Layer During Incremental Fatigue 73

2. Elucidation of the Fatigue Induced Surface Morphology 85

3. Response of the Surface and Bulk to Fatigue Cycling 92

4. Effects of Fatigue Cycling in the Absence of the Surface Layer 103

5. Effect of Grain Size and Radiation Type on Progressive Fatigue Curves 107

V. DISCUSSION 113

A. SINGLE-CRYSTAL STUDIES 113

1. Preferential Surface Layer Work Hardening Induced by Plastic Strain 113

2. Structural Response of the Surface Layer and Bulk to Fatigue Cycling 126

B. Al 2024 ALLOY STUDIES 129

1. Critical Surface Layer Work Hardening as a Precursor to Cyclic Failure 129

2. Influence of the Bulk Response on the Fatigue Life and Failure 133

3. Instability of the Induced Defect Structure of the Bulk 138

Page

4. Prediction of Fatigue Failure by X-ray Diffraction Analysis. 143

VI. CONCLUSIONS. 149

A. IMPLICATIONS OF SURFACE WORK HARDENING: THE SURFACE BARRIER CONCEPT 149

B. IMPORTANCE IN METAL FATIGUE: THE PREDICTION OF FATIGUE FAILURE 151

VII. SUGGESTIONS FOR FUTURE WORK 153

APPENDIX A - DEPTH OF PENETRATION 155

APPENDIX B - HORIZONTAL AND AZIMUTHAL BROADENING. 159

APPENDIX C - DEBYE PATTERN AND ROCKING CURVE ANALYSIS 163

REFERENCES. 167

LIST OF FIGURES

1 - Determination of surface layer stress induced by tensile deformation. 7

2 - Evidence of preferential surface work hardening. 12

3 - Dependence of the etching rate on the distance from the specimen surface for fatigue cycling of annealed steel 19

4 - Determination of the surface layer stress induced by fatigue, and its change with the number of cycles under variable amplitude loading. 20

5 - Schematic illustration of the changes in the half-value breadth, Vicker's hardness, and compressive residual stress at the specimen surface during the fatigue life for cantilever-type plate bending of unnotched steel 24

6 - Distribution of b/B, H_v, and σ_r with depth from the surface. 25

7 - Changes in the lattice strain, $\Delta d/d$ (from the radial breadth), total misorientation, β (from the tangential breadth), and the number of subgrains, m (from the number of subdivided spots) during reversed bending fatigue of notched steel specimens. 36

Page

8 - Specimen configurations employed in the tensile tests of single crystals 44

9 - Specimen configuration and grip assembly employed in the fatigue investigations of Al single crystals and Al 2024 alloy. 46

10 - X-ray double crystal diffractometer for single crystal analysis 48

11 - X-ray double crystal diffractometer for polycrystalline metals 56

12 - X-ray rocking curve profiles of tensile deformed silicon single crystal 65

13a - Rocking curve halfwidths as a function of depth from the specimen surface for a silicon single crystal deformed by uniaxial tension 66

13b - Rocking curve halfwidths as a function of depth from the specimen surface for an aluminum single crystal deformed by uniaxial tension 67

13c - Rocking curve halfwidths as a function of depth from the specimen surface for a gold single crystal deformed in tension. 68

14 - X-ray rocking curve profile correlated to topographic images at successive angular positions along the reflecting range for tensile deformed aluminum single crystal 70

15 - Halfwidth depth profile for an aluminum single crystal, fatigued in the high-cycle range, tension-compression mode 74

16 - S-N curve for Al 2024, batch A, fatigued in the push-pull mode 76

17 - Detail of the grain reflections for Al 2024 prior to fatigue 78

18 - Detail of the grain reflections of Al 2024 cycled to 30.4% of the fatigue life with a stress amplitude of $\pm$200 MPa. 78

19 - Detail of the grain reflections of Al 2024 cycled to 95.7% of the fatigue life with a stress amplitude of $\pm$200 MPa. 79

Page

20 - Debye pattern for fatigue-cycled Al 2024 alloy showing azimuthal limits for grain reflection analysis. 79

21 - Change in the surface halfwidths with progressive fatigue cycling of Al 2024 alloy, batch A 81

22 - Surface halfwidths as a function of the fatigue life for Al 2024, batch A, cycled at ±200 MPa. 83

23 - Change in the surface halfwidths as a function of fraction of the fatigue life for Al 2024, batch A, cycled at stress amplitudes corresponding to 1.0, 0.75, and 0.50 $\sigma_{p.l}$ 84

24 - Schematic rocking curves (above) for actual grain reflection arrays (below) recorded during controlled rotation of Al 2024 alloy specimens 86

25 - Scanning electron micrograph of the flat gage region especially prepared by spark-erosion planing, prior to electropolishing and testing of the specimen. 87

26 - Light micrographs of unetched Al 2024 specimens cycled at ±200 MPa to stages II and III of the fatigue life. 88

27 - Optical micrographs of etched Al 2024 specimens showing the comparative degrees of slip activity in stages II and III of the life. 89

28 - Optical micrographs of etched Al 2024 specimens showing intragranular and transgranular slip traces induced by fatigue cycling. 90

29 - SEM photomicrograph of an Al 2024 specimen cycled to 95% of the fatigue life at ±200 MPa 91

30 - SEM image of high-relief slip band structure at 0.95 N/N_f 93

31 - High-magnification SEM photomicrographs of an Al 2024 specimen cycled to 95% of the fatigue life at ±200 MPa, unetched 94

32 - SEM image of the fracture surface for an Al 2024 fatigue specimen cycled at ±200 MPa 95

33 - Detail of the fracture surface by SEM photomicroscopy 96

Page

34 - Debye pattern spot arrays exhibiting the reflection range of Al 2024 grains prior to cycling. 98

35 - Debye pattern spot arrays exhibiting the reflection range of grains located at the surface of cycled Al 2024 specimens 99

36 - Debye pattern spot arrays exhibiting the range of reflection for cycled Al 2024 grains after removal of a 100 μm layer from the specimen surface by electropolishing 100

37 - Depth profiles (β vs depth, χ) for various fractions of the total fatigue life of Al 2024 specimens. 102

38 - Effect of recycling on the (new) surface halfwidths after removal of a 400 μm surface layer from prefatigued specimens 105

39 - Composite diagram for Al 2024 specimens given prior cycling to 75 and 95% of their fatigue life at ±200 MPa, followed by a surface removal and recycling procedure (A) and (B), and either continued cycling or depth profile analysis (C). 106

40 - Comparison of progressive fatigue curves for 44- and 33-μm grain size Al 2024, cycled at stress amplitudes equivalent to their respective static proportional limits. 109

41 - Comparison of progressive fatigue curves for Al 2024, batch B, using x-ray radiations with different maximum penetration depths. 111

42a - Experimental gradients of the excess dislocation density with depth from the surface for tensile deformed monocrystals. 116

42b - Ratios of the excess dislocation density at various depths, χ, to the constant bulk density, ρ_i, for tensile deformed monocrystals 117

42c - Comparison of linearized excess dislocation gradients from the surface to bulk for tensile deformed Si, Al, and Au single crystals. 118

43 - Correlation of x-ray rocking curves, crystal morphology, and topographic images. 124

Page

44 - Comparative changes in surface (broken line) and bulk (solid line) halfwidths as a function of fatigue life 136

45a - Comparison of excess dislocation densities measured during the fatigue life by analysis with copper and molybdenum radiations 145

45b - Comparison of the change in average dislocation densities during the fatigue life determined by integration of the depth profiles in Figure 37. 146

A1 - Schematic diagram of radial penetrations for molybdenum, copper, and chromium radiations 158

LIST OF TABLES

1 - Measured X-ray Rocking Curve Halfwidths, Halfwidth Ratios, and Calculated Excess Dislocation Densities for the Surface Layers and Bulk of Tensile Deformed Single Crystals. 64

2 - X-ray Rocking Curve Data as a Function of Depth From the Surface for Cylindrical Aluminum Monocrystals; [100] Loading Axis, (100) Reflection. 73

3 - Comparison of Some Morphological, X-ray Diffraction, Monotonic, and Fatigue Properties of the Two Al 2024 Alloy Stocks. 75

4 - Rocking Curve Data for Fatigue Studies of Al 2024, Batch A 80

5 - X-ray Rocking Curve Data for Depth Profile and Recycling Studies of Al 2024, Batch A 101

6 - X-ray Rocking Curve Halfwidths Recorded for Cycled Al 2024, Batch B, Employing Cu, Mo, and Cr Incident Radiation; $\sigma_a = \pm 280$ MPa. 108

7 - Comparison of Relative Halfwidth Expansions in the Surface Layer and Bulk Material During Incremental Fatigue Cycling of Al 2024 Specimens. 135

A.1 - Maximum Radial Penetrations of Molybdenum, Copper, and Chromium Radiations for Cylindrical Al 2024 Specimens 157

C.1 - Comparative Intensity Ratios for Various Radiation and Monochromator Combinations. 162

ABSTRACT

X-ray double crystal diffractometry and reflection topography were employed to examine the deformation response of single crystals and Al 2024 alloy specimens. A propensity for preferential work hardening of the surface layers compared to the bulk material was demonstrated for both tensile deformed and fatigue cycled metals. The cyclically induced defect distribution with depth from the specimen surface was also investigated as a function of the fraction of fatigue life. This led to a capability for predicting the fatigue life and failure by a nondestructive x-ray diffraction method.

Single crystals of silicon and aluminum pulled in tension exhibited a highly fragmented "debris" layer extending to about 100 μm in depth, and a core region featuring a much lower excess dislocation density and considerably less lattice breakup and misorientation. A similar decreasing gradient in the excess dislocation density from the surface to bulk was obtained for plastically deformed gold monocrystals for which no oxide layer is formed. Aluminum monocrystals cycled in the push-pull fatigue mode revealed a work hardened surface layer, and a transitional subsurface region between the surface layer and the core material. At sufficiently low stress amplitudes, no cyclic damage was introduced in the bulk, despite the rapid generation and interaction of dislocations in the surface layer.

Fatigued Al 2024 specimens also exhibited preferential work hardening in the surface layers. The change in excess dislocation densities for the grains located near the surface was shown to follow a three-stage sequence during the fatigue life: an initial rapid increase comprising the first 20 to 25 percent of the life, a long intermediate period featuring very little change, and a final rapid enhancement during the last 5 to 10 percent of the life, coinciding with crack initiation and growth. A critical excess dislocation density was associated with fatigue fracture. This critical value was independent of the stress amplitude, and varied according to a Petch-type relationship for different grain sizes of the same alloy. An in-depth analysis, carried out by stepwise removal of the surface layers of cycled specimens, disclosed a plastic response for the

Accession For
NTIS GRA&I
DDC TAB
Unannounced
Justification
By
Distribution/
Availability Codes
Dist | Avail and/or special
A

grains located in the bulk after about 5 percent of the fatigue life. The defect structure in the specimen core developed gradually during the cycling. The excess dislocation density for the bulk increased almost linearly as a function of the fatigue life, with a terminal value at failure identical to the critical excess dislocation density for surface grains. The fatigue process was interpreted as a rapid work hardening of the surface to form a barrier to dislocation egression and rearrangement. The dynamic interplay between the surface barrier and the eventual plastic response activated in the bulk leads to a critical defect accumulation at the surface and incipient cracking.

When the fatigue process was interrupted prior to failure and the surface layer was removed, a striking recovery phenomenon was observed throughout the specimen cross section during subsequent cycling. The bulk defect structure was thus shown to be extremely unstable in the absence of the restraining influence imposed by the work hardened surface layer. The extension of the fatigue life of metals by judicious surface removal was ascribed primarily to the elimination of the surface barrier, rather than to the removal of microcracks.

The fatigue response at various depths from the surface was also investigated nondestructively by employing x-ray radiation with differing penetration capabilities. The excess dislocation density of grains located up to 300 μm in depth was examined using molybdenum radiation, and found to vary linearly with the fatigue life. This steep, linear dependence, in conjunction with the early life saturation behavior of surface-grain densities measured with copper radiation, provided a new criterion for predicting accurately the fatigue life and failure.

ADMINISTRATIVE INFORMATION

This investigation is part of an in-house research program at the David W. Taylor Naval Ship Research and Development Center in cooperation with Professor S. Weissmann and Dr. R. Pangborn of Rutgers University. It was conducted under Task ZR 002-0101, Work Unit 2802-004.

I. INTRODUCTION

A. AN HISTORICAL PERSPECTIVE

In the past several decades, the contribution of the plastic response both in the surface layer and in the bulk material to the mechanical behavior of metals has become a subject of considerable interest and controversy. Such interest derives, to a great extent, from the vast improvement and diversification of experimental techniques which now permit the correlation of microstructural characteristics to the macroscopic flow and fracture behavior. However, despite the commonly evoked opinion that the free surface exerts a strong influence on the microstructural response of the metal, and therefore plays an important role in determining its mechanical properties, no comprehensive and indisputable explanation of the surface effect has yet evolved.

The early investigations of fatigue failure in metals provided substantial evidence of the surface sensitivity of mechanical behavior. Surface studies revealed the formation of slip bands and their topological development into intrusions and extrusions associated with subsequent crack initiation and eventual failure[1-4]*. Other fatigue investigations focused on the microstructural developments in metals during repeated stressing[5-9]. During the mid-1960's, many studies were made to relate the fatigue induced defect structure with the slip morphology exhibited on the surface, often with conflicting results[10-14]. In the early 1970's, Grosskreutz suggested a program to integrate the elucidation of the topographical deformation characteristics and the microstructural mechanisms controlling them[15,16]. His hope, though still unrealized, was to define a universal rationale by which to describe fatigue behavior, and then to use it in both the control of fatigue resistance and the prediction of fatigue failure.

While surface effects were diagnosed early on as a primary factor in fatigue performance, the origin of surface effects in crystal plasticity under static loading conditions has also been recognized as a subject of fundamental and practical importance[17]. Elucidation of the intrinsic

---

*A complete listing of references is given on page 165.

response of the surface layer itself in stress relaxation or creep experiments was vital to an understanding of the synergistic effect between the surface and the surrounding environment. The mechanical performance of metals subject to oxide formation, reduced pressures or vacuum, aggressive or inert atmospheres, and surface-active or corrosive solutions has been reviewed in terms of the changes produced in both the macroscopic flow characteristics and the microstructural development[18].

There is still much to be learned regarding the role of the surface layer in determining the bulk mechanical properties of metals and alloys. The explanation and further improvement of surface treatments which prevent or delay failure are contingent on positive diagnosis of the causes of failure, which requires that the inconsistencies inherent to many previous studies be avoided. These derive from several principal sources:

1. the inadequacy of the experimental tool employed in the analysis to provide information concerning the microstructural differences between the surface and bulk;

2. the reliance on qualitative or indirect methods for characterizing the respective surface and bulk responses to the deformation process; and

3. the use of deformation modes, such as bending, which produce a nonuniform stress and strain distribution from the surface to bulk, and therefore obscure the "intrinsic" differences in response which may or may not occur if the loading were uniformly distributed over the cross section.

The ensuing discussion will apply to the three principal phases proposed to comprise the present investigation. The first of these constitutes a fundamental, quantitative analysis of the role of the surface layer in simple, tensile deformation. The second phase involves an evaluation of the surface effect and its influence on the bulk material, related to a more complex form of deformation, that of fully reversed, axial fatigue. The final phase explores the capability of x-ray diffraction and topography to generate evidence of cyclically accrued "damage," which might be used in the prediction of the fatigue life and ultimate failure.

1. Evidence of Surface Layer Work Hardening

a. Experimental Observations. The response of the surface layer and bulk material to plastic deformation has been the subject of numerous investigative efforts, but of fairly limited agreement. The primary interpretive divergence of the studies was related to whether the surface layer or the core material "work hardens" to a greater extent during the deformation process. Some investigators studying the deformation behavior of copper single crystals claimed to have obtained evidence that the core region of the crystals work hardens preferentially[19-22]. This conclusion was based on a combination of theoretical arguments and experimental results regarding the stress distribution, on TEM analysis of thin foils prepared at different depths from the crystal surface, and on interpretation of high-resolution load-strain curve analysis of prestressed crystals. Other investigators, however, using identical experimental techniques to study uniaxially strained aluminum single crystals, concluded that the surface layers experience preferential work hardening[23,24]. In addition, measurements of etch pit density and of microhardness and x-ray diffraction analysis have been shown to support the surface work-hardening mechanism in both single and polycrystalline metals[25-28].

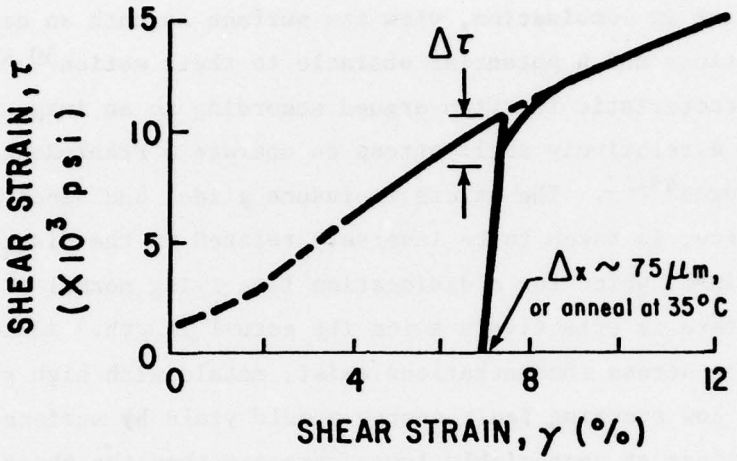
The reasons for the conflicting conclusions were many. First, in most cases, the analysis of the relative flow stress, dislocation density, or hardness of the surface and core material was performed after unloading. Only the stress-strain analysis during continuous surface layer removal performed by Kramer and others is exempt from this generalization[29-32]. According to Fourie[33], if, on initial pulling, the flow stress was assumed to be sufficiently higher in the core, then on unloading, the elastic stress in the bulk would put the surface layer in residual compression. This would lead to reverse plastic flow when the reverse stress was exceeded. The crucial question with regard to reloading was: Does the prior sequence of plastic flow in the surface layer lead to subsequent work hardening in this region, as proposed by Brydges[34], or does the surface flow stress remain significantly lower than that of the

core, as contended by Fourie himself? The interpretation of experimental results was often clouded by such factors as (a) the effects of surface relaxation by dislocation egression after unloading, but prior to flow stress analysis, (b) the dependence of the flow stress magnitude on the size of the specimen, which is obviously altered by the polishing or slicing necessary for relative flow stress determination, and (c) the effect of superimposed bending moments produced by the compressive stress gradient during these operations. All of these factors, as enumerated by Kramer[35], contributed to the difficulty of trying to isolate the surface and bulk regions without altering them in the process, and might possibly induce erroneous results indicating a "softer" core characteristic.

In 1961 Kramer first reported his finding of nonuniformity in work hardening over the cross section[29]. The "hard" surface concept evolved from experiments demonstrating a reduction in the work hardening rate when metal was removed electrochemically during the plastic straining. To measure the contribution of the surface layer to the overall plastic response of the specimen, a sequence involving a prelaoading and unloading step, followed by surface layer removal or annealing treatment and reloading, was prescribed. The resulting decrease in the initial flow stress on reloading from its original terminal, value of the preload step was ascribed to the elimination of the plastic resistance plastic resistance afforded by the work hardened surface (Figure 1). The behavior was found typical of several fcc single crystal metals including gold[31], and of polycrystalline aluminum, copper, gold, and iron[36]. Etch pit measurements on polycrystalline copper by Vellaikal and Washburn revealed a higher dislocation density at the surface[37]. Kolb and Macherauch made a similar observation for polycrystalline nickel[38]. Later investigations by Kramer reported both a decrease in the apparent activation energy with polishing during plastic deformation and an increase in activated volume as the polishing rate was increased[39,40]. For single crystals and pure metals, the activation volume could have increased only if the dislocation density was caused to decrease.

Since a preponderance of the experimental evidence appears to favor preferential surface work hardening, some of the mechanistic models and

(a)



(b)

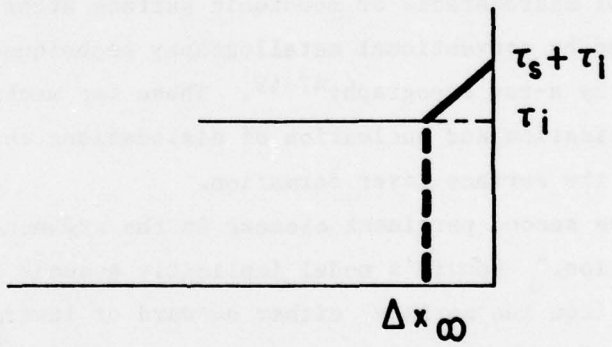


Figure 1. Determination of surface layer stress induced by tensile deformation: (a) decrease in the initial flow stress after removal of the surface layer or annealing at 35°C, for an aluminum single crystal pulled at 3°C; and (b) comparative shear stress for flow in the surface and bulk regions.

related research supporting the concept are introduced in the following section.

b. Surface Layer Work Hardening Mechanisms. Many conceptual models for dislocation generation and interaction have been proposed to explain the "hard" surface layer phenomenon. Most of these models particularly when they act in combination, view the surface as both an easy source of dislocations and a potential obstacle to their motion[30,41]. The former characteristic is often argued according to an image force concept, predicting a relatively small stress to operate a Frank-Read-type or Fischer source[42-45]. The stress to induce glide, and hence operation of the source, is taken to be inversely related to the distance between pinning points, which for a dislocation line lying normal to and unpinned at the surface is effectively twice its actual length. Additionally, when surface stress concentrations exist, metals with high surface energy and low stacking fault energy should yield by surface nucleation of dislocations at appreciably lower stresses than the theoretical stress for bulk or catastrophic yield[46]. Such stress raisers may be on the order of microdefects or monotonic surface steps. These are not usually resolved by conventional metallography techniques, but are revealed easily by x-ray topography[47-49]. These two mechanisms of preferential multiplication and nucleation of dislocations constitute the first step toward the surface layer formation.

The second pertinent element in the argument is essentially one of "retention." Fourie's model implicitly assumes that the dislocations escape from the surface, either outward or inward, faster than they are generated. The "hard" surface concept, on the other hand, predicts that the cumulative effects of enhanced dislocation generation and subsequent pileup prevent egression, and lead instead to greater work hardening in the surface layer. One theoretical analysis of pileup formation and growth in a crystal with a random distribution of growth dislocations suggests that the rate of multiplication by surface sources exceeds considerably that due to internal sites[50]. It would be reasonable to assume that the converse would also hold. Aside from the contention that the close proximity of defects associated with the high surface

concentration acts by itself to increase the potential for interaction and work hardening, other explanations are equally admissible. The pileup formation has been ascribed to a variety of mechanisms which inhibbit egression at the free surface and heighten the interaction potential. For instance, image forces may propel unstable dislocations located near the surface in an outward direction, where they experience the action of the displacement field due to relaxation of the surface lattice[51,52]. Continued glide would then require an increase in the Burgers vector and the eventual separation into partials. When immobile dislocation tails are left behind, they prevent the emergence of dislocations generated in, and egressing from, the bulk[52]. Other contributors to the inherent "barrier" aspect of the free surface include the promotion of the interaction of defects in the surface layer by gradients in the vacancy or solute concentrations, line tension effects, and the energy requirement to produce surface steps at the point of emergence of screw dislocation[53,23,46]. The end result, a zone featuring a high dislocation density and a high degree of entanglement created at or near the surface, causes the predominance of surface work hardening, at least during the initial stages of plastic deformation[54].

Finally, dislocation pileup and concomitant surface layer work hardening can be ascribed partically, or exclusively, to the presence of oxide and metal films. "Trapping" or "blocking" of egressing dislocations by oxide films has been proposed to account for aggravated pileup and associated increases in the CRSS and hardening rate for specimens susceptible to surface oxidation[55-57]. A "locking" of surface dislocation sources by solid surface films was suggested by other scientists to explain the increased resistance to initial plastic flow[58,59], but the mechanisms did not explain the stress-strain curve slope changes. Peripheral experiments showing an extension of the uniaxial deformation stages I and II, and a corresponding reduction in their slopes, during testing in surface-active agents have been interpreted in terms of the weakening effect of physical adsorption[60] and oxide film removal [61]. The softening observed in studies on nonoxidizing metals, however, indicated that the presence of a strong film was not a necessary prerequisite for dislocation pileup at the surface[31]. Further, it was argued that the

failure to witness the softening effect for "clean-surface" specimens under agressive environmental conditions could be alternatively explained by the absence of a soap reaction for this surface condition, rather than to the failure to oxidize[62].

Summarizing the preceding discussion, it is clear that the free surface can function independently as a source of dislocation nucleation and multiplication and as a barrier to dislocation egression. The preferential generation and retention of dislocations leads to surface layer work hardening, the predominance of which is magnified when acting in conjunction with a hard surface layer or film.

c. "Surface Layer Stress" Measurements. When dislocations formed during the early stages of deformation were trapped in the near-surface region to form a kind of "debris" layer, Kramer suggested that a "back" stress was introduced by the piled-up arrays, which opposed the motion of other dislocations into the surface layers[24]. A greater stress then had to be imparted to the specimen to attain a given strain than would have been required if the work hardening were uniform and equivalent to the bulk level throughout the cross section. The additional stress required was defined as the "surface layer stress" and represented the extra work hardening or resistance to dislocation motion associated with the surface layer. It should be emphasized that the "surface layer stress" represents an increased surface plastic resistance and is not appropriately described as a residual stress.

For fcc single crystals the work hardening during stage I deformation was found to be exclusively associated with the surface layer[63]. At the end of the easy glide stage, the CRSS was equal to the difference of the applied and surface layer shear stresses. Thus, as the back stresses increased with increasing strain, slip on secondary systems could not start until the applied stress exceeded the sum of the surface stress and the stress required to activate the sources. Similar findings for polycrystalline aluminum and gold disclosed in addition that the surface layer stress varied with the plastic strain level according to the typical power relationship embodied by the strain-hardening exponent[64].

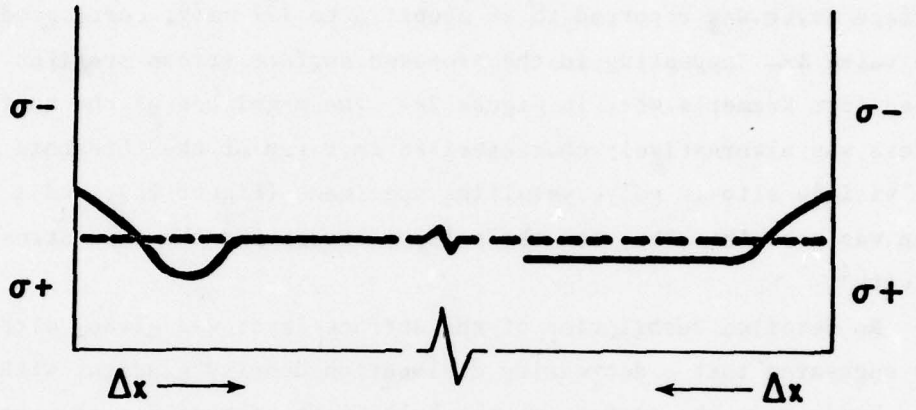
The stress fields in the surface layer were shown to have a short-range characteristic, demonstrated by their disappearance after a short, low-temperature anneal, and also to exhibit a long-range stress effect arising from interactions between the surface stress fields and mobile dislocations approaching from the bulk regions [63,65]. The depth of the surface layer was reported to be about 76 to 127 μm[24], corresponding to the value Δx_∞ appearing in the proposed surface stress profiles reproduced from Kramer's work in Figure 2a. The magnitude of the surface layer stress was alternatively characterized in terms of the threshold stress for visible slip in polycrystalline specimens (Figure 2b), and a connection was postulated between the surface stress and the flow stress size effect[64].

No detailed description of the surface layer was given, although it was suggested that a decreasing dislocation density gradient within the slip bands from the surface to the bulk might account for the correlative flow stress gradient[27]. It is evident, therefore, that quantitative analysis of the defect distribution with depth and elucidation of the respective surface and bulk microstructures induced by plastic deformation are critical to the confirmation of the "hard" surface predominance.

2. Role of the Surface Layer in Metal Fatigue

a. Fundamental Deformation Characteristics of Fatigue Failure. Fatigue performance has long been known to be critically dependent on the condition of the exterior surface of metal components. It is generally agreed that fatigue cracks originate in the surface region. However, despite the considerable effort expended in the last two or three decades to understand the mechanisms governing crack initiation and propagation, no real consensus on what constitutes fatigue "damage" prior to these processes has yet emerged. Description of the microstructural fatigue damage, which serves as a precursor to failure, should enhance the capability for control of fatigue resistance. It should also permit the estimation of fatigue life under a variety of stress, temperature, and environmental conditions, as well as the prediction of the remaining life of components already in service.

(a)



(b)

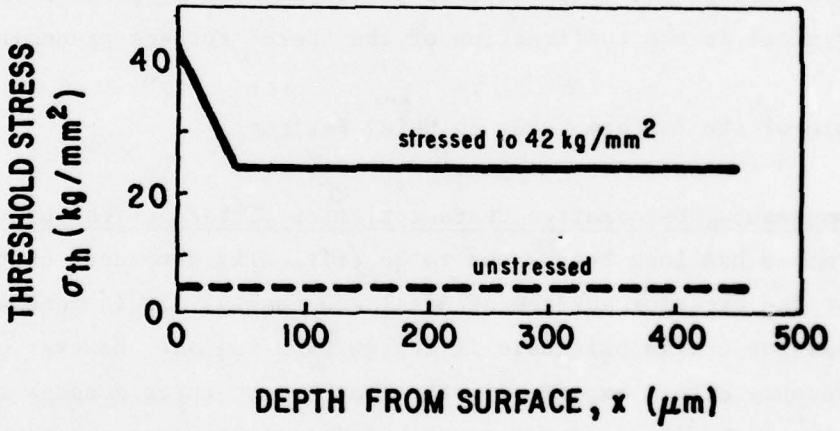


Figure 2. Evidence of preferential surface work hardening. (a) alternative residual stress distributions in the surface layer and bulk material after plastic deformation; and (b) threshold stress for plastic flow of Al 2014-T6 as a function of depth from the surface, measured from the first appearance of slip bands.

As mentioned earlier in the brief introductory chronology of fatigue-related research, the first observations were confined to the fundamental deformation characteristics of cycled metals. Limited by the available optical microscope techniques, these studies concentrated on interpreting the surface topography, such as slip bands and intrusion and extrusion striation markings, in terms of their topological counterparts, namely, slip mode and homogenization, and crack formation and propagation phenomena. The association of incipient cracks with persistent slip bands (PBS's) was detected by Thompson et al.[66]. The early appearance of the PSB's indicated that the balance of the fatigue life was consumed by the crack propagation process. Grosskreutz reported that crack initiation in the structural-type alloys, Al 2024-T3 and 4130 steel, was delayed until 60-70 percent of the total fatigue life had been expended[67]. Fatigue cracks were also reported to originate at intrusions and extrusions[2-4,68]. Using a tapered section technique, Wood et al. confirmed the propensity for fatigue crack initiation in the surface region[69].

The surface morphology was later correlated to microstructural characterizations facilitated by the advent of electron microscopy. A distinction was observed among various metals, founded on their potential for dislocation motion[15]. The ability to cross slip, which varies as the magnitude of the stacking fault energy (SFE), was reported to influence strongly the surface features and cracking mechanism[7,70]. Low SFE metals were usually reported to exhibit planar arrays of dislocations[71], and were, therefore, denoted as "planar slip-mode" metals[8]. The slip band structure of these metals and alloys (which included titanium, magnesium, stainless steels, and brass) revealed dense bands of dislocations interspersed with dislocations dependent on the initial condition of the metal. The high-SFE, or "wavy slip-mode" metals such as aluminum, copper, iron, and nickel featured unrestricted dislocation motion facilitated by cross slip, resulting in the formation of interconnected bands containing dislocation dipoles, loops, and other debris[29,72]. At high strains, a cell structure was observed over the entire section of monocrystals, while at low strains a bulk structure consisting of dipole clusters or veins was correlated to the PSB's at the surface[73].

It was evident, however, that cross slip was not basic to the formation of PSB's. Nine et al. carried out torsional fatigue studies of single crystal copper[74,75]. In these experiments, it was observed that slip between the twist boundaries forming the sides of a cell-type structure induced by low strain amplitude fatigue easily accounted for the striation distribution. The ladder-like cell structure's development in copper, and its association with fatigue striations, were also reported by Laufer and Roberts[13]. The underlying dislocation structure in this system was also studied by Levine and Weissmann[14].

Therefore, while no single mechanism could be credited with adverse local concentration of plastic deformation, and thus with sole responsibility for crack initiation, it was clear that maintenance of a homogeneous slip condition was essential to insuring good fatigue resistance[15]. In polycrystalline materials, cracks were often found to nucleate at grain boundaries or inclusions when slip-related surface features failed to provide the necessary stress intensification for cracking[76-79]. Watt et al. conducted experiments which showed the reproduction of original slip bands after removal of a 300-μm surface layer from copper single crystals, and proposed that the plastic elements associated with localized "reversible" slip were distributed throughout the crystaL, not confined to the surface[80]. Nevertheless, recent TEM studies of polycrystalline iron have shown that the plastic flow at the surface always represents a more advanced stage of development than in the bulk, even when the flow has proceeded over the entire cross section[81]. It has also been shown that surface treatments or testing under particular environmental conditions, which tend to cause enhanced slip dispersal during cycling, increase significantly the specimen longevity[72,82,83]. The same philosophy has been employed to improve the fatigue resistance of precipitation-hardened alloys by thermomechanical treatment (TMT), although the impact of the process is not restricted to the surface layer. Again, the objective was to eliminate heterogeneous aging effects in the form of precipitate-free zones (PFZ's) prior to fatigue to promote a metallurgically stable structure that would support homogeneous deformation during subsequent cycling[84].

b. Bulk-Hardening/Softening Phenomena Induced by Fatigue Cycling. Another characteristic of fatigue deformation that has been studied extensively, but proved difficult to relate to crack initiation and failure, is the cyclic hardening or softening phenomenon[4,6,85-91]. It should be noted that fatigue failures occur for specimens that exhibit work hardening, work softening, or work hardening followed by work softening[92]. This implies that any functional relationship between fatigue failure and cyclic hardening or softening would involve a number of fatigue mechanisms. One controlling factor in determining the operating mechanism has been identified as the stress-strain amplitude. The cyclic strain-hardening rationale, defined by Feltner and Laird[8], stipulated that a correlation exists between low-amplitude strain-hardening behavior and stage I unidirectional deformation, and between high-amplitude strain-hardening and stage II unidirectional testing. The former is characterized by the formation of dipoles, while the latter involves the formation of a cell structure. Their cyclic strain-softening rationale assumed as a prerequisite that "reversed plastic flow" occurs and that the rate of cyclic softening is controlled by frictional-type impediments to mobile dislocations.

Experimentally, these investigators determined that a saturated condition was achieved for annealed fcc metals after about 15-20% of the life. The stress response of cold-worked specimens required about 50% of the total life to attain a stabilized condition. Surprisingly, the microstructure at saturation was essentially the same for both the annealed and cold-worked specimens for representative metals of both slip mode characters. The saturation stress was found to be a unique function of the cyclic strain range, strain rate, and temperature. Further, its apparent independence of prior strain history permitted the postulation of a "cyclic mechanical equation of state."

Both McGrath and Bratina[7] and Lukas and Klesnil[93] studied the cyclic hardening in bcc iron and found surface features and microstructures

---

*These results are of particular interest and pertinence to the present investigation since the same alloy was chosen for the surface studies.

similar to those obtained for fcc metals. The transient saturation-hardening stage has been ascribed to a decrease in the production of fresh dislocations, coupled to a "flip-flop" motion of existing dislocations[7,94].

Greenhut[95] studied the cyclic deformation of Al 2024* and characterized the substructural response contributing to the fatigue-hardening process. The alloy had a bimodal nature; one precipitate consisting of S"-S'-S particles, depending on the aging treatment, and the other tentatively identified as an α(AlMnSi)-α(AlFeSi) incoherent inclusion. TEM analysis of the ambient-temperature aged alloy revealed the formation of prismatic disocation loops by the interaction of moving dislocations and the inclusions early in the cycling process. Acting as a barrier to dislocation motion, these loops produced a finer, high-density dislocation loop debris which, at failure, formed the boundaries of a cell-like structure.

Recalling Feltner and Laird's proposal that the saturation stress is independent of the prior strain history[8], it must be presumed that cold-worked metals must undergo a transient stage of cyclic reversion of the prior deformation to achieve the deformation substructure characteristic of saturation condition of annealed specimens. For design purposes, this behavior is distinctly problematic, since the strength properties in low-cycle fatigue would be significantly less than expected from the monotonic testing[96]. As expressed by Grosskreutz[15], the softening effect signifies a loss in "load-carrying ability" and can thus be viewed as detrimental degradation of the high-strength microstructure produced during the prestressing or prestraining operation. Age-hardened alloys have been reputed to be especially susceptible to softening effects. Since these alloys are hardened by a metallurgical process, the softening mechanism proposed by Forsyth[97], involving a redissolution of precipitates by the repeated and systematic cutting by dislocations, is a plausible though somewhat disputed[98] hypothesis.

On the other hand, if extended life rather than fatigue strength is the primary design criterion, softening can be credited with beneficial results. Studies of Al and Ag single crystals cycled in the bending mode have shown that alternating between high and low strain amplitudes is capable of delaying crack initiation and reducing the crack propagation

rate[99,100]. The sequence of amplitude changes promoted climb- and glide-aided substructural recovery and reduced the deleterious effect of introduced grain boundaries in the crystals, increasing the average life by about four times. Since the behavior was found comparable to that produced by intermittent annealing, the softening due to intermittent low-strain cycling was ascribed to the dislocation rearrangement, stimulated by an ample vacancy supply from nonconservative motion of jogged, oscillating dislocation segments.

c. Correlation of Surface Layer Work Hardening to Fatigue Failure. The hardening and softening behavior recounted in the previous section has earned acceptance as a tenable bulk process. However, the relationship between fatigue failures and the cyclic hardening or softening was further complicated by the findings of Grosskreutz[67]. He reported that slices cut from cyclically failed copper specimens exhibited fatigue lives comparable to that of the original specimen and concluded, therefore, that the "damage' introduced to the copper during the initial fatigue process was harmless, serving only to determine the flow stress. The implication that the bulk hardening or softening under constant-amplitude cycling was significant only in terms of the dynamic strength properties of the metal lent support to the growing evidence that the fatigue life was critically dependent on the surface hardening or softening behavior.

Fourie invoked the opinion that, while at the outset there is no substantial difference in plastic resistance for the surface or interior, during deformation a variation emerges due to the inefficiency of cyclic strain hardening near the surface of annealed crystals[101]. Argon then argued that "damage" accrues by void and porosity concentration in the slip bands, shown to be "soft" by micro-hardness measurements, such that incipient cracks are nucleated[102]. A vacancy production mechanism during high-amplitude cycling was correlated to the recovery and fragmentation of hard surface layers introduced by prior surface treatment, and ultimately with condensation into voids to cause failure. This recovery mechanism is obviously in contrast to the beneficial vacancy-aided bulk recovery thought to be promoted by the low-amplitude blocks of a variable-amplitude fatigue program[99-100].

Early in the 1950's, Vitovec also observed that limited cycling at high strain amplitude, prior to fatigue at a lower strain, resulted in considerable extension of the fatigue life[103]. Conducted in the bending mode, the improvement in fatigue performance was described in terms of a "training" effect in which the surface region was strengthened so as to resist further fatigue damage. The hardening aspect was shown experimentally by a decreasing gradient in the etching rate from surface to bulk, indicative of a higher dislocation density at the surface (Figure 3). On the basis of the applied stress distribution in bending, preferential surface work hardening would not be an unexpected result. Later, however, uniaxial fatigue of polycrystalline aluminum and copper also revealed an increase in the "surface layer stress" compared to the bulk material[104,105]. In these investigations it was shown that the cycling increased the flow stress and activation volume of the specimens. But when the surface layer was removed, the flow stress and activation volume reverted to their original uncycled values. Kramer's work on fatigue of precycled commercial alloys[106] revealed a behavior comparable to that observed earlier by Vitovec. When a short period of high-amplitude cycling was performed prior to cycling to failure at a lower amplitude, an anomalous life extension was obtained. The life increased as the decrement in stress amplitude increased, and decreased if the prior fatigue was carried beyond a certain limiting number of cycles (Figure 4). The imposition of a "hard" surface layer by prestraining bears some resemblance to the improved resistance to damage afforded by long-employed surface preparation techniques such as shot peening[107], and surface rolling[102,108] which introduce compressive residual stresses to the surface layers.

In summary, the divergent conclusions drawn from similar experiments demonstrate the complexity of the fatigue process. Thus, bulk softening was shown to have a deleterious effect on dynamic strength properties, but a beneficial life extension is gained through bulk substructural recovery induced by low-strain cycling. At the surface, on the other hand, both detrimental softening within the slip bands and progressive surface layer work hardening have been shown to lead to crack initiation. In addition, deformative surface treatments or prestraining has led to life extension.

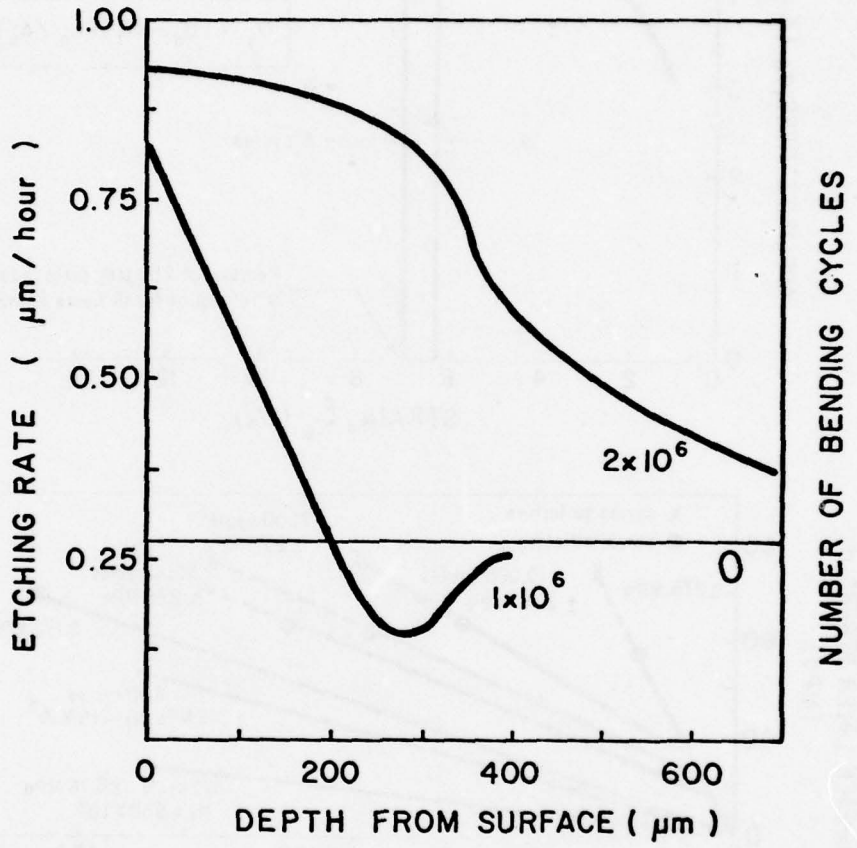


Figure 3. Dependence of the etching rate on the distance from the specimen surface for fatigue cycling of annealed steel. (0.18% C, 0.66% Mn, 0.021% Si, 0.066% S, and 0.04% P.)

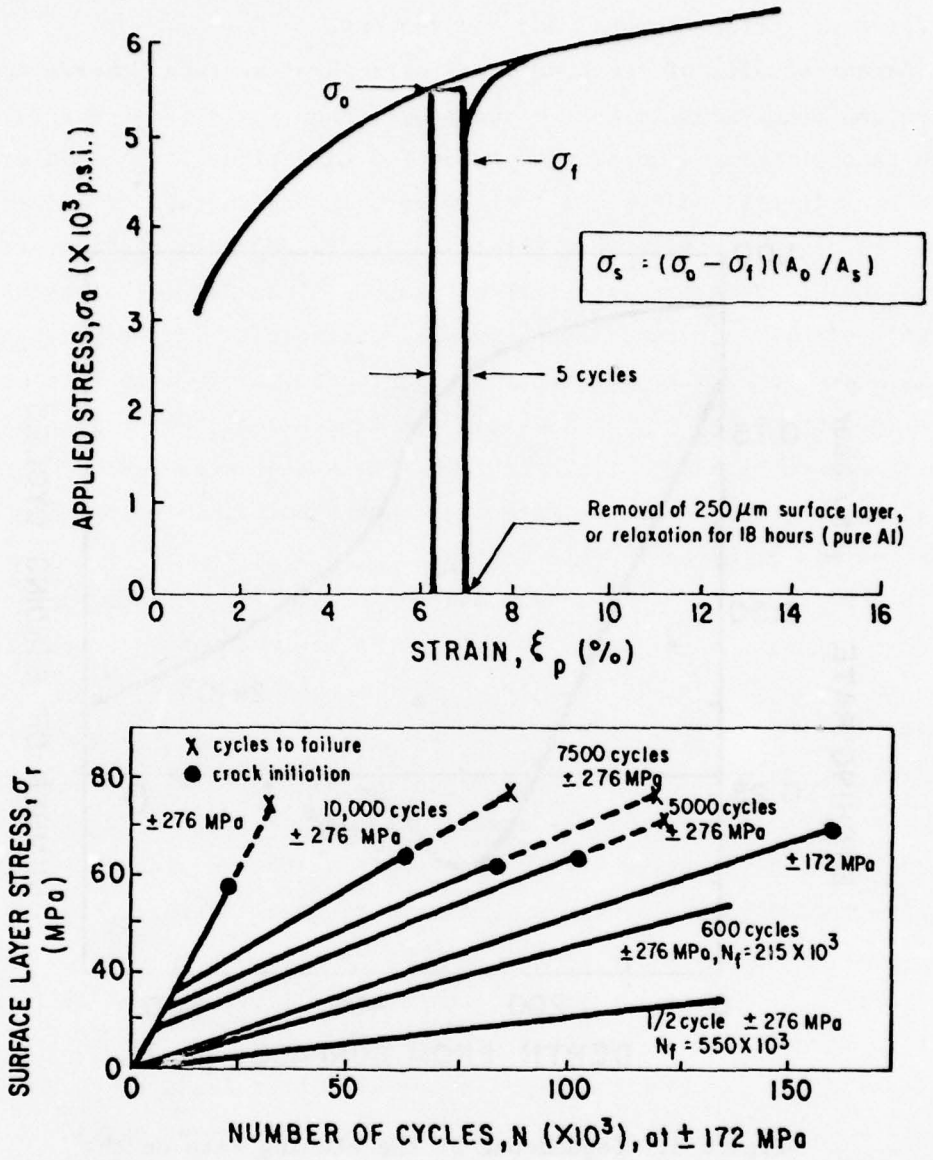


Figure 4. Determination of the surface layer stress induced by fatigue, and its change with the number of cycles under variable amplitude loading: (a) typical composite stress-strain curve showing the increase in strain during stress cycling, and the decrease in the flow stress after surface removal and reloading; and (b) increase of the surface layer stress during cycling at ±172 MPa, after limited periods of prior fatigue at ±276 MPa for Al 2014-T6.

Still another important aspect in surface-related fatigue processes is the effect of surface removal and environment.

Recent studies of the beneficial effects of surface removal are an interesting complement to the long-employed shop practice of machining the surface of service components subjected to fatigue. Thompson et al. showed that intermittent removal of 30 μm from the surface of copper specimens prolonged their fatigue life. He attributed this effect to the elimination of PSB's and incipient cracks[66]. Alden and Backofen showed that periodic surface removal or annealing treatment, if performed prior to saturation hardening, substantially prolonged the fatigue life of aluminum single crystals[4]. They ascribed the improvement, however, not to a removal of accumulated damage, but rather to a prolonged period of random slip step emergence at the surface, and thus a postponement of slip concentration and cracking in this region.

Recent TEM studies of single and polycrystalline copper subjected to tension-compression fatigue in an aggressive environment have been interpreted in terms of the cracking process or mechanism[72]. For the single crystals, increased life spans due to the suppression of crack propagation were attributed to the blunting of cracks by preferential corrosion of PBS's. For the polycrystalline specimens, reduced lives were ascribed to the acceleration of intergranular crack initiation and propagation by the corrosive medium. Similar tests performed on Cu-5%Al single crystals again indicated a mechanism in which the corrosive medium attacked the PSB, "unraveled" the dislocations, and caused a rearrangement of the normal fatigue-induced "vein" structure[82].

The fatigue resistance in vacuum has also been found to exceed substantially the normal life in air for Fe-3.72Si specimens cycled at constant-strain amplitude[83]. The absence of striations for aluminum alloys fatigued in vacuum had been previously interpreted as complete reversion of the crack-opening displacement, a mechanism termed "rewelding," since oxidation of the newly created free surfaces was prevented[109]. Snowden postulated that the observed intergranular crack initiation in air and transgranular cracking in vacuum was related to the reduction in grain boundary energy by a similar oxygen absorption process[110]. Shen et al. suggested that the primary reason for improved resistance in vacuum was

more efficient dislocation egression due to the absence of an oxide film[111,112]. Kramer, who cooperated in this latter study, and his co-worker Kumar, found additionally that the "surface layer stress", as well as the rate of cyclic hardening, was less for specimens cycled at reduced pressures or in an inert atmosphere[113]. In the same study, the surface layer stress of Ti(6Al-4V) increased markedly, while the fatigue life decreased when tested in solutions known to promote corrosion fatigue and stress corrosion cracking.

In consideration of the work hardening exhibited by the surface layer of fatigued metals, Kramer questioned whether the increase in life normally attained on surface removal was due, in fact, to the elimination of cracks and slip bands[115]. He proposed, instead, that the behavior might be more accurately described as an elimination of the barrier to dislocation motion represented by the preferentially work-hardened surface layer. According to this concept, when the obstacle strength of the surface layer becomes sufficiently great to support a piled up array of dislocations of like sign, a crack would form when the local stress in the pileup exceeds the fracture strength, in accord with the fracture theory proposed by Stroh[114]. The pileup would not have to be a linear array; rather, the accumulation of dislocations of like sign needs only to satisfy the condition that the net addition of the cumulative stress fields exceeds the fracture strength. Given the decreasing dislocation gradient from the surface into the bulk, the elastic energy would be dissipated over a short propagation distance, requiring further cycling to reestablish the failure criterion for continued crack growth. The concept implies that the surface layer stress must reach a critical value, independent of stress amplitude, in order for cracking to be initiated. In a comprehensive evaluation of the surface layer stresses generated by fatigue in various commercial alloys[115], this behavior was confirmed. Reference to Figure 4(b), taken from similar work[106], discloses the invariance of the critical surface layer stress even under complex loading conditions.

A wide range of x-ray analysis techniques, from conventional line broadening to microbeam methods, were employed by Taira et al. to confirm the close correlation of the surface microstructure to fatigue failure[116,117]. Much of their data for cycled steel specimens appear to

support the cyclic generation of a "hard" surface layer. Composite illustrations of the dependence of the "halfvalue breadth" (lattice misorientation), Vicker's hardness, and residual compressive stress as functions of both the fatigue life and depth from the surface are reproduced from their study in Figures 5 and 6, and will be discussed in more detail with regard to fatigue life prediction. The results indicated that the damage produced and stored in the surface layer, reaching to a depth of about one grain's diameter, substantially exceeds that of the bulk material. The question as to whether the life extension by surface polishing is due to elimination of this barrier-like layer, or simply related to the reduction in surface relief and associated microcracks, remains unanswered. Duquette and Laird recognized this problem in their discussion of the difficulty in assessing the contribution of the dislocation structure to fatigue damage[118]. Although it is nearly impossible to return the internal microstructure to its initial state without destroying the surface topography, they propose that to predict the total fatigue life it would be necessary to formulate a quantitative description of the severity of the surface relief and evaluate the importance of the dislocation structure in the surface layer. Kramer's investigations involving layer removals from the surface of fatigued specimens have indicated that elimination of the surface relief does not account for the major portion of the extension in life[40]. Removal of layers of sufficiently shallow thicknesses, to eliminate only the slip bands, produced only small reductions in the surface layer stress. The corresponding increases in fatigue life were also small, compared to the greater life extensions achieved by removing the entire work-hardened surface layer to about 100 μm in depth.

The following discussion will present a brief introduction to fatigue life and failure prediction, both from "macroparameter" and "microstructural" approaches. Although the existence of a surface layer/barrier has not yet been fully confirmed and characterized on a microstructural level, the concept stands out as a unifying rationale for various fatigue processes, and thus will be briefly examined as a macroparameter in semi-empirical fatigue life prediction. X-ray diffraction analysis, combined with reflection topography, on the other hand, exhibits great potential for nondestructive fatigue failure prediction on the basis of microstructure.

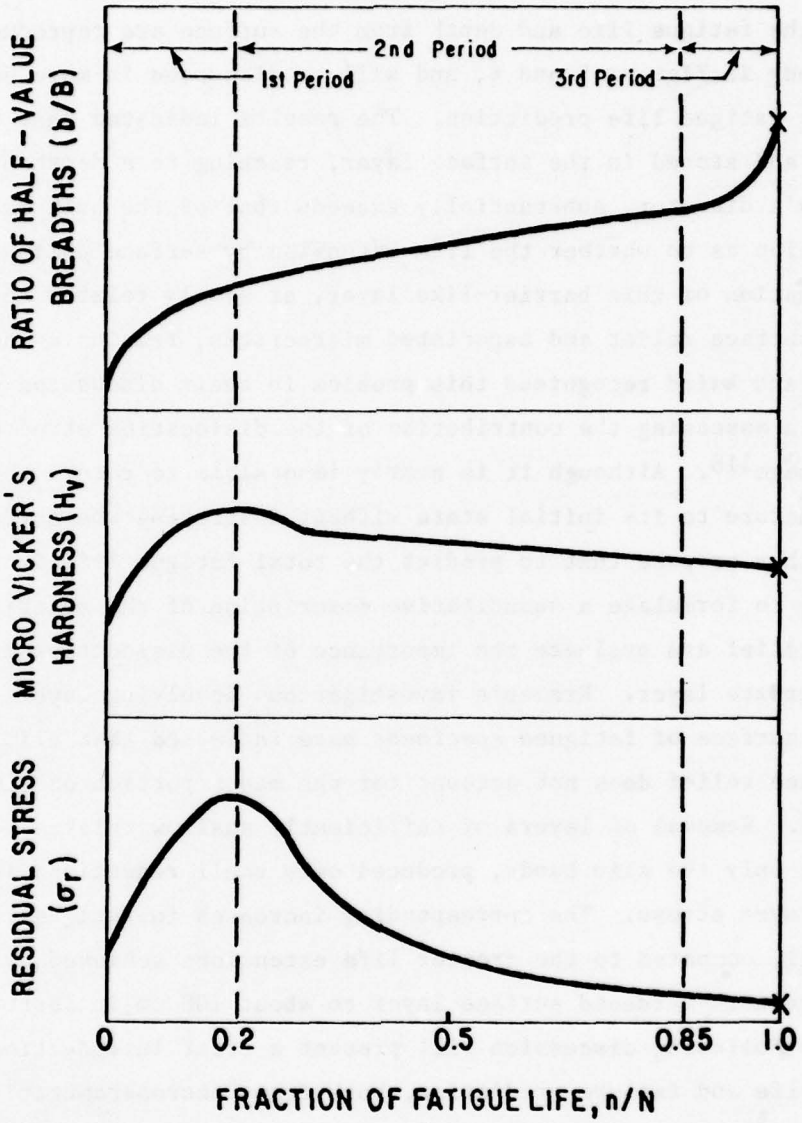


Figure 5. Schematic illustration of the changes in the half-value breadth, Vicker's hardness, and compressive residual stress at the specimen surface during the fatigue life for cantilever-type plate bending of unnotched steel.

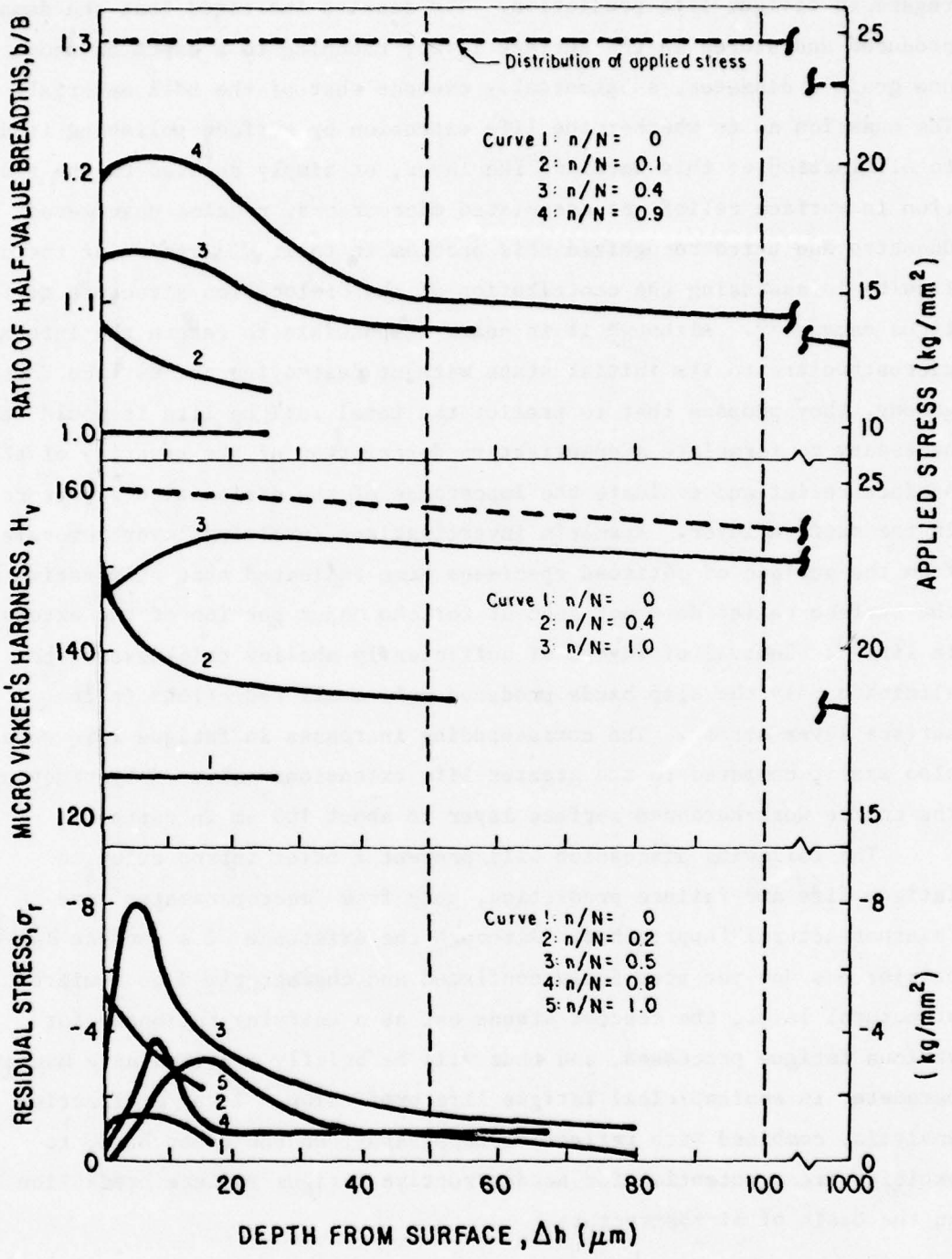


Figure 6. Distribution of b/B, H_v, and σ_r with depth from the surface.

regard to fatigue life prediction. The results indicated that the damage produced and stored in the surface layer, reaching to a depth of about one grain's diameter, substantially exceeds that of the bulk material. The question as to whether the life extension by surface polishing is due to elimination of this barrier-like layer, or simply related to the reduction in surface relief and associated microcracks, remains unanswered. Duquette and Laird recognized this problem in their discussion of the difficulty in assessing the contribution of the dislocation structure to fatigue damage[118]. Although it is nearly impossible to return the internal microstructure to its initial state without destroying the surface topography, they propose that to predict the total fatigue life it would be necessary to formulate a quantitative description of the severity of the surface relief and evaluate the importance of the dislocation structure in the surface layer. Kramer's investigations involving layer removals from the surface of fatigued specimens have indicated that elimination of the surface relief does not account for the major portion of the extension in life[40]. Removal of layers of sufficiently shallow thicknesses, to eliminate only the slip bands produced only small reductions in the surface layer stress. The corresponding increases in fatigue life were also small, compared to the greater life extensions achieved by removing the entire work-hardened surface layer to about 100 μm in depth.

The following discussion will present a brief introduction to fatigue life and failure prediction, both from "macroparameter" and "microstructural" approaches. Although the existence of a surface layer/barrier has not yet been fully confirmed and characterized on a microstructural level, the concept stands out as a unifying rationale for various fatigue processes, and thus will be briefly examined as a macroparameter in semiempirical fatigue life prediction. X-ray diffraction analysis, combined with reflection topography, on the other hand, to exhibits great potential for nondestructive fatigue failure prediction on the basis of microstructure.

3. Prediction of Fatigue Failure

a. A "Macroparametric" Approach. Most attempts to predict fatigue life have traditionally employed a "macroparametric" approach as defined by Grosskreutz[15]. This procedure involved the development of semi-empirical equations relating a macroscopic mechanical property of a material to its fatigue life, or the number of cycles required to induce failure. Basquin, for instance, proposed that the data from ordinary experimentally derived S-N curves could be expressed by a linear relation between the logarithms of the applied stress amplitude and the number of cycles to failure[119]. The slope and intercept of the line are now referred to as the material-dependent fatigue strength exponent b and coefficient σ_f', respectively, and the predictive equation for controlled stress dynamical behavior is expressed as

$$\sigma_a = \sigma_f'(2N_f)^b \qquad (1)$$

where σ_a is the applied stress amplitude and N_f is the number of cycles to failure. The Coffin-Manson relationship[120-121] is currently used to describe the inelastic cyclic behavior under controlled strain conditions, or "thermal" fatigue, in the form

$$\Delta\varepsilon_t/2=(\Delta\varepsilon_p/2)+(\Delta\varepsilon_e/2) = \varepsilon_f'(2N_f)^c + (\sigma_f'/E)(2N_f)^b, \qquad (2)$$

where $\Delta\varepsilon_t$ is the total strain amplitude, and $\Delta\varepsilon_p$ and $\Delta\varepsilon_e$ are the plastic and elastic components of the strain, respectively; ε_f' and c denote the fatigue ductility coefficient and exponent; and E is Young's Modulus. Since the plastic component predominates the behavior in low-cycle fatigue, the expression can be simplified to

$$\Delta\varepsilon_t/2 \tilde{=} \varepsilon_f'(2N_f)^c \qquad (3)$$

The equations have been combined [122] to derive a parabolic equation similar to that used to fit monotonic stress-strain curves, namely

$$\sigma_a = \sigma_f'(\Delta\varepsilon_p/2\varepsilon_f')^{n'} \quad (4)$$

where n' is the cyclic strain hardening exponent which like σ_f' and ε_f is related to the monotonic counterpart. This equation describes the dynamic response after saturation has occurred and the stress response is relatively stable. The cyclic stress-strain curve is derived experimentally by drawing a curve through the tips of the stabilized hysteresis loops obtained for different amplitudes. The problem of predicting the initial hardening or softening response in low-cycle fatigue, defined as the change in stress required to enforce a given strain limit as a function of the number of cycles, has been reviewed by Feltner and Landgraf[96]. A simple, two-step test was devised to measure and rank materials according to their ability to resist repeated stressing or straining for a given life level, taking both the initial and saturation behaviors into account. Equation 3 has been modified to use the plastic work per cycle W_p, as the input variable of the failure criterion under total plastic strain control conditions when there is often no tendency for saturation, i.e., the plastic strain continues to change with N[123]. The invariance of W_p with the number of cycles gave rise to a single straight line log-log plot when substituted as the independent variable in the Coffin-Manson relation. Data from several precipitation-hardened aluminum-base copper alloys, including Al 2024 all fell on the same single-segment line.

Many of these prediction laws are subject to inconsistencies caused by effects such as notch sensitivity and environmental attack, and concomitant acceleration of the dynamic crack initiation and growth rates[124]. Mircrostructural inhomogeneities intrinsic to the test metal itself, produced by the slip mode character, grain boundaries, inclusions, and second phases, have also hampered the semi-empirical predicition efforts.

b. Cumulative Damage Rules. The most severe hindrance to the prediction of cumulative damage, i.e., the addition of fractional damage incurred during cycling blocks with different amplitudes, is the load interaction effect on the operating fatigue mechanism. To be truly useful in design, cumulative damage rules must incorporate the influence of mean stress or

strain, and occasional overloads. One method for rectifying their contribution has been to treat the occasional overloads or mean-stress blocks as if they were actually initial prestresses, or alternatively to convert the combination of the peak amplitude and mean stress to a representative reversed-stress amplitude[125]. The cumulative damage formulations improvised by Palmgren[126], and later by Miner[127], avoided these concerns by assuming implicitly that the number of cycles at each amplitude always advances the damage accumulation. In other words, the change in the life produced by occasional overloads, which could cause either aggravation of the cracking process or the imposition of favorable residual stresses at potential failure sites[128], or afforded by substructural recovery due to large high-to-low amplitude decrements[99], was essentially neglected. The hypothesis suggested a linear addition of the fractions of the total life "used up" during the cycling at each amplitude such that

$$\sum(N/N_f)_i = 1 \tag{5}$$

which should hold if the extent of the cycling at each level is nearly equal.

c. <u>"Surface Layer Stress" as a Damage Criterion</u>. Practical implementation of the cumulative damage rule, for example, to predict the remaining life of a metal component already in service requires the definition of a damage criterion from which the expended life can be determined without full knowledge of the prior cyclic history. The "surface layer stress," found by Kramer to vary as the fraction of life, was uniquely suited for this purpose[104]. Related to Miner's hypothesis, the accumulated damage for each stress block would be expressed as

$$D_i = (\sigma_s/\sigma_s^*)_i, \tag{6}$$

and failure would be initiated when

$$\sum D = \sum(\sigma_s/\sigma_s^*)_i = 1, \tag{7}$$

where the critical surface layer stress σ_s^* was found to be independent of the cyclic stress amplitude and environment.

In a systematic study of Al 2014-T6, Ti9(Al-4V), and 4130 steel, a linear relationship was observed between σ_s and N for constant-stress amplitude cycling[115]. The slope of the curves varied with applied stress amplitude according to the typical power law.

$$S = d\sigma_s/dN = k\sigma_a^{-P} \tag{8}$$

where -P is the slope of a log-log plot of S for each stress amplitude σ_a. Since $\sigma_s^* = SN_f$, a Basquin-type relation was derived and confirmed such that

$$N_f = (\sigma_s^*/k)\ \sigma_a^{-P}. \tag{9}$$

Assuming that the applied stress is to be held constant or that the slope S for a particular amplitude is insensitive to past history, the remaining life of a part could be estimated by measuring the acculmulated surface layer stress σ_s, computing the fraction of the life used up from Equation (6), and computing the remaining cycles to failure at the amplitude to be employed in subsequent testing as a fractional amount of N_f in Equation (9).

In later studies of the same alloys, however, it was observed that the slopes S for each testing amplitude did vary with the extent of prior cycling at a different amplitude[106]. This required redefinition of the slopes, such that the earlier simplified failure criterion

$$\Sigma S_i N_i = \sigma_s^* \tag{10}$$

was expanded to the form

$$\begin{aligned} &N_1S_1 + N_2S_2(S_1/S_2)^{f_1} + N_3S_3(S_2/S_3)^{f_2(S_1/S_2)^{f_2 f_1}} + \ldots \\ &\quad = N_1S_I + N_2S_{II} + N_3S_{III} + \ldots = \Sigma N_i S_X = \sigma_s^*, \end{aligned} \tag{11}$$

where S_X represents the modified slope, taking into account the history of

amplitude changes. This formulation was found reliable for prediction under variable-amplitude conditions, even in the case of high-to-low amplitude programs, as long as the decrements were small enough and the frequency of change high enough to avoid the anomalous life improvements inherent to short-duration overstressing. Substituting for the slopes S_i in terms of the applied stress, equation[11] becomes

$$\sigma_3^*/k = \sigma_1^{P}N_1 + \sigma_2^{P}N_2(\sigma_1/\sigma_2)^{pf_1} + \sigma_3^{P}N_3(\sigma_2/\sigma_3)^{pf_2f_1} + \ldots \qquad (12)$$

The values for σ_s^*/k and P may be obtained from Equation (9). Kramer obtained very good agreement between the experimentally derived Σf_i and N_f data and their predicted values.

A more direct approach to prediction based on the fatigue-induced microstructure has thus far met with little success. A brief state-of-the-art discussion of past attempts in this direction is provided in the next introductory section to x-ray defect analysis.

B. X-RAY DEFECT ANALYSIS AND APPLICATIONS TO FATIGUE

The key to predicting fatigue life from a microstructural viewpoint is the isolation of a telltale, easily measurable, material characteristic representative of fatigue damage. However, the complexity of the various microstructural mechanisms produced by, and responding to, the cycling process inhibits the filtering out of a quantitative feature indicative of the expended life, and thus of the fractional life remaining before failure. As suggested by Taira, x-ray diffraction analysis provides a unique and diverse selection of methods with which to examine the mechanical behavior of metals[129]. The techniques are highly sensitive to the changes in crystal structure and may generally be applied nondestructively. They may therefore be employed throughout a comprehensive program of materials research, including fundamental microscopic studies, testing and evaluation, and design and performance prediction in service.

Many of the early x-ray studies were devoted to the evaluation of deformation-induced stresses which could be considered to be uniformly distributed throughout macroregions on the material. The analysis of the

change in the lattice spacing homogeneity due to residual stresses from the line shifts in x-ray patterns was studied extensively by Glocker and others[130,131]. Line broadening analysis methods were developed to study the stresses which were distributed on a microscopic scale from grain to grain, or region to region. Such microstructural systems were usually treated according to a "mosaic block" concept in which the changes in secondary extinction were correlated to the integrated x-ray intensity[132]. Other microscopic lattice disturbances were found to be concentrated over highly localized regions and were, therefore, ascribed to the distortions around dislocations. In order to separate and analyze individually the contributions to the total microscopic strain, including microlattice strains and misorientations, and the degree of the breakup into sub-domains, or the "particle size" broadening, Fourier analysis of the profile shape has been employed[133-135]. The use of these techniques and procedures to study the metallurgical processes associated with particular forms of deformation began in the 1930's. The change in x-ray patterns when crystalline materials were cold worked was studied extensively by Wood and co-workers[136,137]. Gough and Wood were the first to demonstrate that a similar, though less pronounced asterism in the patterns was induced by cyclic stressing[138]. This observation led them to propose that one should should be able to identify progressive fatigue damage during cycling by intermittent x-ray pattern evaluation, and that dynamic stressing in the "safe" range should leave the patterns relatively unchanged. Proof of such a hypothesis, however, has eluded scientists for many years. As chronicled in the next section, the evidence of cyclic cold working has defied any interpretation as fatigue "damage," and the x-ray diffraction patterns obtained from cyclically stressed metals and alloys have failed to provide clearcut indications of the onset of fatigue failure.

1. A "Microstructural" Approach To Fatigue Life Prediction

A quarter of a century ago, Barrett gave witness to the existing dilemma regarding fatigue life prediction[139]. The following excerpt from his observations made in 1943 is relevant to the predicament which still persists today:

> A reliable means of forestalling breakage of machines and structures from fatigue under repeated stress would be of immense importance to engineers and metallurgists. For many years there has been a search for some non-destructive test that would predict the extent of damage caused by repeated stresses and thus predict whether or not the stresses would lead to fracture. Since x-ray methods have been most effective in revealing the internal structure of metals, it is natural that they have been investigated hopefully for this purpose, and numerous tests have been reported, both here and abroad. It seems to the author that these methods must be regarded at present as unreliable for practical use, yet papers continue to appear expressing a favorable attitude toward the x-ray methods.*

Barrett cited reports from the Fatigue Committee of the ASTM which concluded with evidence that cold work was induced by cycling in both the "safe" and "unsafe" ranges of stress[140]. He also proposed that the manifestation of cold work in fatigued metals, far from representing cyclic "damage," might actually improve the resistance to fatigue failure. Earlier, Spencer and Marshall had reported little change in the pattern sharpness of 175-T Al until the catastrophic distortions of actual fracture had already been initiated[141]. Other later investigations confirmed that line broadening could be observed after cycling to a small fraction of the fatigue life, but remained virtually unaltered both in extent and intensity throughout the remainder of the life[142,143]. It was thus evident that the cyclic introduction of cold work could not be used to esti-estimate the span of the fatigue life, nor could it be used even to diagnose accumulated damage or imminent failure.

More recent application of the sophisticated Warren Averbach method[133] to fatigued metals also produced results of limited predictive or diagnostic value[144]. Reduction in extinction due to the particle size occurred after only 1% of the fatigue life, and saturation of the root mean square (rms) strain occurred within the first 2% of the life of copper[145]. In another study[146], the change in integrated intensities was correlated to the formation of subdomains, since their 0.5 to 1.0 μm size measured by TEM was comparable to the extinction distances in copper. The line

---

* C.S. Barrett, Structure of Metals; Crystallographic Methods, Principles, and Data, 1st ed. (New York: McGraw-Hill, 1943), pp. 337-38.

broadening, on the other hand, was associated with clusters of dislocation dipoles separating the subdomains rather than the distance between them. These results contributed to the understanding of the phenomenological aspect of fatigue deformation, but the tendency for strain field cancellation indicated by the minimal broadening continued to hinder failure prediction.

Taira et al.[129] reported some success using the method of Hall[135] to separate the effects of particle size and rms strain contributing to the integral breadth of x-ray lines. The deconvolution technique showed that the microstrain increased initially, but quickly attained a constant value for the balance of the fatigue life. Evidence of a slight decrease prior to fracture was interpreted as a tendency for fatigue-induced polygonization. The particle size, however, displayed a continuous decrease throughout the life, and the individual curves for different amplitudes shifted downward with increasing strain level. It was therefore proposed that since the subgrain boundaries were known sites for crack initiation and propagation, subgrain development, indicated by the particle size reduction, and increase in boundary dislocation density might prove to be a damage parameter directly associable to imminent failure. To confirm this behavior, Taira utilized a more refined microbeam method. His previous analysis of Debye patterns from notched steel specimens had already been useful in following the progressive changes in microstructure during the fatigue life[116,147,148]. In these experiments, the incident x-ray beam was passed through a 1.0 mm-diameter pinhole and translated along the imposed notch in cantilever specimens to generate a continuous and representative diffraction ring for the region. The half-value breadth of the (310) reflection line, measured microphotometrically from the intensity distribution, was obtained as a function of the life fraction. The resulting curve featured a three-stage sequence of half-value breath expansions: a marked increase early in the cycling, a long period of nearly constant value during the intermediate fractions of the life, and another marked increase coinciding with the initiation of fatigue cracks. Simultaneous measurement of the compressive residual stresses generated during the cycling showed that the high stresses introduced early in the life decreased nearly to zero at the onset of cracking

(Figure 5). By further limiting the pinhole size to 50 μm, corresponding to a microbeam approach[149], the radial breadth of the diffraction line could be correlated to a more localized phenomenon, rather than averaging the microstructural response in many grains. Taira's use of this technique[117,150] permitted him to measure the number of subgrains m, and thus their mean size t, in a single grain, the total misorientation of the grain β, and the microlattice strain induced in the grain Δd/d for various stages in the fatigue life. The trends portrayed by these parameters during bending fatigue of low-carbon steel are reproduced from this study in Figure 7. It can be seen that the misorientation and lattice strain increased rapidly early in the life. Their magnitudes were found to be independent of the applied stress amplitude but extremely sensitive to whether or not the analyzed grain was a site of eventual crack initiation. The formation of subgrains proceeded more slowly, and for grains subject to fatigue cracking became the predominant response to the cycling process in the late stages. The breakup into subgrains was minimal for grains which did not experience cracking and was not observed at all if the cycling was carried out below the fatigue limit. Finally, fatiguing of previously rolled specimens produced a reduction in the microstrain, a rapid increase in the number of subgrains to a saturation level, and a small increase in the misorientation or half-value breadth.

While these studies provided a wealth of quantitative data with which to characterize the stages of development of fatigue damage, none of the analyzed parameters could be concluded to have significant potential with regard to reliable fatigue failure prediction. The increased resolution of the microbeam technique over the coarser averaging methods improved the capability to discern the subtle microstructural responses induced by fatigue. But the sensitivity of microbeam analysis introduced new disparities in the responses for highly localized regions, and the rapid saturation of the measured parameters continued to hinder the prediciton of failure. Even modern techniques outside the realm of x-ray analysis, designed to characterize the microstructural response as a function of fatigue life, have been found to generate descriptive curves with broad plateau regions over a significant range of intermediate life fractions. Positron lifetime data used to measure the fatigue damage in

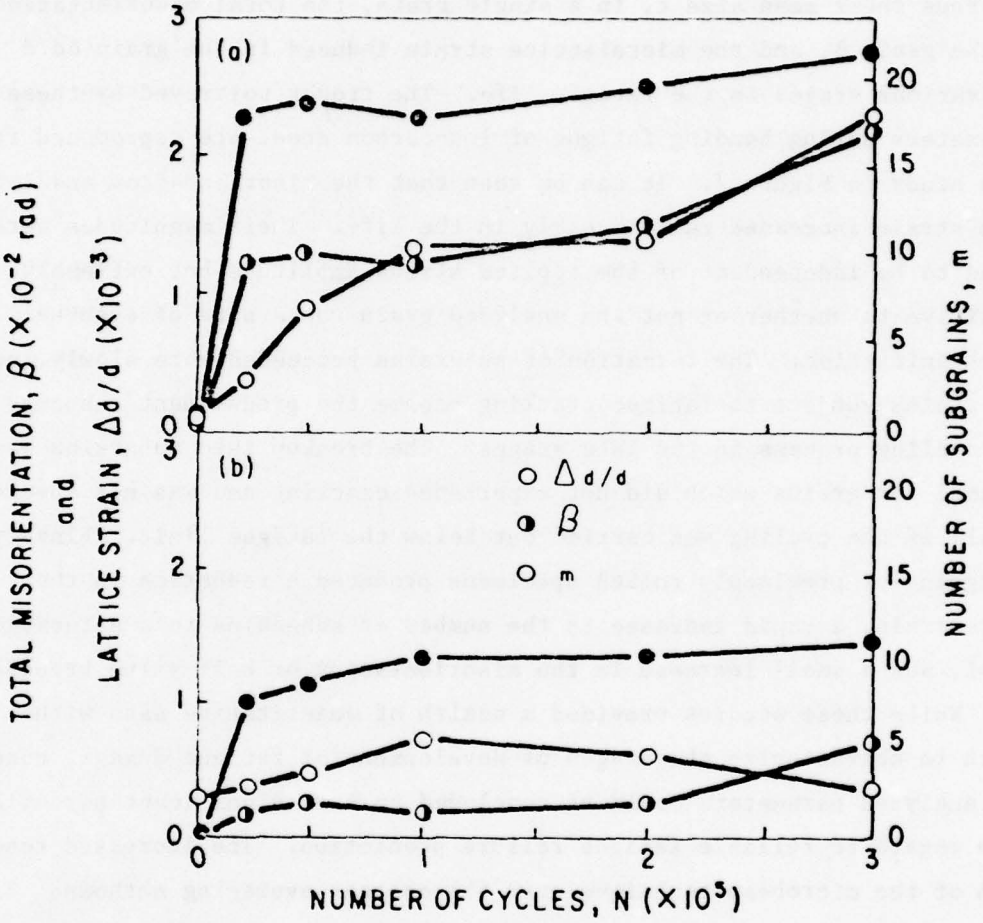


Figure 7. Changes in the lattice strain, d/d (from the radial breadth), total misorientation, (from the tangential breadth), and the number of subgrains, m (from the number of subdivided spots) during reversed bending fatigue of notched steel specimens: (a) x-ray microbeam analysis of a grain in which a crack is initiated; (b) data from a spot diffracted by a grain which does not suffer cracking.

cycled Ni and Ni-Co[151], and the acoustic emission from cycled α-Ti[152] caused by preferential fatigue damage in the twin-matrix interfaces[118,153], have been found to saturate early in the life. In 1963, however, still another x-ray method was employed to investigate fatigue-induced microstructures[154]. As presented in the next and final introductory section, the success achieved with the method in elucidating the material response to many forms of deformation, including preliminary investigations of single-crystal fatigue, predicated its use in the present metal and alloy deformation studies.

2. Double-Crystal Diffractometry and Topographic Techniques

In 1956, Hirsch[155] stated that "by far the most reliable x-ray evidence about the distribution of dislocations comes from measurements of misorientations... The most sensitive of these [techniques] is the two-crystal spectrometer method." As in the classical experiments by Renninger on rocksalt[156], the procedure involves the rotation of a crystal through its reflecting position to generate a "rocking curve," which is representative of its lattice misorientations. Intrater and Weissmann employed the technique to study the imperfections of annealed and bent aluminum crystals by measuring the breadth of rocking curves and photographing the reflected beam at discrete angular positions along the curves[157]. In 1951, however, Weissmann et al. had adapted the "double crystal diffractometer" (DCD) to study polycrystalline specimens[158]. Like the x-ray microbeam technique, the DCD method was highly sensitive to the changes in the defect structure of individual metallic grains. Instead of limiting the size of the incident beam to achieve increased resolution, the method's sensitivity to microstructural imperfections derived from the rigid parallelism of the incident radiation attained by interposition of a highly perfect monochromating crystal and defining slit system between the x-ray source and the test specimen. Under the conditions prescribed for interpreting the patterns[158,159], the distribution of photometric intensities for each of the reflecting grains was related directly to the distribution of defects in the grains, and could therefore be used to understand the structure-sensitive properties of the metal.

The method was tested experimentally on silicon powders[158] and later used to study the annealing and recrystallization response of cold-rolled low-carbon alloy and silicon ferrite[159]. These initial studies successfully revealed changes in the misorientation of subdomains and in their respective internal misalignments. Quantitative analysis of these parameters was carried out as a function of the degree of cold working of fine-grained aluminum[160] and then used in conjunction with qualitative information furnished by Berg-Barrett (B-B) reflection topography[161,162]. This combination of x-ray diffraction analysis and microscopy was performed by an outward tracing of the B-B image to the Debye pattern. A least-squares method was employed to spacially extrapolate adjacent images on the film onto the specimen surface itself to clarify the topographic relationship of the reflecting domains[162]. The procedure enabled three orders of magnitude of substructural entities to be identified for tensile deformed and -recovered nickel and nickel alloy specimens[163]. In a practically oriented study, the substructure formation during high-temperature creep of iron was analyzed[164]. Unfortunately, however, the analysis of fatigued polycrystalline metals was never attempted with the technique.

An indication of the DCD method's great potential in this respect was supplied by an investigation of fatigued single crystals[154]. The predecessor to the special DCD modification for polycrystalline materials was used effectively as an integral part of a comprehensive research program to study fatigued silver and zinc monocrystals. Counter-recorded rocking curves were combined with divergent beam, Berg-Barrett, TEM, and hardness measurement techniques to exhibit the predominance of the following fatigue processes:

1. Cyclic work hardening, accompanied by an increase in integrated intensity due to reduction in the primary and secondary extinction; an increase in the measured microhardness added evidence that the work hardening was associated with an increase in the dislocation density.

2. Dynamic recovery of the substructure, elucidated by a decrease in coarse lattice misalignments due to cross slip, and a reduction in integrated intensity and hardness; the evidence of "softening" suggested that dislocation climb was facilitated by the cyclic production of point defects, and that dislocations were "shaken" from the subgrain boundaries.

Premature failure at this stage was ascribed to obstructed cross slip by high-angle grain boundaries in Ag, or twin boundaries in Zn.

3. Fragmentation of the substructure, correlated to an enhancement of the integrated intensity and line broadening, and the generation of smooth-peaked rocking curves; the formation of debris consisting of edge dislocation dipoles and dense, closed, prismatic loops evoked interpretation in terms of excessive cross slip in silver and the interaction of basal and pyramidal slip in zinc.

It is clear that the x-ray DCD techniques are capable of revealing fine, microstructural changes that are not normally observable with other techniques, or are obscured by the inseparability of competing mechanisms. The DCD arrangement can be employed to study single crystals, pure polycrystalline metals, and multiphase alloys with mutual ease and equal promise. The method offers good resolution of the local effects in individual grains, but also provides information from a sufficient number of grains to permit accurate statistical analysis of an average or mean microstructural response. The film-recorded reflections represent an imaging of the subdomain structure which can also be interpreted quantitatively in terms of the excess dislocation density, which is known to be a factor in the accumulation of fatigue damage and the initiation of ultimate fracture. The intent of the present study will be to exploit these aspects of the method to isolate a suitable microstructural indicator of progressive fatigue damage, and thereby contribute to the capability for accurate fatigue life and failure prediction. In accomplishing this objective, the DCD method is particularly useful for the microstructural analysis of the surface and bulk. Analysis of these regions can be carried out independently, in a stepwise manner, by incremental removal of surface layers. In addition, nondesctructive in-depth analysis is made possible by altering the depth of penetration of the incident radiation. This potential may be very important in technological applications when service components are to be examined.

II. OBJECTIVES

The complexity of metal fatigue processes, probed by the diverse macroscopic and microstructural characterization methods described in the previous sections, serves to heighten the urgency to identify the real causes of cyclic damage. The results of previous investigations have fueled a growing controversy regarding the role of particular substructural entities in the accumulation of fatigue damage and ultimate failure. It is thus the primary goal of this study to provide experimental evidence to support a more comprehensive and unambiguous theory with respect to the accruement of cyclic damage, and then to test it for the prediction of eventual failure.

Based on the preceding discussion, the approach to the problem will consist of three phases:

1. Microstructural evidence will be sought to determine whether or not there is a universal propensity for perferential work hardening of the surface layer as compared to the bulk material, under both static and dynamic loading conditions.

2. Differences in the structural response to the monotonic and cyclic modes of deformation will be disclosed, particularly with respect to the stability and interactive effects associated with the surface and bulk regions.

3. New information and knowledge gained through these investigations will be utilized to develop new criteria for fatigue life estimation.

A. MICROSTRUCTURAL CONFIRMATION OF SURFACE LAYER WORK HARDENING

Since it is well known that the initial condition of a specimen's surface is of vital importance to its fatigue performance and resistance, many previous studies have focused on the cyclic development of surface relief and other topological processes contributing to the onset of fracture. The research devoted to elucidation of fatigue-induced microstructural changes, such as those participating in hardening and softening phenomena, often failed to differentiate among the processes specific to the surface and bulk regions. The scientists who did recognize a difference between surface and bulk mechanisms found it difficult to distinguish

which features could be best associated with actual fatigue damage. Thus, the cause-and=effect relationships between microcracking and the underlying defect structure in the surface layer, and between subdomain formation and microstrain in the bulk, for instance, were hard to justify in terms of ultimate failure.

The first objective of the present research is to generate concrete microstructural evidence to confirm previous mechanical stress measurements which have shown that the surface layer may be subject to preferential work hardening during plastic deformation. To achieve this end, x-ray double-crystal diffractometry will be employed as the principal research tool. By incremental removal of surface layers, the defect concentration and distribution will be characterized as a function of depth from the surface. The study will encompass an analysis of four model materials: low-SFE silicon single crystals, deformed at elevated temperature; aluminum single crystals, typical of the class of high-SFE, ductile, fcc metals; gold monocrystals, which have little propensity for oxide formation; and Al 2024, as a typical, commercial, precipitation-hardened alloy. It is hoped that the elucidation of a surface work hardening process in these materials will assure the universal nature of the behavior, and thus contribute to the understanding of accrued damage and failure mechanism under varied modes of plastic deformation.

B. TESTING THE "SURFACE BARRIER MODEL" FOR FATIGUE DEFORMATION

The analysis of surface work hardening induced by simple tension will be extended in this phase of the investigation to include alternating tension-compression fatigue. By carrying out a thorough examination of the defect configuration as a function of distance below the specimen surface, by systematic surface layer removal, the substructural response to the two modes of deformation will be compared. In this way, it is hoped that evidence will be generated to test the "surface barrier model" for the accumulation of damage under dynamic stressing conditions[115].

An attempt will also be made to evaluate the structural stability of the defect configuration produced by repeated loading. The microstructural response during cycling will be studied by intermittent x-ray diffraction analysis, before and after polishing away the surface layers.

The objective of these experiments will be to contribute to the understanding of some of the apparent anomalies of fatigue processes, such as cyclic recovery and softening, life extension by surface polishing or removal treatment, and the cold working observed for metals tested even in the "safe" range of stresses.

C. DEVELOPMENT OF NEW CRITERIA FOR FATIGUE FAILURE PREDICTION

The application of traditional x-ray pattern asterism or line broadening analysis has been shown to be inadequate for predicting the onset of fatigue failure. It is proposed that the deficiencies of past efforts to predict the fatigue life derive from the collective treatment of surface and bulk substructural entities induced by fatigue. It is presumed that if the "in-depth" and structural stability experiments comprising the first two phases of the investigation are successful in decoupling the surface and bulk responses, it will be easier to understand how they work together to contribute to the final structural instability at failure.

The final phase of the research will therefore be designed to apply the information from the "in-depth" studies to define the progression towards crack initiation and fracture. An attempt will then be made to explore the response in depth, nondestructively, and to develop a simple and accurate method for predicting the total life span and/or remaining fatigue resistance of cycled metals.

III. EXPERIMENTAL PROCEDURE

A. SINGLE-CRYSTAL STUDIES

1. Tensile Deformation

Single-crystal specimens of silicon, aluminum, and gold were prepared for the experiments involving simple tensile deformation. Cylindrical single crystals of aluminum and silicon were sliced into thin wafers after orientation by means of the Laue back-reflection x-ray diffraction method. Shoulder-type tensile specimens, as shown in Figures 8a and 8b, were cut from the wafers using a Servomet spark-erosion apparatus. The silicon specimens had a (112) surface orientation and a [110] tensile axis. The surface orientation and tensile axis directions for the aluminum specimens were (100) and [100]. The gold specimens were prepared by Windsor Metalcrystals, Incorporated, and all consisted of several large grains of indeterminate orientation. One of the specimens chosen for inclusion in the study had a large grain which constituted a major portion of the gage length, such that the [123] crystallographic direction nearly coincided with the tensile axis. The (311) crystal planes were oriented at an angle of about 11° to the surfaces of the square cross-section specimens, as shown by Figure 8c.

Surface damage was removed from the silicon specimens by lapping with 600 grit silicon carbide, followed by chemical polishing (1 part HF, 3 parts HNO_3, 2 parts CH_3COOH). The aluminum specimens were reduced to the desired thickness by spark-erosion planing and subsequent electropolishing at -5°C (1 part HNO_3, 3 parts CH_3COOH). The gold specimens were electropolished at ambient temperature in a Thiorea solution. At least 70 μm were removed in the final chemical or electropolishing step to insure damage-free surfaces[165]. The aluminum specimens were annealed at 600°C for 20 hours in a protective argon atmosphere to relieve the internal stresses introduced during preparation.

All the specimens were deformed on an Instron universal tester. The silicon specimens were mounted in loading grips equipped with ceramic fittings designed to both clamp the specimen ends and provide shoulder support on application of the load. After mounting in the grips, a

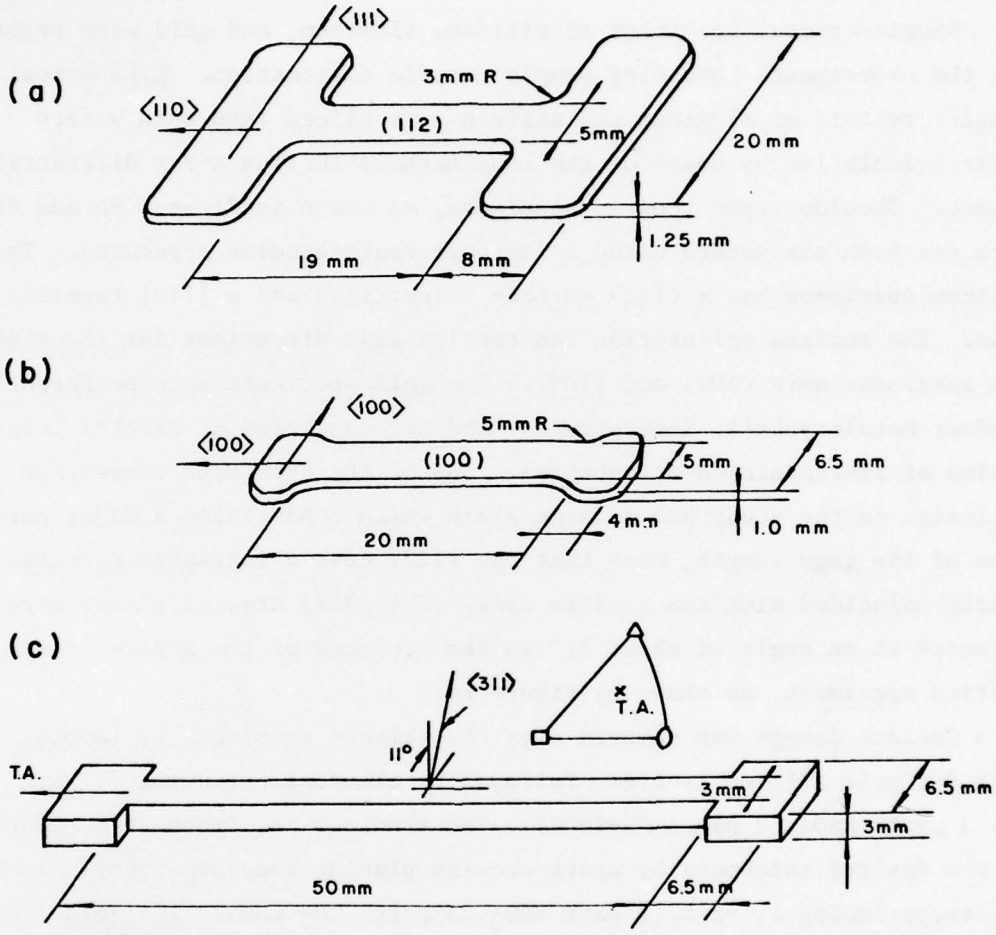


Figure 8. Specimen configurations employed in the tensile tests of single crystals: (a) silicon specimens - mounted in combination clamp and shoulder-support grips, with ball-bearing connection to the loading rods; (b) aluminum specimens - clamped in ball-bearing mounted grip assembly; (c) gold specimens - installed with rigid, clamp-style loading fixture.

cylindrical, high temperature furnace was lowered into position to enclose the specimen and brought to a temperature of 750°C with an argon atmosphere. The deformation was carried out at a strain rate of 5.9×10^{-5} sec^{-1} to a plastic strain level of 10%, followed by unloading and cooling in a stream of argon. The aluminum specimens were clamped into a grip assembly provided with a rigid, removable jig to prevent accidental deformation during installation in the Instron equipment, and ball-bearing connections to the loading rods to prevent twisting during the extension. The specimens were pulled to 10% plastic strain at a rate of 3.3×10^{-3} sec^{-1} while cooled to below 0°C in a steady stream of liquid nitrogen vapor. After testing, the aluminum crystals were held at a temperature of -5°C by refrigeration. The gold specimens were mounted in a rigid clamp-style arrangement in the Instron tester. Under the restrictive gripping conditions, the deformation was limited to 3% plastic strain at a rate of 1.7×10^{-5} sec^{-1}.

The defect concentration and distribution as a function of distance from the free surface of the deformed specimens were obtained by incrementally removing the surface layers and performing x-ray diffraction analysis at each depth. The layers of 25- to 75 μm thickness were polished away with the chemical or electropolishing procedure used for each of the crystal species in the damage removal step. The x-ray analysis of the silicon and gold monocrystals was performed at ambient temperature. The aluminum single crystals were mounted on a copper cooling block fitted to the diffractometer goniometer head. The temperature during x-ray analysis, measured by attaching a thermocouple to the grip section of the specimen, was maintained at 3 to 5°C by a flow of ice water pumped through the cooling block.

2. Dynamic Testing

Rod-shaped aluminum single crystals were obtained from Windsor Metalcrystals, Incorporated, with [100] axis orientation. Cylindrical fatigue specimens were fabricated from the rods by lathe operations. The specimen shape and gripping arrangement are shown in Figure 9. A cold worked layer totaling 150μm in thickness had to be removed from the specimens by electropolishing to eliminate the damage due to machining.

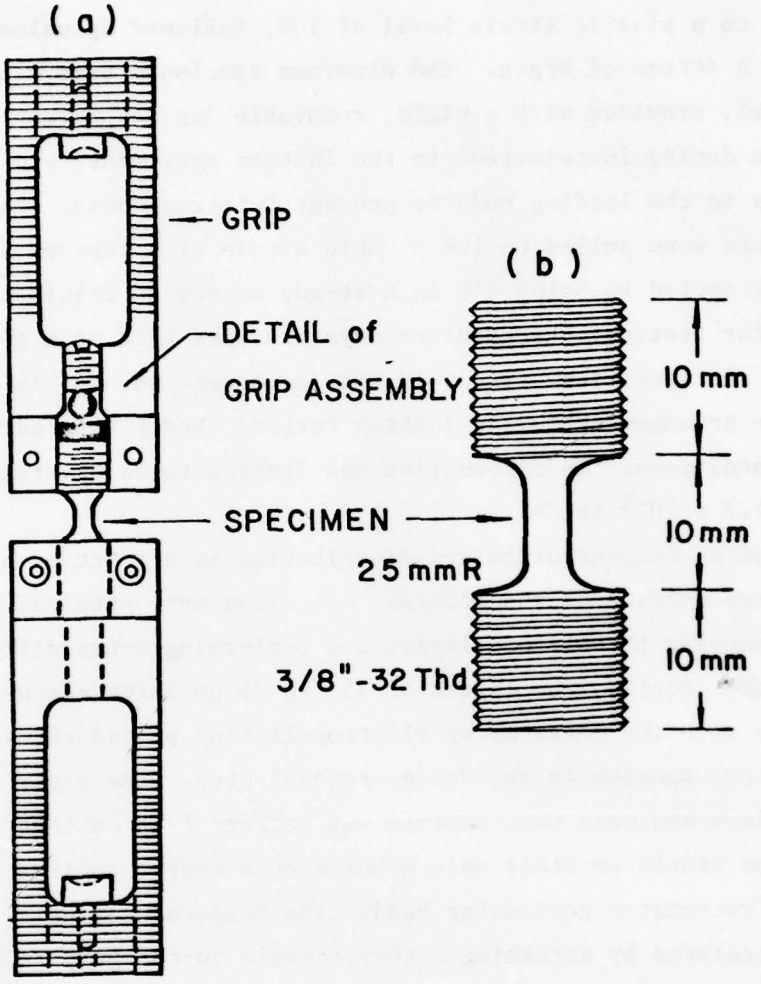


Figure 9. Specimen configuration and grip assembly employed in the fatigue investigations of Al single crystals and Al 2024 alloy: (a) specimen mounted in grips used for both static (tensile) tests with a ball-and-socket arrangement, and dynamic (push-pull fatigue) testing by clamping to a similarly serrated loading fixture; (b) cylindrical fatigue specimen - fabricated with 4.5 mm gage diameter for the single crystals, and 3.0 mm for the alloy specimens.

The tensile properties of the specimens were determined by static testing on an Instron universal testing machine. The specimens were mounted in a ball-bearing grip assembly with a removable support jig to prevent handling damage. The threaded grips were split into halves and fitted with connecting screws to facilitate direct installation and removal of the specimens without accidental twisting. The fatigue cycling was carried out on a Tatnell-Krause apparatus fitted with a 100-lb load bar. The specimens were cycled at 15 Hz employing tension-compression, zero-mean loading. The grips used in the tensile testing were provided with horizontal saw teeth to match those on the fixtures at the end of the carefully aligned fatigue machine loading rods. This feature insured the minimization of specimen torque and bending moments during the testing. The axial force applied to the specimen by flexure of the eccentrically mounted load bar was calibrated beforehand by means of constantan strain gages mounted at 90° intervals about the circumference of an eleastically loaded steel specimen.

Specimens were fatigued 2×10^5 cycles at a stress amplitude of 1.03 MPa, for which no failure occurred if cycling was carried to 10^7 cycles. They were then analyzed in depth by x-ray diffraction, employing incremental surface layer removal by electropolishing.

3. X-ray Diffraction Analysis

X-ray double-crystal diffractometry (DCD), combined with (B-B) reflection topography, was employed as the principal research tool for analysis of the defect structure introduced to the single crystals by monotonic and fatigue testing. The DCD geometry is illustrated in Figure 10a. The primary beam is reflected by a highly perfect monochromating crystal and passes through a long collimator and a series of defining slits prior to incidence on the test specimen. The technique may be applied in either a transmission (Laue) or reflection (Bragg) arrangement. Analysis of the surface layers of the test crystal is best facilitated by using the symmetric Bragg reflection arrangements shown in Figure 10b. The single-crystal specimen is rocked about an axis which lies in the plane of the reflecting surface, and normal to the plane of parallelism. For an in-depth analysis, care must be taken to maintain the position of

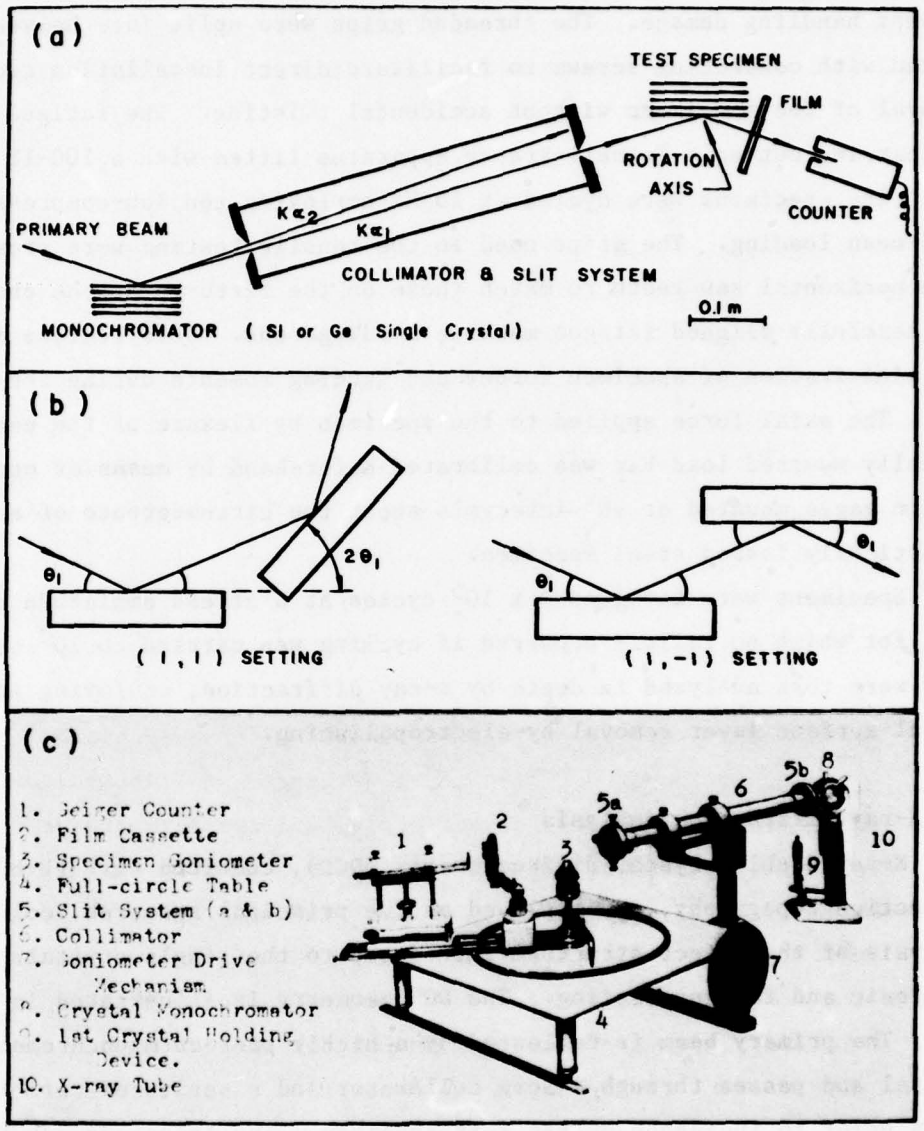


Figure 10. X-ray double crystal diffractometer for single crystal analysis: (a) schematic diagram of the diffraction geometry; (b) illustration of the antiparallel (m,n) and parallel (m,-n) settings; (c) photograph of the complete diffractometer assembly.

the rotation axis at the specimen surface as the surface layers are incrementally removed. The rocking procedure produces an increasing and then decreasing measured intensity as the crystal planes pass through their ideal reflecting position. The intensity variation over the range of reflection constitutes the "rocking curve profile" for the region analyzed.

In this investigation a "dislocation-free" silicon crystal with a (111) orientation was used as the first monochromating crystal. Copper radiation was employed, and the $K\alpha_2$ component was eliminated with a knife-edge. Since the silicon test crystal had a (112) surface orientation, the reflection geometry approximated a parallel condition, denoted (1,-1) in Figure 10b, and for which the normals to the crystal surfaces are opposite in direction. Any deviation from this condition is represented symbolically by $(m_x,-n_y)$, where m and n connote the order of reflection, and x and y refer to the first and test crystal, respectively. The aluminum specimens with a (100) surface orientation, and the gold specimens for which the (311) reflection was used, also corresponded approximately to the parallel arrangement. The parallel setting was employed to minimize the wavelength dispersion.

By maintaining incident beam dimensions of 0.2-mm width and 1.2-cm height, a large portion of the specimen gage length contributed to the rocking curve profiles, assuring an effective averaging of the deformation response without sacrificing angular resolution. Rocking curves were also recorded with the beam length normal to the specimen tensile axis and a slightly wider slit separation. Evaluation of the profile shapes and breadths revealed little difference for the two geometric configurations. B-B topographs were taken at angular rotation intervals along the rocking curves by moving a film into position close to the specimen to intercept the reflected beam in front of the counter as shown in Figure 10c. By suitable translation of the cassette after exposure at each angular position, a mapping of the substructural contributions to the intensity profile was obtained.

X-ray rocking curves were first recorded for each of the three crystal species in the polished and undeformed condition. After tensile deformation, x-ray analysis was performed at the original surface and

after removal of appropriate layer thicknesses. The maximum penetration of the CuKαa_1 radiation was 24.6, 14.5, and 0.7 μm for silicon, aluminum, and gold, respectively [see Appendix A, Sect 1]. These values therefore represent the total distance from the surface for which the defect concentration was averaged by the rocking curve analysis after each removal of a layer thickness.*

The cylindrical aluminum single crystals used in the fatigue studies** were oriented by the back-reflection Laue method to identify the position of the (100) planes lying parallel to the tensile axis. This permitted more rapid location of the diffraction peak in the full-circle diffractometer. The specimen was positioned so as to achieve a glancing incidence of the incident beam on the specimen surface conforming to a parallel-type arrangement. The cross section of the incident beam had dimensions 4 x 0.5 mm, and the maximum penetration distance varied with the take-off angle from the cylindrical surface, from zero to 7.25 μm in depth [see Appendix A, Sect 2].

As will be discussed in more detail in conjunction with the actual experimental results, the combination of DCD rocking curves and B-B topography yields substantial information regarding the microstructural response to the deformation process. The successive topographic images recorded over the reflection range provide a unique qualitative correlation between the defect structure and the minute intensity fluctuations constituting the overall rocking curve profiles. The breadth of the rocking curve, on the other hand, is a qualitative measure of the relative misorientation of deformation induced subdomains and the misalignment within them. These substructrual features are related primarily to the generation and interaction of excess dislocations of one sign. To calculate the cancentration or density of excess dislocations from the x-ray

---

*It should be noted that, for the curves presented in the results section plotting the x-ray data as a function of depth, the origin of the abscissa corresponds from a rigorous viewpoint to the mean penetration of the radiation; i.e., to a distance from the surface equaling half the maximum penetration of copper radiation for each crystal specie.

**The author was assisted in the single-crystal fatigue studies by T. Takemoto.

data, it is necessary to make some assumptions regarding the defect distribution and to define a consistent method for evaluation of the rocking curve breadth. The former will be taken up in the Discussion section, but it is appropriate to describe the breadth measurement method here. For the purposes of this investigation, the rocking curve "half-width," or its angular breadth at half of the peak's intensity maximum, provided an easily measurable parameter for use in the calculation. Identical to the "half-value breadth," as it was denoted in the Taira studies[117], the halfwidth is controlled principally by the tilts and/or curvature produced by accumulation of excess dislocations and excludes the broadening of the profile tails caused primarily by point defects and other singular microstructural entities[155]. The "Laue integral breadth," defined as the integrated to peak intensity ratio, was also measured for the single-crystal studies. While this parameter offers some advantage by avoiding the complications due to shoulders and other asymmetries of the diffraction peak, its value and sense of change with deformation extent or depth were always consistent with that of the corresponding halfwidth. Since its value could not be determined for the subsequent studies of polycrystals, the data listed throughout the Results section were restricted to the halfwidth parameter.

B. Al 2024 ALLOY STUDIES

1. Incremental Fatigue Cycling

The Al 2024 alloy was obtained in two separate batches of bar stock with composition in weight percentage: 3.99 Cu, 1.35 Mg, 0.50 Mn, and an impurity content totaling about 0.5 wt% consisting principally of Fe, Si, Zn, Ti, and Cr. The stock was fabricated into cylindrical fatigue specimens with the configuration shown in Figure 9. The specimens were mechanically polished to remove the surface irregularities caused by the lathe operations, using successively finer grades of emery paper. The two batches were then given a solution heat treatment in a tilting furnace at 495°C in an argon atmosphere or encapsulated in evacuated quartz ampoules. After quenching in ice water the specimens were given a second mechanical polishing, this time with 5.0, 1.0, and 0.05 μm particle

size alumina. Some of the specimens from each batch were set aside for grain size analysis, tensile property determination, and surface microscopy. The balance of the specimens to be used in the x-ray analysis was given a final electropolishing. At least 100 μm was removed from the gage diameter to eliminate any remaining surface damage, employing either of two electrolytic solutions: 1 part $HClO_4$, 9 parts CH_3COOH; or 1 part HNO_3, 3 parts CH_3COOH. The specimens retained for grain size analysis and surface microscopy after cycling were specially prepared with a flat region on their gage sections. The planar region with dimensions 6 x 1.5 mm was produced by spark-erosion planing. The surface damage induced by this procedure was then removed with a final electropolishing. After etching with Keller's reagent, the grain sizes for the two batches were determined by the linear intercept (Hyne) procedure[166], applied to 40, 100, and 200X photomicrographs. The tensile properties of specimens from the two batches were characterized using an Instron universal tester. The elastic limits were obtained employing a strain rate of 1.3×10^{-4} sec^{-1}.

The specimens from batch A, which will be used to denote the larger grain size stock, were fatigue cycled in the push-pull mode with zero mean stress using a 500-lb load bar on the Tatnell-Krause fatigue apparatus. At least three specimens were tested to failure at each of three constant load amplitudes corresponding to ±1.0, 0.75, and 0.50 of the proporational limit, $\sigma_{p.l.}$, to generate a representative S-N curve for the batch. A similar procedure was used for the smaller grain size batch B specimens, but these were tested on newly acquired Instron servohydraulic fatigue equipment (model 1350). For this batch, the cyclic amplitudes corresponded to ±1.0, 0.75, 0.60, and 0.50 of its respective elastic limit. The cyclic frequency was maintained at 10 Hz in all the tests, except for periods of 10- to 100-cycle duration during the fatigue of batch B specimens, for which the frequency was gradually reduced to 1 Hz for hyteresis loop observation.

The incremental fatigue experiments for batch A were carried out by stepwise fatigue of at least two specimens at each stress level. After each fatigue increment, the cycling was interrupted to allow for x-ray analysis of the specimen surface, followed by remounting in the fatigue

machine for the next cycling period. The sampled increments represented regular fractions of the expected total life, as drawn from the previously obtained S-N data. After eventual failure, these fractions were adjusted to reflect the true percentages of the actual life span of each specimen.

The incremental fatigue analysis of batch B specimens was accomplished slightly differently. In this case, two specimens were cycled to each of the chosen fractions of the life, namely 5, 25, 50, 75, and 95% of the expected life, at a single stress amplitude corresponding to the proportional limit. The high degree of reproducibility afforded by the servohydraulic equipment permitted assumption that these fractions of life, derived from the S-N data, conformed reasonably well to the fractions of the actual life spans of the individual specimens. After the predetermined amount of cycling was completed, the specimens were simply dismounted from the fatigue machine for subsequent x-ray analysis.

2. Damage Gradients from Surface to Bulk

In order to determine the defect concentration and distribution as a function of the distance from the specimen surface, a stepwise surface removal and x-ray analysis procedure, similar to that employed in the single crystal studies, was applied to study the fatigued alloy specimens. Batch A specimens were cycled to arbitrarily selected fractions of the predetermined average fatigue lives at amplitudes equal to 1.0 and 0.5 of the proportional limit. After testing, the specimens were removed from the fatigue apparatus for x-ray analysis of the original surface. Layer thicknesses of 50 to 100 μm were subsequently removed by electropolishing, accompanied by intermittent x-ray analysis at each depth. To generate a representative "depth profile" of the damage gradient from surface to bulk, this procedure of thickness removal followed by x-ray analysis was continued until no further change in the x-ray data was apparent. The invariance of the x-ray data was found to occur at a depth of 200 to 400 μm into the bulk. A protective microstop lacquer was then applied to half of the gage section circumference along the full length of the test specimens, and electropolishing was continued to a depth of 1500 μm from the original surface, or approximately the center of the specimen. A final x-ray data point was recorded for this depth to

assure the constancy of the defect concentration throughout the bulk region of the specimen.

3. Surface Removal and Recycling

The procedures just described were designed to analyze the deformation response in the surface layers and bulk material during incremental fatigue cycling to failure. In order to investigate the stability of the induced microstructure, it was decided to measure the cyclic response of the bulk in the absence of the surface layer. To this end, several batch A specimens were cycled to 75 and 95% of the predetermined life span at an amplitude equivalent to the static proportional limit. The damage gradient from the surface to a depth of 400 μm was obtained by the stepwise polishing and x-ray analysis sequence outlined in the previous section. This procedure served both to generate standard depth profiles for the precycled specimens and to eliminate completely the original surface layers. The specimens were then reinserted in the fatigue machine for continued cycling at the same amplitude as before. The recycling was interrupted after intervals of short duration, ranging from 0.2 to 3% of the normal fatigue life, to permit intermittent x-ray analysis of the "new" surface. After the recycling intervals totaled 5% of the normal life, the specimens were either cycled continuously to failure or subjected to a second depth profile analysis sequence. The former allowed the change in the total fatigue life afforded by surface layer removal to be determined. The latter permitted the elucidation of the change in defect concentration and distribution in the reduced gage section, induced by recycling in the absence of the original surface layer.

4. X-ray Diffraction and Surface Microscopy

The special DCD method for polycrystalline materials[167] was used to measure the alloy's microstructural response to fatigue cycling. Figure 11a presents a schematic illustration of the diffraction geometry. The polycrystalline specimen is irradiated by a crystal-monochromated beam. Each reflecting grain is considered to function independently as the test crystal of a double-crystal diffractometer. For a stationary specimen position, the spot reflections for the individual grains are

recorded along the Debye arcs on a cylindrical film. Depending on the perfection of the grains, the specimen is rotated or rocked in angular intervals of 1 to 10 minutes of arc, over a total range of 1 to 2°. To separate the spots corresponding to successive rotation positions, the film is shifted or translated slightly after each exposure. This multi-exposure technique gives rist to an array of spots for each reflecting grain, as shown in the film reproduction in Figure 11b. These arrays of spots, with their intensity dependence on the angular position, are pictorial representations of the rocking curves of the reflecting grains. The shape of the spots within an array is thus a visual manifestation of the penetration of the Ewald's sphere by the reciprocal lattice point which, owing to the lattice defects, is enlarged to a reciprocal lattice volume. The latter depends on the transformation of the shape factor from physical to reciprocal space. Thus, if the grains contain a sub-structure, the intensity distribution of the arrays will be broad and multipeaked, both in the horizontal direction and along the azimuthal, or vertical elevation. As a result of reflection from the first monochromating crystal, the irradiating beam is geometrically parallel in the horizontal plane, or the plane of the diffractometer. Thus, by photometrically scanning an array from spot to spot in the horizontal direction, the film density or blackening for each spot is recorded as a separate peak on the microphotometer chart. After adjusting each spot's peak blackening to represent the true intensity via a predetermined film density-to-intensity calibration curve, the plot of the spot intensities against their angular separation constitutes a normal rocking curve for the particular grain analyzed. From the angles subtending successive peaks of the rocking curve, the excess dislocation density in the subgrain boundaries can be determined, while, from the spread of the subpeaks, the excess dislocation density within the subgrains can be obtained. As in the single-crystal studies, the width, β, at half of the intensity maximum of the entire rocking curve, provides a measure of the excess dislocation density in the grain causing the statistical distribution of subdomain tilts comprising the overall misorientation in the grain[161].

Since the incident beam impinges on a large portion of the gage section, a large number of grain reflections are recorded in a single

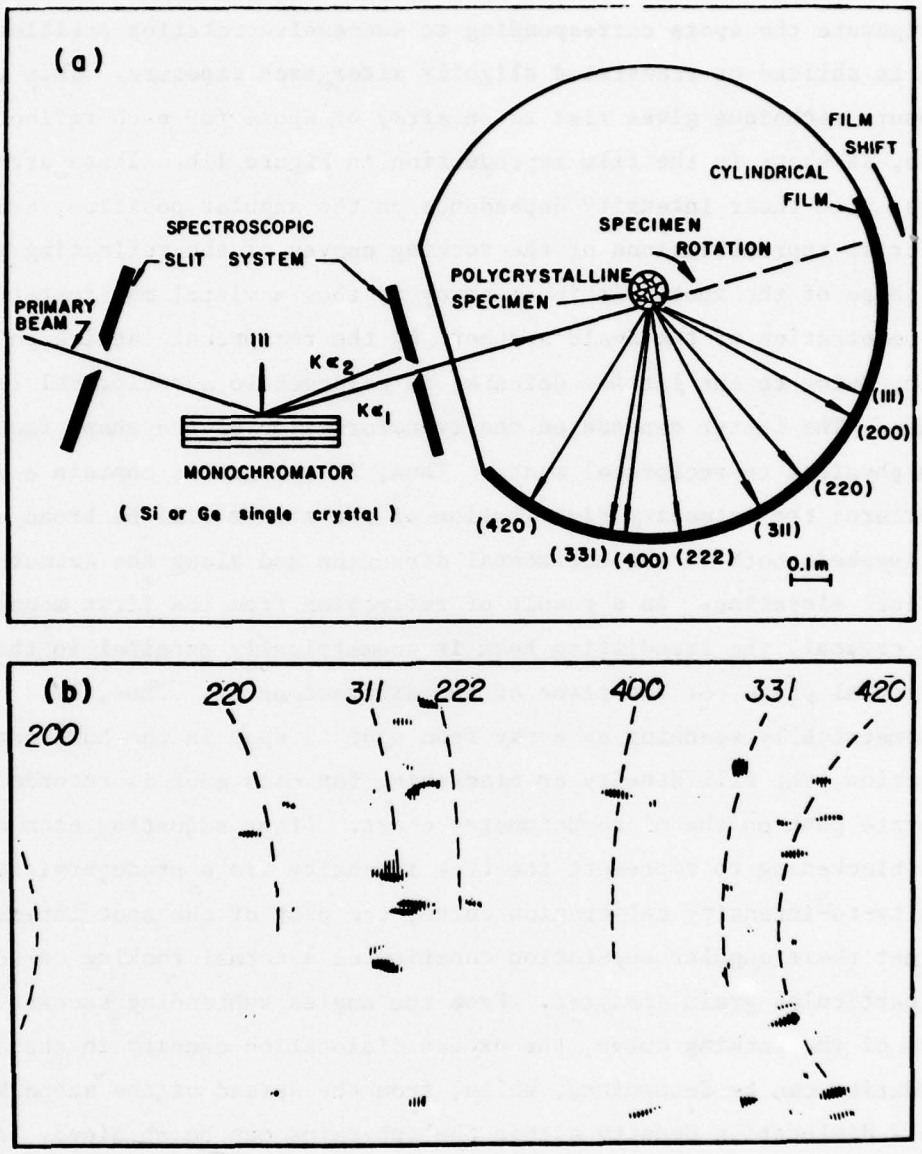


Figure 11. X-ray double crystal diffractometer for polycrystalline metals: (a) schematic diagram of the diffraction geometry and x-ray camera; (b) developed x-ray film showing grain reflections along the Debye arcs.

exposure sequence. By analyzing the rocking curves from various (hkl) reflections in the manner described above, a representative statistical parameter, β_m, is generated to describe the mean defect concentration of the grain population. Furthermore, by taking B-B topographs close to the specimen and performing a spacial tracing of the images outward to the spot reflections of the Debye pattern, the rocking curves of the individual grains can be correlated to their topographic relationship on the specimen surface[161].

Two additional characteristics of the Debye patterns generated by the polycrystalline specimens, while incidental to the current investigation, are nevertheless noteworthy. First, since the x-ray beam is essentially parallel in the horizontal plane, the halfwidth, β, can be determined only by carrying out a complete sequence of incremental specimen rotations. The vertical divergence of the primary beam, however, remains unaltered after reflection from the first monochromating crystal. The unrestricted divergence of the beam in this direction allows it to effectively rock over the grains during each discrete exposure. The azimuthal intensity variation which results also provides a measure of the breakup and induced substructural strain of each grain. The vertical spread of the spots on the film recorded in a single exposure, combined with their respective angular distance from the equatorial line, lying in the horizontal plane of the diffractometer, can be used to calculate the azimuthal spread, $\Delta\psi$[159] [see Appendix B, Sect 2]. A second consequence of the DCD arrangement for polycrystalline materials is the substructural information which can be derived from the angular relationship of the spots due to the $K\alpha_1$ and $K\alpha_2$ spectral components. For the antiparallel arrangement, the angular separation of the two components, or doublet split, produced by diffraction from the first and test crystals, is additive. For the parallel arrangement, on the other hand, the resultant doublet split for a given (hkl) refaection as the difference between that of the test crystal and that of the monochromator. The magnitude of the dispersion for each arrangement increases with reflection angle; thus, when the total divergence exceeds the misorientation angle associated with the crystal lattice, the reflection conditions for both components can no longer be simultaneously satisfied. By identifying the highest order of reflection for which both

components can still be detected for the two settings, one can successfully "zero in" on the average total misorientation inherent to the reflecting grains. The average disorientation of the individual subdomains contributing to the total misorientation in the grains can also be estimated if the misaligned subgrains have fairly well-defined boundaries. This misorientation or tilt angle is computed from the angular separation of the respective maxima of the $K\alpha_1$ and $K\alpha_2$ curves, manifested by the array of spot doublets generated during the specimen rotation.

For the purposes of the present fatigue study, the azimuthal broadening was calculated and compared with the horizontal distribution of misalignment to provide an initial confirmation of the isotropy of the fatigue induced misorientation in the grains. Once the isotropic behavior was established, the average azimuthal broadening was ascertained only to check its consistency with the horizontal range of reflection, and therefore the adequacy of the diffractometer alignment during the specimen rocking sequence. The vertical widths were not actually reported since the diffuseness of the spots and the uncertainty as to whether the image derived from one or more grain reflection made it a less accurate parameter by which to characterize the marginal distribution of misalignment. Neither of the characterization techniques related to the $K\alpha_1/K\alpha_2$ divergence were found applicable in the alloy studies. The intrinsically imperfect nature of the alloy grains, even after annealing, caused mutual reflection up to high diffraction angles where dispersion tended to diffuse the reflected intensity. Similarly, the internal strain of the subgrains caused the $K\alpha_1$ and $K\alpha_2$ peaks to coincide so that only through the intensity fluctuation of the $K\alpha_1$ component itself, during the rocking procedure, could the relative subgrain tilts be revealed.

Since primarily the horizontal breadth, β, was used for evaluation of the fatigue induced defect concentration and substructure, several additional comments regarding this parameter should be made. The angular range of reflection due to coherently reflecting domains can be accurately obtained only when the irradiating beam and the rocking curve for the grain have well-defined boundaries. This occurs at or near the equatorial plane. The distribution of photometric intensities at higher azimuth reflections is greatly modified by the vertical divergence of the beam

and is influenced by the velocity factor. Due to these instrumental broadening effects, the higher azimuth reflections become "smeared out" when the corresponding reciprocal lattice points traverse the Ewald sphere. Rocking curves for these reflections can be excluded entirely from the statistical analysis if the population of grain reflection arrays near the equator is sufficiently large to give a representative sampling of the lattice defects. However, if the population of grain reflections is not large enough, even when a larger specimen area is irradiated by enlarging the slit opening, then the higher azimuth reflections can also be used, provided the necessary ψ-corrections are carried out [see Appendix B, Sect 1].

Account should also be made for the systematic broadening with reflection angle. Exclusive of particle size broadening, which is insignificant when the subgrains are large enough to be individually resolved and analyzed with monochromatic radiation, the angular dependence of the broadening due to uniform lattice strain should vary proportionally to tan θ. Finally, some of the variation in the average breadths for the different (hkl) reflections and the variation among the breadths of the individual arrays within each Debye arc are produced by the crystallographic nature and inhomogeneity of the material response to deformation. The former type of variation frequently results, for instance, when the active slip planes exhibit a different average array breadth than the average rocking curve halfwidth measured for other (hkl) reflection arcs. The latter type of variation often occurs if the deformation is highly localized by such phenomena as persistent slip, void production, or microcracking, so that even the grains with nearly the same orientation will be subject to different degrees of broadening. This accounts for the deviation in halfwidths for arrays of a single Debye arc.

In the current investigation, the representative halfwidth for the alloy at any stage of the fatigue process, or any depth from the surface, was taken as the mean value of the measured arrays, β_m, irrespective of the reflection angle. In order to minimize the inconsistency of this parameter which might derive from dispersion effects or crystal anisotropy, a similar number of reflections were drawn from each of the Debye arcs for each computation. The nominal accuracy of the mean halfwidth

value was insured by restricting the statistical sample to arrays within small azimuthal limits. For analysis with copper radiation and beam dimensions of 8 x 0.5 mm, this permitted inclusion of 25 to 30 arrays in a single sampling. The contribution by instrumental broadening to the total breadth of an array located at the maximum allowed azimuthal elevation was about 4 minutes of arc [see Appendix B, Sect. 1]. The symmetry of the halfwidth distribution in each sample was confirmed by the equivalence of the mean and median values of the halfwidth, and slight inhomogeneities in the deformation response from grain to grain were therefore considered to have little impact on the analysis. The deviation in the mean halfwidth value for any two complete exposure sequences performed for different surface areas of each specimen was found to average ±3.6 minutes of arc, and was used to represent the error spread associated with any particular data point. Finally, the mean halfwidths after deformation were corrected for the intrinsic halfwidth, β_o, of the virgin specimens according to the relation, $\overline{\beta} = (\beta_m{}^2 - \beta_o{}^2)^{1/2}$, where $\overline{\beta}$ is the corrected halfwidth.

The progressive change in the halfwidths during cycling was correlated to the development of surface relief disclosed by surface microscopy. The specimens prepared with flat gage regions and cycled to regular fractions of the fatigue life were examined by both SEM and light microscopy. A light etch was used to enhance the optical resolution of the topographical features and to distinguish the individual grains comprising the surface layer. Other specimens were subjected to incremental electropolishing and intermittent optical examination to ascertain the penetration of surface microcracks, intrusions, and PSB's into depth.

5. Nondestructive X-ray Analysis in Depth

The final phase of the x-ray diffraction study of fatigued alloy specimens was designed to analyze the defect distribution with depth from the surface using a method by which the physical removal of surface layers could be avoided. Such nondestructive analysis was accomplished by choosing three different x-ray target metals which would produce K spectra

with different wavelengths, and therefore provide a variation in the penetration distance into the specimen interior. Chromium radiation ($\lambda_{K\alpha}$ = 2.291) and molybdenum radiation ($\lambda_{K\alpha}$ = 0.7107) were selected, in addition to the previously employed copper radiation ($\lambda_{K\alpha}$ = 1.542), to obtain three penetration distances differing by about an order of magnitude [see Appendix A, Sect 3]. As a result of the absorption characteristics and experimental reflection geometry, Cr radiation analyzed a layer ranging from the surface to a depth of about 6 to 12 μm, Cu radiation penetrated to a depth of 20 to 35 μm, and Mo radiation sampled the grain perfection from the surface to a distance of 125 to 350 μm into the bulk. Further differentiation of the depths from which the individual grain reflections emanate was afforded by correlation of each array to its reflection order. In general, it was concluded from the diffraction geometry that the back reflections were derived from greater depth than the forward reflections, while experiencing an identical degree of absorption. Thus, the most intense spot arrays recorded for the forward reflections could be presumed to emanate principally from grains located at shallow depths, while the least intense back-reflected arrays originated primarily from grains located in deeper regions from the surface.

The batch B specimens, prepared and tested in previous incremental fatigue experiments, were used in the analysis. Specimens cycled to 5, 25, 50, 75, 95, and 100% of the normal fatigue life at a load amplitude corresponding to the proportional limit were analyzed successively with the three characteristic wavelengths. By measuring the halfwidths as a function of the fraction of life for each type of radiation, progressive fatigue curves for each analysis depth could be constructed and compared.

A germanium single-crystal monochromator with a (111) surface orientation was substituted for the silicon single crystal used in the previous studies. This improved the reflected intensity from the first crystal by about 2.5 times for copper and chromium radiation, but theoretically reduced that for molybdenum radiation by a factor of 3.5 [see Appendix C, Sect 1]. Since for the longer wavelength Cr radiation only three Debye arcs were intercepted by the film, the average halfwidth, β_m, had to be calculated from a smaller sample of arrays. This incident

radiation also produced fewer spots per Debye arc due to its limited penetration [see Appendix C, Sect 2], all of which revealed a high diffuseness due to air scattering. To insure the reliability of the comparative data for different extents of cycling, supplemental average half-widths were determined for each of the Debye arcs independently. Then the corrected values, $\overline{\beta}_{hkl}$, were averaged and compared to the overall, corrected, mean value, $\overline{\beta}$, for consistency.

One last specimen was fatigued to 10^7 cycles at an amplitude corresponding to $0.33\ \sigma_{p.l.}$ and was analyzed with Cu and Mo radiation to examine the in-depth response of the alloy tested below its fatigue limit.

IV. RESULTS

A. SINGLE-CRYSTAL STUDIES

1. X-ray Rocking Curves of Tensile Deformed Si, Al, and Au Crystals

X-ray rocking curve analysis of single crystals deformed in the uniaxial tension mode revealed a definite propensity toward preferential production of imperfections in the surface layers. Evaluation of the surface rocking curve profiles of plastically deformed silicon, aluminum, and gold crystals showed a strain induced expansion of halfwidths over intrinsic or undeformed and annealed values, indicative of the introduction of lattice strain and misorientation. Investigation of the induced defect structure as a function of depth into the crystal from the original free surface also revealed that the halfwidths decreased as surface layers were polished off from all three crystal species. These results are summarized in Table 1.

Annealed and polished silicon crystals have a narrow, spike-shaped rocking curve profile with an intrinsic halfwidth, β_o, of only 15 seconds of arc for the (112) reflection, as predicted by dynamical theory's primary extinction concept for crystal lattices which approach "ideal perfection." After monotonic deformation to 10% plastic strain at elevated temperature, the halfwidths, both at the surface and in the bulk, show a dramatic increase over the initial undeformed value. As depicted in Figure 12a, the rocking curve profile at the surface becomes much broader and multipeaked, and the measured halfwidth increases to 15.6 minutes of arc. Of primary significance to this study, however, is the deformation induced dependence of the halfwidths on the distance from the surface into the crystal bulk. As rocking curves are recorded at successively greater depths from the original surface by incrementally polishing away the surface layers, they are found to become progressively narrower. The corresponding halfwidths decrease to a minimum at a distance of 100 to 150 μm from the surface and maintain a constant value further into the bulk. Figure 12b shows the typical narrower rocking curve obtained at a depth of 100 μm from the surface, with a halfwidth measuring about 6.2 minutes of arc. Therefore, while at the surface, the rocking curve halfwidths are

TABLE 1 - MEASURED X-RAY ROCKING CURVE HALFWIDTHS HALFWIDTH RATIOS, AND CALCULATED EXCESS DISLOCATION DENSITIES FOR THE SURFACE LAYERS AND BULK OF TENSILE DEFORMED SINGLE CRYSTALS

	Aluminum	Silicon	Gold
β_o; Undeformed	4.0 min of arc	0.25 min	6.0 min
ε_p	10%	10%	3%
β_s; Surface	14.0 min of arc	15.6 min	11.0 min
β_x	11.1 min (30 μm)	12.6 min (30 μm)	9.8 min (10-30 μm)
.	8.4 min (100 μm)	7.2 min (100 μm)	8.6 min (75 μm)
.	8.1 min (200 μm)	6.8 min (175 μm)	8.3 min (135 μm)
β_i; Bulk	7.8 min (300 μm)	5.7 min (250 μm)	8.1 min (220 μm)
β_s/β_o	3.5	62	1.8
β_i/β_o	2.0	25	1.4
β_s/β_i	1.8	2.5	1.3
ρ_o; Undeformed	1.83×10^8 cm^{-2}	3.98×10^5 cm^{-2}	4.06×10^8 cm^{-2}
$\overline{\rho}_s$; Surface	2.06×10^9	1.55×10^9	9.56×10^9
$\overline{\rho}_s/\overline{\rho}_i$	3.8	6.2	2.7

increased from the initial value by a factor of over 60 (β_s/β_o); those in the bulk increase by a factor of only 25 (β_i,β_o). The resultant decrease in the halfwidths from the surface to bulk (β_s/β_i) is thus on the order of 2.5:1, as shown in the "depth profile" for silicon in Figure 13a.

Virgin aluminum crystals are found to have a much larger inherent rocking curve halfwidth and associated lattice imperfection, characteristically about 240 seconds (4 minutes) of arc for the (100) reflection, or 16 times that of virgin silicon crystals. After 10% plastic deformation at 0°C the surface halfwidths expand by 3.5 times to 14 minutes of arc, and the interior curves increase in breadth by a factor of just less than

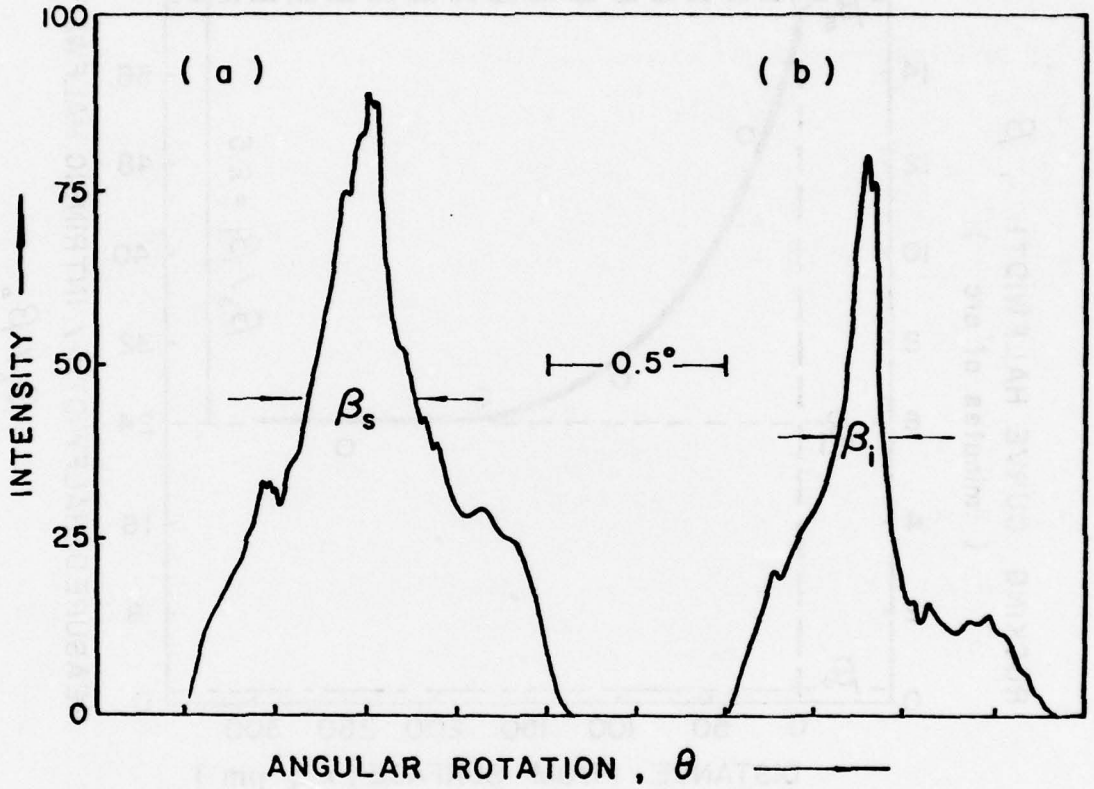


Figure 12. X-ray rocking curve profiles of tensile deformed silicon single crystal (ε_p = 10%, 650°C, tensile axis [110], (112) reflection, CuKα_1 radiation): (a) original surface, and (b) after removal of a 100-μm surface layer.

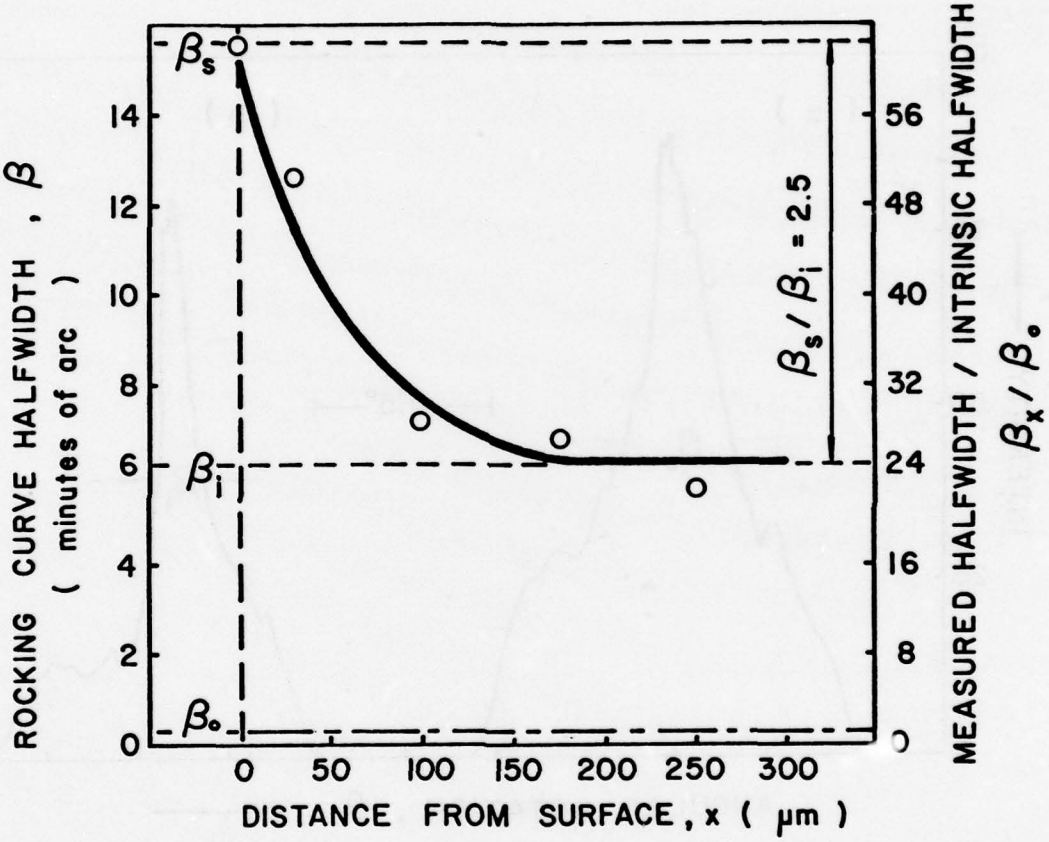


Figure 13a. Rocking curve halfwidths as a function of depth from the specimen surface for a silicon single crystal deformed by uniaxial tension (ε_p = 10% at 650°C, [110] tensile axis, and (112) reflection)

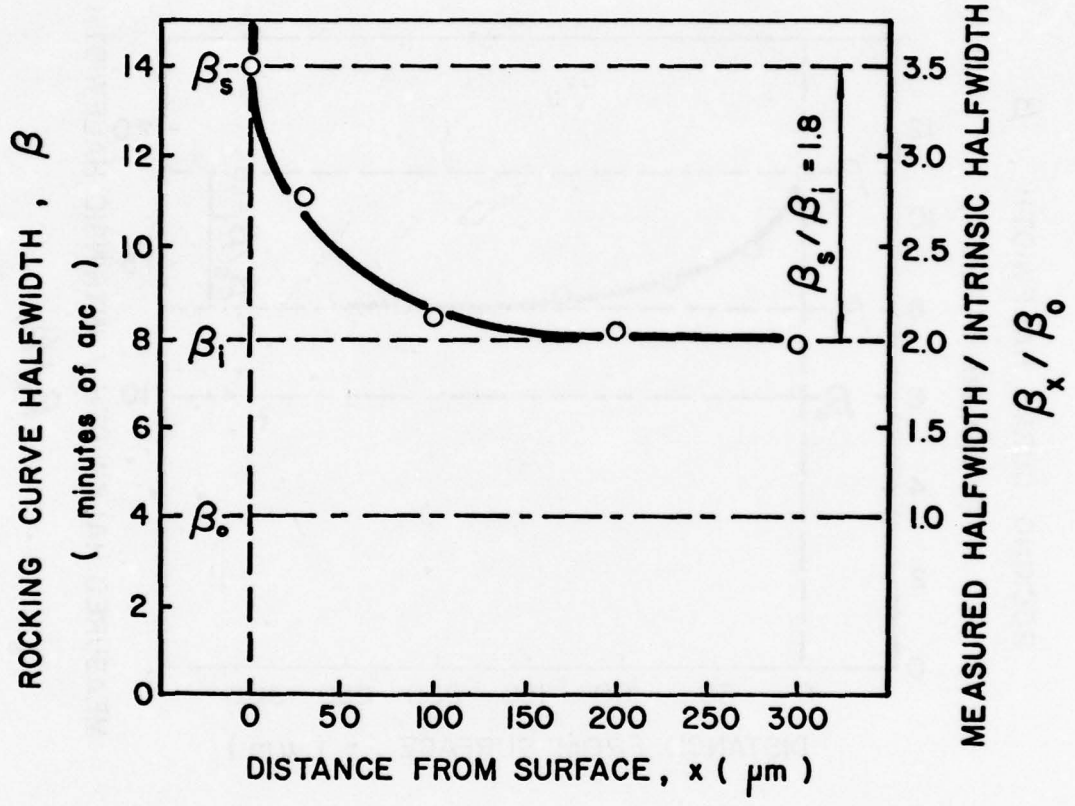


Figure 13b. Rocking curve halfwidths as a function of depth from the specimen surface for an aluminum single crystal deformed by uniaxial tension (ε_p = 10% at 0°C, [100] tensile axis, and (100) reflection)

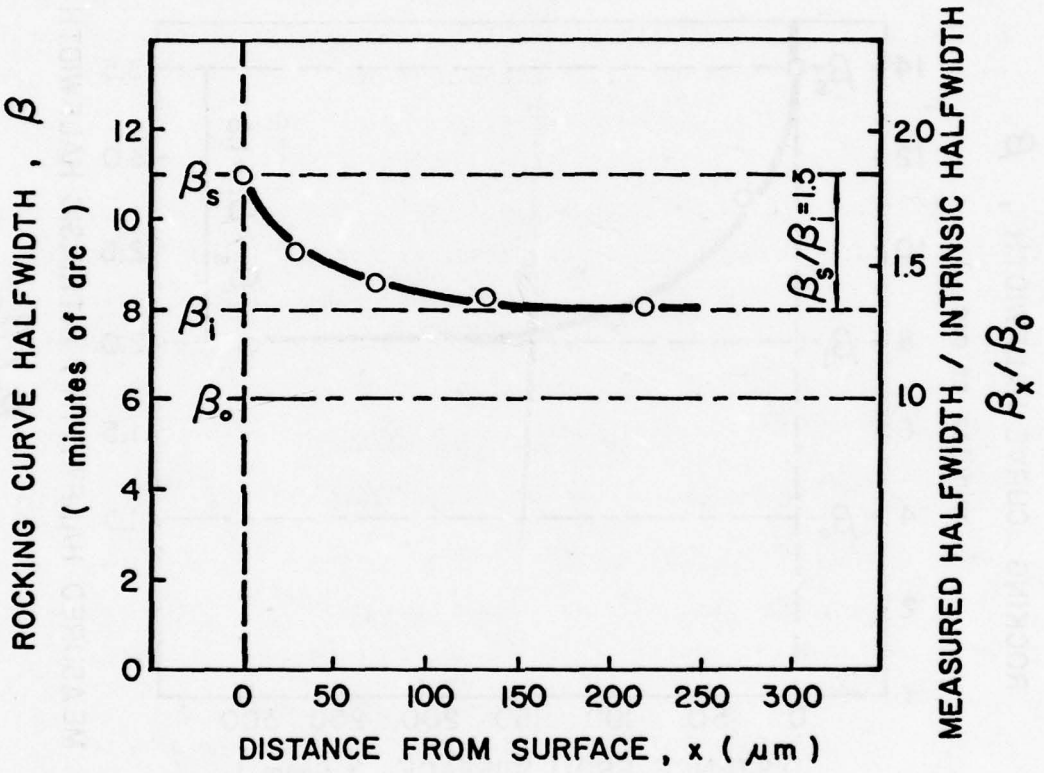


Figure 13c. Rocking curve halfwidths as a function of depth from the specimen surface for a gold single crystal deformed in tension (ε_p = 3%, ~[123] tensile axis, and (113) reflection)

2 to about 8 minutes of arc. Thus, the β_s/β_o and β_i/β_o values for aluminum average 1/15th of the relative halfwidth expansions exhibited by the surface layer and bulk regions of tensile deformed silicon. As illustrated by the depth profile for aluminum in Figure 13b, a decreasing halfwidth gradient with distance from the surface is again evident, giving a ratio of surface to bulk halfwidths, β_s/β_o, of about 1.8. A constant minimum halfwidth value is similarly established at a distance of about 150 μm from the surface.

Finally, gold single crystals exhibit an equivalent microstructural response to tensile deformation. Although pulled to only 3% plastic strain, compared to 10% for the Al and Si crystals, gold displays a significant deformation gradient, characterized by decreasing halfwidth values from a high of 11 minutes of arc at the surface, to a constant minimum of 8 minutes at the typical depth of 150 μm, measured for the (113) reflection. The reduced degree of plastic extension produces relative expansions of the surface and interior halfwidths of 1.8 and 1.4, respectively. The depth profile for gold in Figure 13c shows that the deformation gradient is manifested quantitatively by a halfwidth reduction from the surface to bulk by a factor of 1.3.

2. Rocking Curves and Topography of Tensile Deformed Al Crystals

In the previous section it was shown that x-ray rocking curves yield quantitative information with regard to deformation induced lattice imperfection and, with appropriate surface layer removals, reveal the defect distribution as a function of depth from the surface. In order to better understand the role of the surface and bulk during the early stages of tensile deformation, it is useful also to focus attention on the qualitative aspects of the rocking curve profiles, namely their overall shape and specific features as a function of angular position. This can be best accomplished by correlation with the topographic images of the reflecting lattice subdomains. Consequently, x-ray reflection topography was combined with the rocking curve analysis for the surface and bulk regions of aluminum single crystals pulled to 10% plastic strain.

Figure 14 shows typical rocking curves obtained for the deformed crystal at the surface and a depth of 100 μm. Beneath them are corresponding film-recorded topographic exposures taken at regular

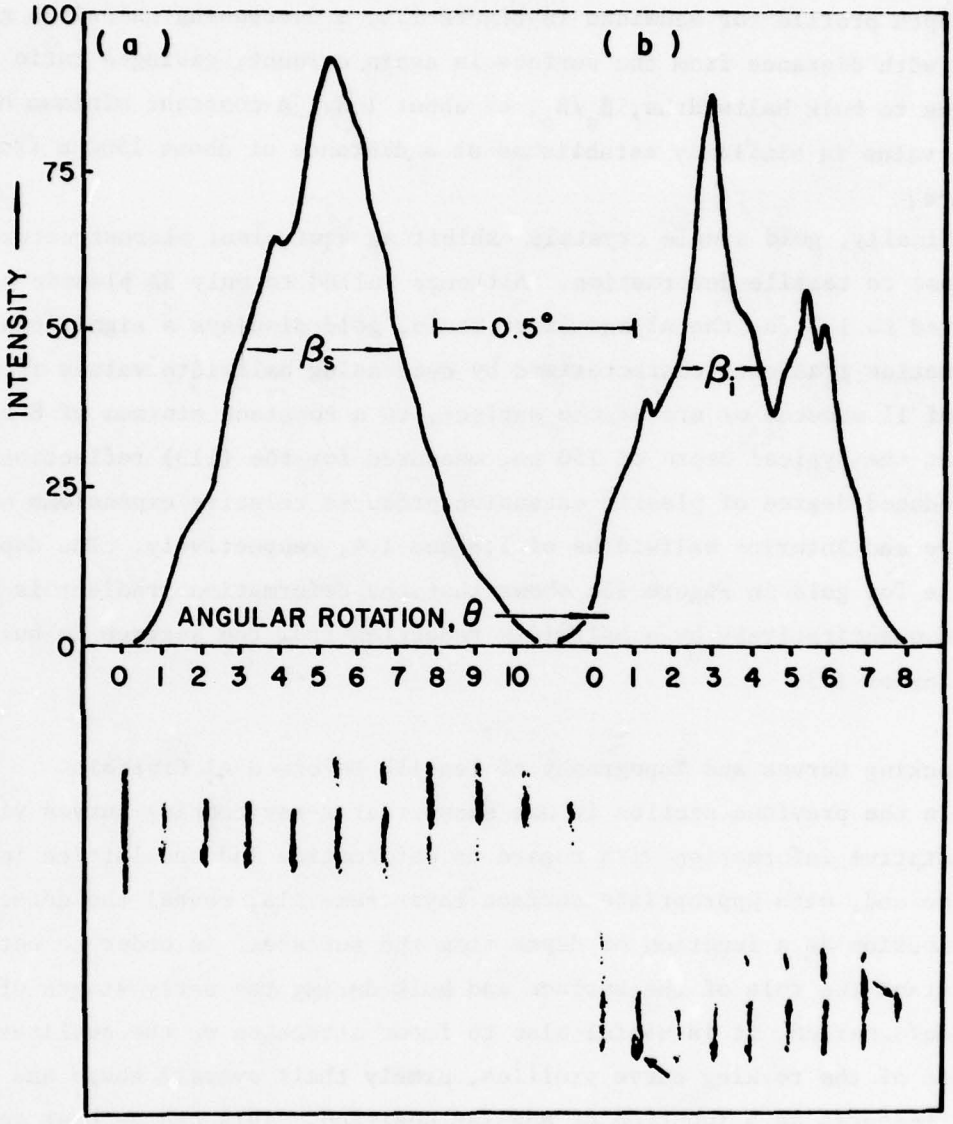


Figure 14. X-ray rocking curve profile correlated to topographic images at successive angular positions along the reflecting range for tensile deformed aluminum single crystal (ε_p = 10%, 0°C, tensile axis [100] reflection, CuKα_1 radiation): (a) original surface, and (b) after removal of a 100-μm surface layer.
Note: Topographs labeled "0" correspond to rotation through entire reflection.

6-minute-of-arc intervals during the crystal "rocking" procedure. As revealed by inspection of the enlarged sequence of images in Figure 14a, the deformed surface layer exhibits small, highly misaligned lattice domains, each of which reflects over a wide angular range. The former characteristic is a substructural feature indicative of deformation induced lattice breakup, often described as the evolution of a "debris" layer. The degree of tilt between dominant domains is represented by the angular separation of the intensity maxima of the multimodal rocking curves. The latter feature, or the persistence of reflection over rotation angles of 18 to 24 minutes of arc, is a measure of the internal strain produced in the small coherently reflecting lattice domains or "particles." Thus, the overlapping and poorly resolved component curves constituting the relatively smooth resultant profile are pictorially separated out, or "deconvoluted" by the topographic technique.

In contrast, the topographic features of the bulk regions suggest a closer resenblance to the substructural characteristics of an annealed or polygonized material. Reference to Figure 14b shows that the subdomains at 100 μm in depth are larger, more clearly resolved, and remain in reflec-reflecting position over a much narrower angular range. The domains indicated by arrows, for instance, exhibit reflection durations of only 6 to 12 minutes of arc. Hence, a well-defined rocking curve consisting of narrow, multiple peaks is generated for the interior region of the specimen.

3. Measurement and Characterization of Fatigue Damage in Al Crystals

The results presented in the previous section show that uniaxially deformed single crystals demonstrate a universal propensity toward preferential substructural breakup in the surface layer compared to the bulk material. After 10% plastic deformation, corresponding to a maximum applied stress of about 20 MPa, aluminum crystals with a [100] axis orientation typically display nearly a twofold decrease in halfwidth from the high surface values to a constant minimum value at approximately 100 to 150 μm into depth. The subsequent investigation involves the extension of the x-ray diffraction analysis to fatigue cycled crystals. For tension-compression fatigue with constant stress amplitude and zero mean

stress, a simple tension test represents the first half-cycle of the alternating sequence. This relationship, then, provides a basis upon which to compare the microstructural characteristics induced by monotonic deformation and the defect configurations produced on subsequent stress reversals.

Table 2 summarizes the results obtained by rocking curve measurements from the (100) reflection of cylindrical aluminum single crystals. The left half of Table 2 gives the halfwidths measured from the surface to the bulk after simple tension testing to a terminal stress of 17.2 MPa, corresponding to about 10% plastic strain. Inspection of the halfwidth values shows a typical decreasing gradient from a high, 14.3 minutes of arc, halfwidth value at the surface to a constant miminum halfwidth of 6.3 minutes at 150 to 200 μm in depth.

When identical specimens are subjected to cyclic stress reversals, even though carried out below the endurance limit at an amplitude of 1.03 MPa, dramatic differences in the defect distribution are evident. As recorded on the right half of Table 2 and shown in Figure 15, a decline in breadths can again be detected as the surface layers are incrementally removed to a distance of 100 μm from the surface. At this depth, however, contrary to the observations for simple extension, instead of continuing to descend toward a minimum value in the specimen core, the breadths for the fatigued crystal rise again to a plateau level in the bulk. This plateau region is established at a depth of about 200 μm, the same depth at which the tension curves level off at a constant minimum value, and extends throughout the specimen core. The most striking consequence of cycling at low stress is that the decreasing gradient from the surface to the bottom of the profile "well" in the subsurface region extending from 50 to 200 μm in depth results in a drop in breadth below the intrinsic halfwidth value of the virgin crystals. While the surface halfwidth after 2×10^5 cycles measured about 11 minutes of arc, the halfwidth at 100 μm depth is about 2 minutes of arc, considerably less than the inherent halfwidth of 5.7 minutes. Further, even after ascending to a plateau level at greater distances from the surface, the breadths in the crystal bulk do not exceed that of the undeformed crystal.

TABLE 2 - X-RAY ROCKING CURVE DATA AS A FUNCTION OF DEPTH FROM THE SURFACE FOR CYLINDRICAL ALUMINUM MONOCRYSTALS; [100] LOADING AXIS (100) REFLECTION

$N = 1/2$, $\sigma = +17.2$ MPa*		$N = 2 \times 10^5$, $\sigma = \pm 1.03$ MPa**	
Depth from Surface x (μm)	Average Measured Halfwidth β_m (min of Arc)	Depth from Surface x (μm)	Average Measured Halfwidth β_m (min of arc)
0	14.3	0	10.8
30	12.8	25	5.6
		50	3.9
		63	3.5
80	9.5	74	2.9
		90	2.1
		105	3.0
		122	3.5
130	7.8	135	3.3
		150	4.5
		165	4.4
200	6.3	210	4.6
		270	4.9
β_o (undeformed) = 5.4 min of arc		β_o (undeformed) = 5.7 min of arc	

*Simple tension.

**Tension-compression fatigue.

B. Al 2024 ALLOY STUDIES

1. Rocking Curve Analysis of the Surface Layer during Incremental Fatigue

In the previous sections, the results of x-ray diffraction studies of monotonically deformed and fatigue-cycled single crystals were described.

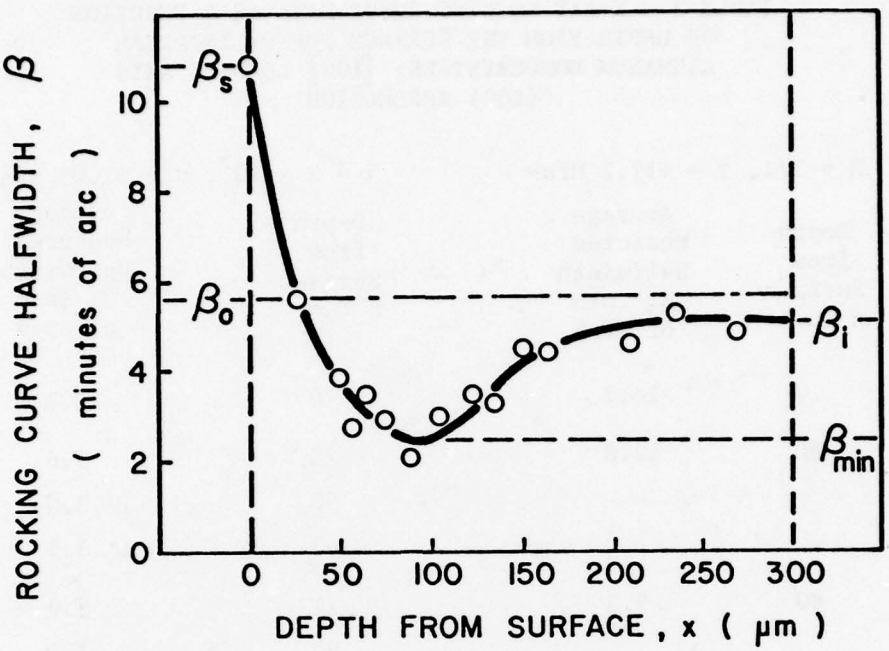


Figure 15. Halfwidth depth profile for an aluminum single crystal, fatigued in the high-cycle range, tension-compression mode ($\sigma_a = \pm 1.03$ MPa, 200,000 cycles, [100] axis orientation, (100) reflection)

Rocking curve analysis of the defect distribution and the microstructural characterization afforded by reflection topography could be successfully interpreted in terms of a preferential collection of imperfections in a surface "debris" layer, and to explain many mechanical properties of tensile and fatigue specimens. It was decided, therefore, to employ a similar x-ray technique to analyze the deformation characteristics of a polycrystalline metal. The first phase of the study of Al 2024-T3 was designed to measure the change in defect concentration in the surface layer as a function of the fraction of fatigue life. A special x-ray double-crystal diffractometer was used to generate pictorial rocking curves for the individual reflecting grains located at the specimen surfaces. As recorded in Table 3, the two Al 2024 batches used in the alloy investigation, having grain sizes of 44 and 33 μm in diameter, were found to have average halfwidths of 45.0 and 20.6 minutes of arc, respectively, after similar heat

TABLE 3 - COMPARISON OF SOME MORPHOLOGICAL, X-RAY DIFFRACTION, MONOTONIC, AND FATIGUE PROPERTIES OF THE TWO Al 2024 ALLOY STOCKS

Batch Designation	A	B
Grain Size (μm)	44	33
Undeformed Halfwidth, β_o (minutes of arc)	45.0	20.6
Proportional Limit, $\sigma_{p.l.}$	200 MPa 29 ksi	280 MPa 41 ksi
Cycles to Failure, N_f (at $\sigma_a = \pm\sigma_{p.l.}$)	21.1×10^3	7.5×10^3
Stress Amplitude $\sigma_a = (3/4)\sigma_{p.l.}$	150 MPa	210 MPa
Cycles to Failure, N_f	19.1×10^4	2.85×10^4
Stress Amplitude, $\sigma_a = (1/2)\sigma_{p.l.}$	100 MPa	140 MPa
Cycles to Failure, N_f	6.74×10^6	1.00×10^6

treatment and aging at ambient temperature. Also tabulated are the static and cyclic mechanical data pertinent to the study. Batch A (44-μm grain size) had a proportional limit for static tension of 200 MPa, compared to the predictably higher value for the smaller grain size batch B of 280 MPa. Fatigue cycling, at a stress amplitude equivalent to each stock's respective proportional limit, resulted in cycles to failure on the order of 21.1×10^3 for batch A and 7.5×10^3 for batch B. Figure 16 displays a typical S-N curve constructed for batch A, plotting the number of cycles to failure for tension-compression fatigue cycling with zero mean stress and stress amplitudes corresponding to 1.0, 0.75, and 0.50 of the proportional limit.

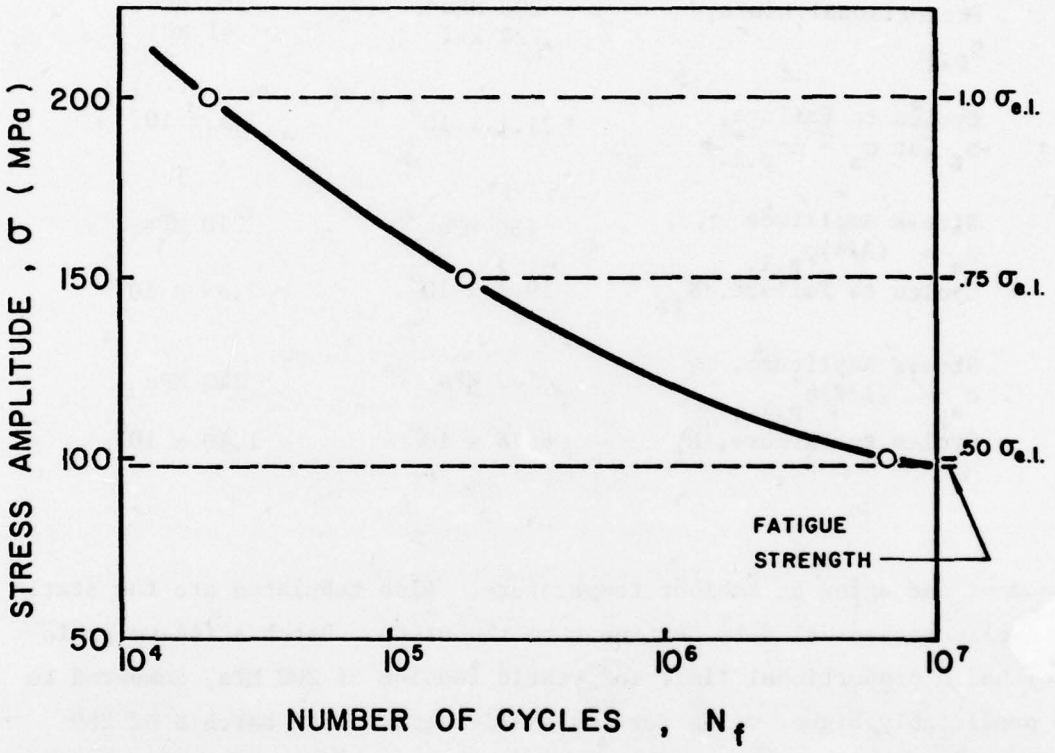


Figure 16. S-N curve for Al 2024, batch A, fatigued in the push-pull mode. Note: Each data point corresponds to average for at least three specimens.

As a preliminary evaluation of the effect of alternate stress cycling on the individual grain's reflection arrays, several specimens were cycled stepwise to failure at 200 MPa, with intermittent x-ray analysis of the surface grains. Figures 17 through 19 provide a basis for following the fatigue-induced substructural response. The grain reflections lying along selected Debye arcs for an undeformed cylindrical alloy specimen are presented in Figure 17. The film-recorded reflections are distinct and short in angular duration. The halfwidths, obtained by recording the intensity variation of successive spots as a function of their angular separation by microphotometry, are measured to be about 45 minutes of arc. After fatigue cycling to about 30% of the fatigue life, or 6300 cycles, the grain reflections become considerably more diffuse and persist over a greater angular range. The detail of reflections at this stage in the fatigue life, shown in Figure 18, displays the enhanced intensity and broad, 65 minutes of arc, halfwidths characteristic of the grains of a cycled alloy. After about 95% of the fatigue life, the striking grain reflection persistence is even more evident, as in Figure 19. At this last stage, the arrays appear broadened in both the horizontal and vertical, or azimuthal, directions, and breakup into a subgrain structure is indicated by the intensity fluctuations in these directions. The surface grain halfwidths expand on the average to over 75 minutes of arc. A substantial integrated intensity enhancement of the arrays is also associated with imminent failure, probably due to a reduction in secondary extinction caused by fragmentation into a surface debris. Reference to Figure 20 shows the complete Debye pattern from which the grain reflections in the former figure were chosen. As previously discussed in the Experimental section, statistical analysis of the grain reflection breadths permits a quantitative evaluation of the microstructural response during incremental fatigue cycling. Table 4 summarizes the surface rocking curve data collected for batch A specimens for stepwise fatigue employing various stress amplitudes. Figure 21 presents the same data plotted against the actual number of fatigue cycles to which the percentages of life correspond. Inspection of the curves for stress amplitudes equivalent to 0.5, 0.75, and 1.0 $\sigma_{p.l.}$ leads to the formulation of a general behavioral pattern. First, the lower the stress amplitude, the greater is the number

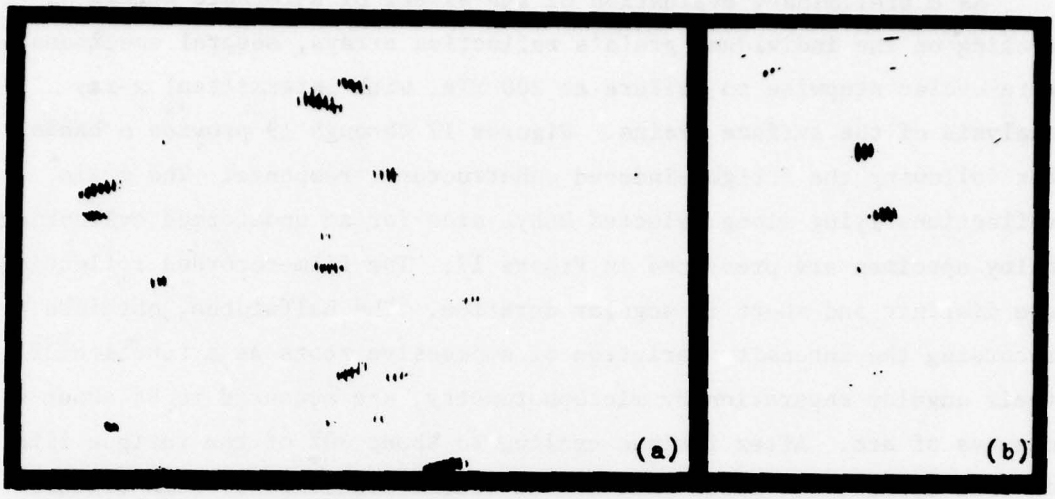


Figure 17. Detail of the grain reflections for Al 2024 prior to fatigue (CuKα monochromated radiation, angular specimen settings 5 minutes of arc): (a) (200), (311), and (222) reflections; and (b) (331) and (410) reflections.

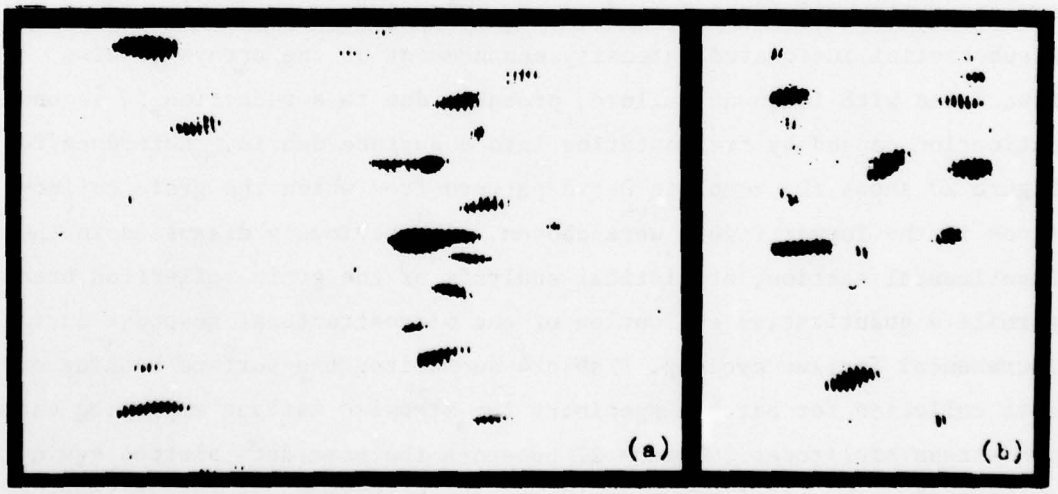


Figure 18. Detail of the grain reflections of Al 2024 cycled to 30.4% of the fatigue life with a stress amplitude of ±200 MPa: (a) (200), (311), and (222) reflections; and (b) (331) and (410) reflections.

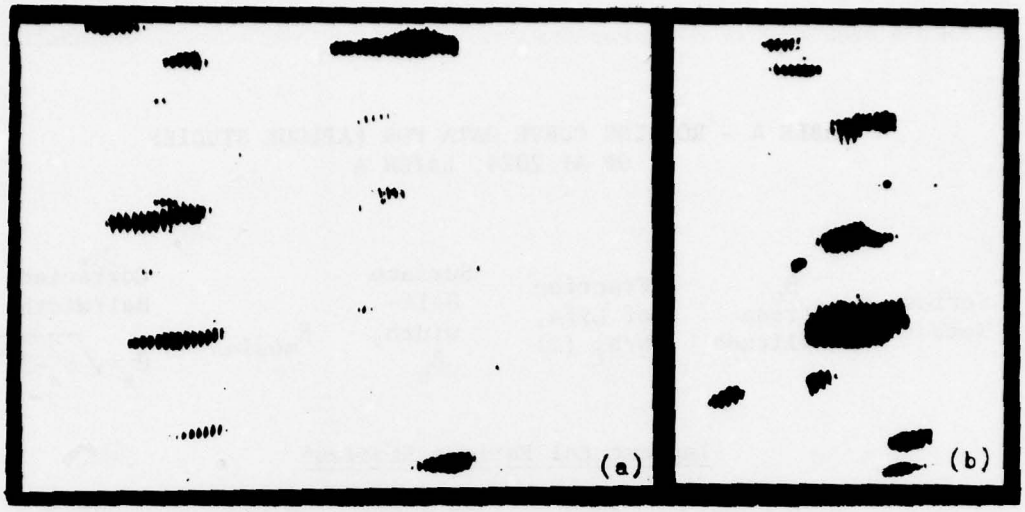


Figure 19. Detail of the grain reflections of Al 2024 cycled to 95.7% of the fatigue life with a stress amplitude of ±200 MPa: (a) (200), (311), and (222) reflections; and (b) (331) and (420) reflections.

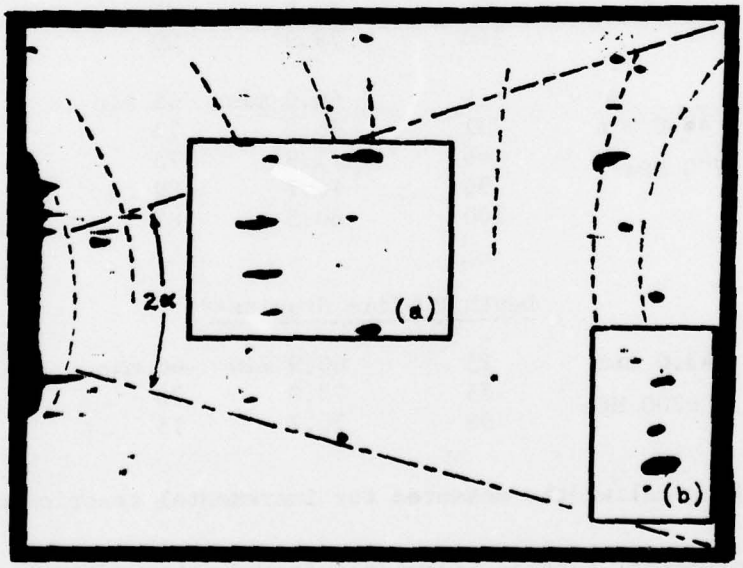


Figure 20. Debye pattern for fatigue cycled Al 2024 alloy showing azimuthal limits for grain reflection analysis. Note: Regions (a) and (b) correspond to enlarged arrays in Figure 19.

TABLE 4 - ROCKING CURVE DATA FOR FATIGUE STUDIES OF Al 2024, BATCH A

Series Number	β_o Stress Amplitude	Fraction of Life, N/N_f (%)	Surface Halfwidth, β_s	β_{median}	Corrected Halfwidth, $\bar{\beta}_s = \sqrt{\beta_s^2 - \beta_o^2}$
		Incremental Fatigue Studies*			
10	43.0 min	22	55.6 min	50 min	35.2
		44	57.1	55	37.6
$\sigma_a = \pm 100$ MPa		66	62.5	65	45.4
		88	66.2	65	50.3
		100	77.5	75	64.5
		9.5	60.4 min	57.5 min	38.3
		19	65.4	65	45.8
20 and 30	46.7 min	28	66.3	65	47.1
		47	68.7	70	50.4
$\sigma_a = \pm 150$ MPa		94	71.5	75	54.1
		100	79.9	80	64.8
		19	60.0 min	65 min	39.7
40	45.0 min	31	66.2	70	48.6
		66	71.9	75	56.1
$\sigma_a = \pm 200$ MPa		96	76.7	80	62.1
		100	80.5	85	66.7
		Depth Profile Studies**			
70	45.0 min	25	60.9 min	60 min	41.0
50		75	73.0	70	57.5
80	$\sigma_a = \pm 200$ MPa	95	76.7	75	62.1

*Surface halfwidths measured for incremental fraction of the life.

**Supplemental surface halfwidths from depth profile investigation.

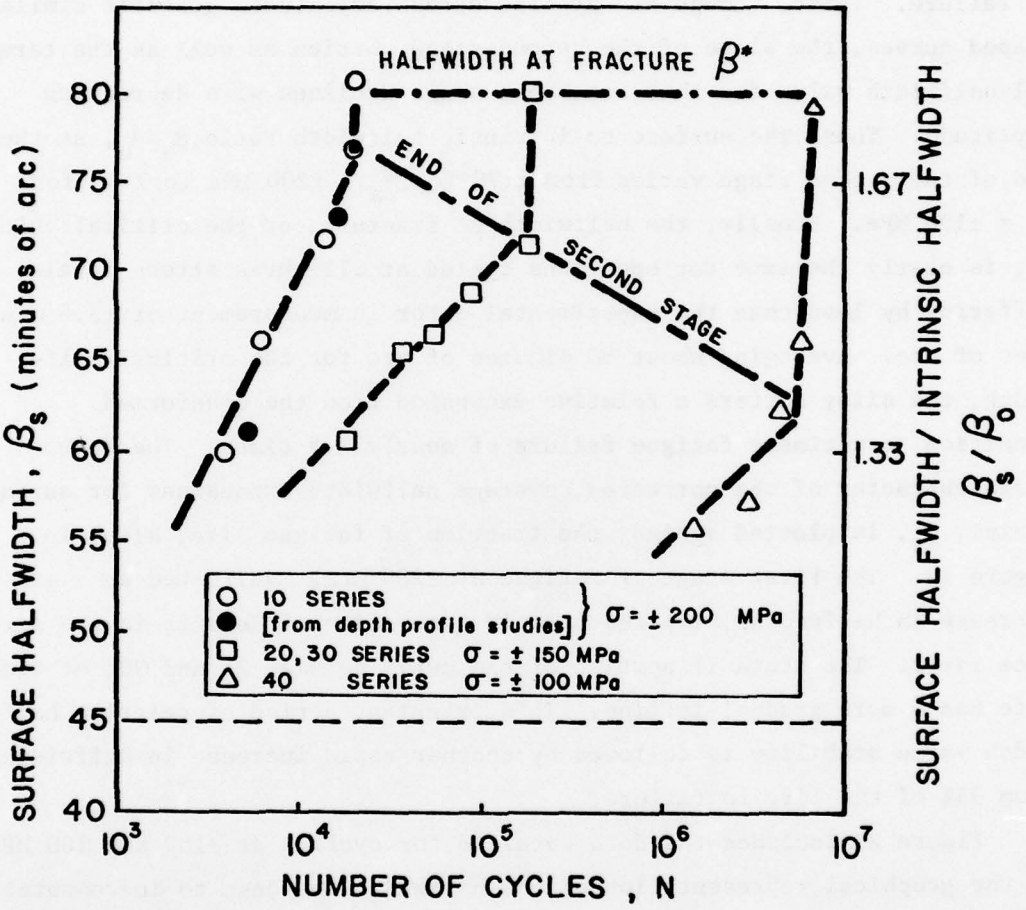


Figure 21. Change in the surface halfwidths with progressive fatigue cycling of Al 2024 alloy, batch A.

of cycles required to generate any given degree of halfwidth expansion; for the stress levels employed in this study, the curves are shifted relative to one another by about an order of magnitude. Second, the progressive fatigue curves suggest a three-stage response to the cycling process: an initial period of rapid expansion of absolute halfwidths, an intermediate stage of more gradual increase, and a final stage of rapid increase prior to failure. Third, though all applied stress amplitudes generate similarly shaped curves, the slope of the second-stage portion as well as the terminal halfwidth value for this transient stage declines with decreasing amplitude. Thus, the surface to intrinsic halfwidth ratio, β_s/β_o, at the end of the second stage varies from 1.70 for $\sigma_a = \pm 200$ MPa to 1.40 for $\sigma_a = \pm 100$ MPa. Finally, the halfwidth at fracture, or the critical value, β^*, is nearly the same for specimens cycled at all three stress levels, differing by less than the experimental error in measurement of ±3.6 minutes of arc. Averaging about 80 minutes of arc for the critical halfwidth, the alloy suffers a relative expansion from the undeformed condition to ultimate fatigue failure of nearly 1.8 times. The three-stage character of the corrected, average halfwidth expansions for surface grains, $\overline{\beta}_s$, is plotted against the fraction of fatigue life, N/N_f, in Figure 22. The first stage of fatigue at ±200 MPa, manifested by a steep increase in halfwidths, implies a rapid generation of defects in the surface layer. The stage II portion of the curve between 25 and 90% of the life has a more gradual incline. This transient period of relative halfwidth value stability is followed by another rapid increase in halfwidths from 95% of the life to failure.

Figure 23 includes the data obtained for cycling at ±150 and 100 MPa in the graphical representation of the halfwidth response to incremental fatigue. It is immediately evident that the halfwidth expansions under these lower stress amplitudes are similar to that obtained for the initial stress level. All the curves fall within experimental error bands of ±3.6 minutes of arc. This indicates that the surface defect concentration introduced by cycling to any fraction of the fatigue life is virtually independent of the stress amplitude employed. The slopes for stages I, II, and III are about 1.86, 0.23, and 1.40, respectively.

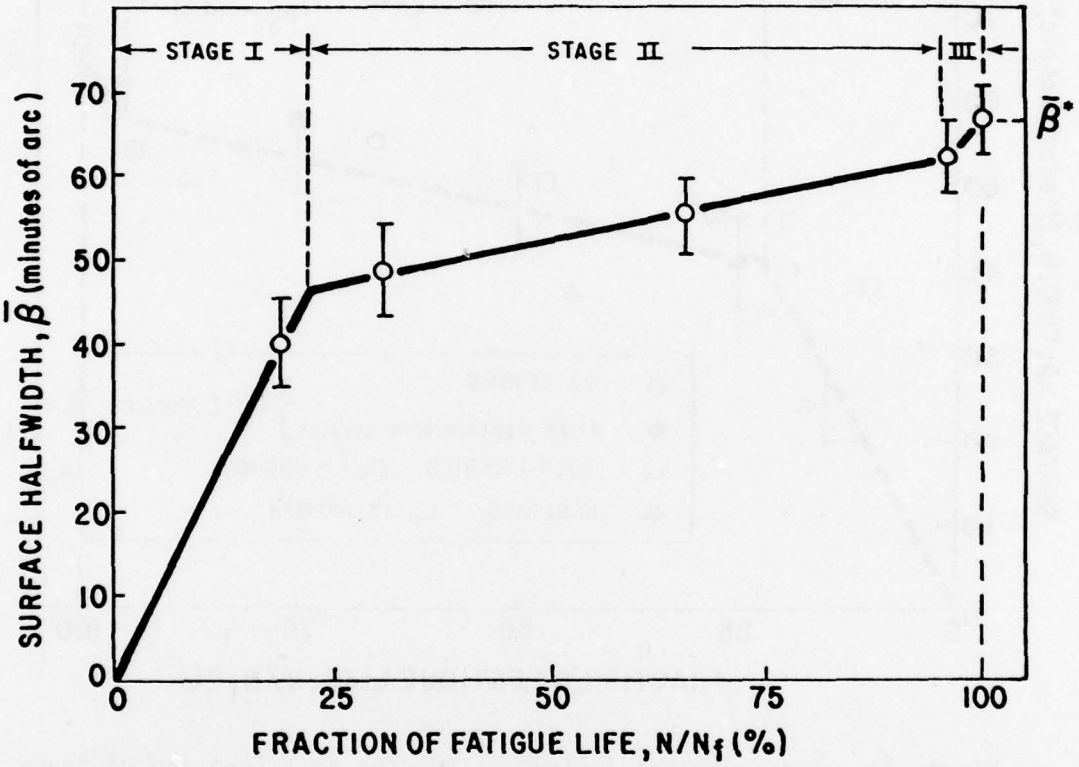


Figure 22. Surface halfwidths as a function of the fatigue life for Al 2024, batch A, cycled at ±200 MPa.

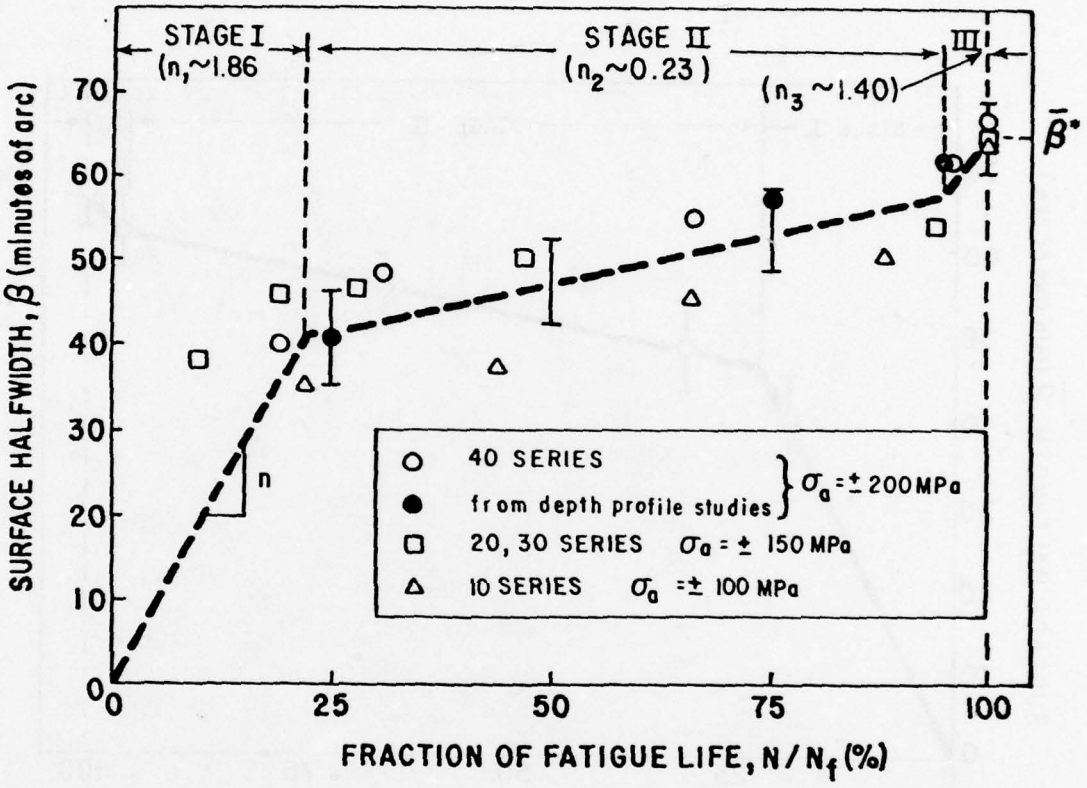


Figure 23. Change in the surface halfwidths as a function of fraction of the fatigue life for A1 2024, batch A, cycled at stress amplitudes corresponding to 1.0, 0.75, and 0.50 $\sigma_{p.l.}$. Note: Error bars represent the average, 3.6 minutes of arc, deviation in measured halfwidths for the grain population contributing to each experimental data point.

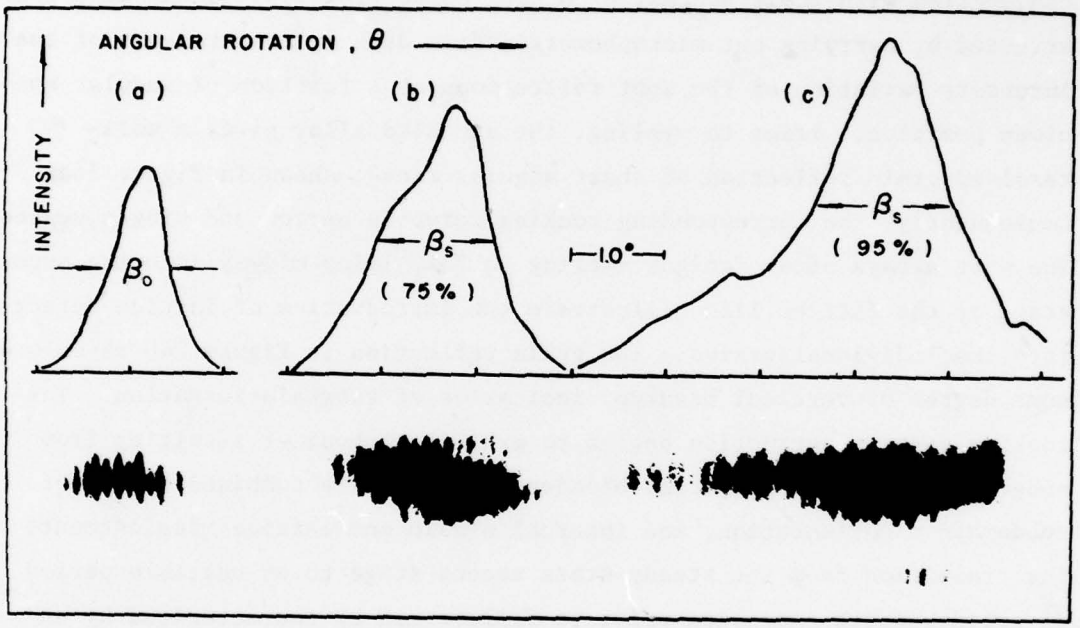


Figure 24. Schematic rocking curves (above) for actual grain reflection arrays (below) recorded during controlled rotation of Al 2024 alloy specimens [Intensity profiles constructed from microphotometric scan of each spot array; sample reflections taken from (222) Debye arcs]: (a) undeformed, annealed, and polished; (b) fatigue cycled to $N/N_f = 0.75$, and (c) cycled to $N/N_f = 0.95$.

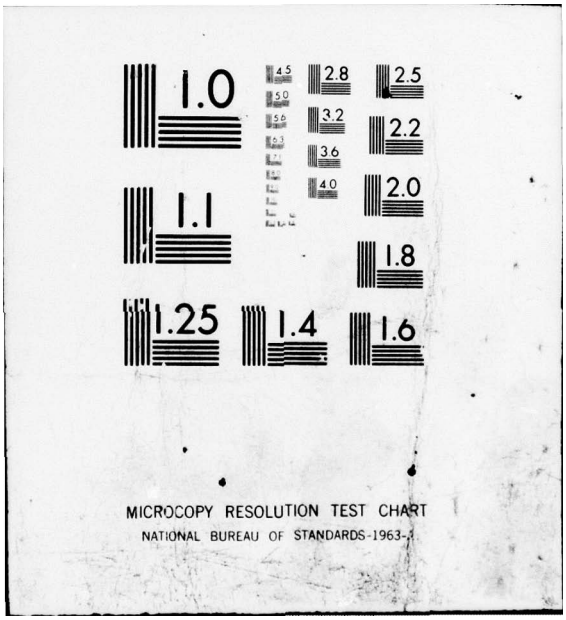
AD-A079 538 RUTGERS - THE STATE UNIV PISCATAWAY NJ COLL OF ENGIN--ETC F/G 11/6
DETERMINATION OF PREFRACTURE FATIGUE DAMAGE.(U)
JAN 80 R PANGBORN, S WEISSMANN, I R KRAMER N00600-77-C-1134
DTNSRDC-80/006 NL

UNCLASSIFIED

2 OF 2
AD
A079538



END


1.0
1.1
1.25
1.4
1.6
1.8
2.0
2.2
2.5
2.8
3.2
3.6
4.0
4.5
5.0
5.6
6.3
MICROCOPY RESOLUTION TEST CHART
NATIONAL BUREAU OF STANDARDS-1963-A

2. Elucidation of the Fatigue-Induced Surface Morphology

In orde to further differentiate the three stages comprising the surface layer response to fatigue cycling, the topographic features displayed by the grain reflections can be correlated to the morphological changes at the surface during the fatigue life. Analogous to the single-crystal study, Figure 24 presents photographic enlargements of typical grain reflections obtained for 0, 75, and 95% of the fatigue life, in conjunction with their schematic rocking curve profiles. These were constructed by carrying out microphometric film density measurements of the intensity variation of the spot reflections as a function of angular specimen position. Prior to cycling, the annealed alloy gives a well-resolved grain reflection of short angular range, shown in Figure 24a. Consequently, the corresponding rocking curve is narrow and single peaked. The spot arrays after fatigue cycling to 75%, lying midway into the second stage of the fatigue life, illustrate the introduction of lattice defects into the individual grains. The grain reflection in Figure 24b reveals some degree of vertical breakup, indicative of subgrain formation. The rocking curve construction begins to exhibit a shoulder resulting from subgrain tilt, and an overall broadening due to the combined effect of subdomain misorientation, and internal strain and lattice misalignment. The transition from the steady-state second stage to an unstable period of rapid breadth expansion prior to failure can be characterized by an escalation of the grain fragmentation by intense multiplication and interaction of lattice defects. The intensity oscillation along the angular reflecting range becomes more pronounced. The spot reflections shown in Figure 24c become increasingly diffuse and larger in number, generating a broad, multipeaked rocking curve profile.

The morphological examination of the surface afforded by light and scanning electron microscopy displays transitional stages consistent with those identified by x-ray analysis. As shown in the SEM photomicrograph, Figure 25, several specimens were especially prepared with spark-erosion planed flat regions along the gage length prior to final electropolishing and cycling to 25, 75, and 95% of the fatigue life. The specimens cycled to 25%, representing the end of stage I, exhibited

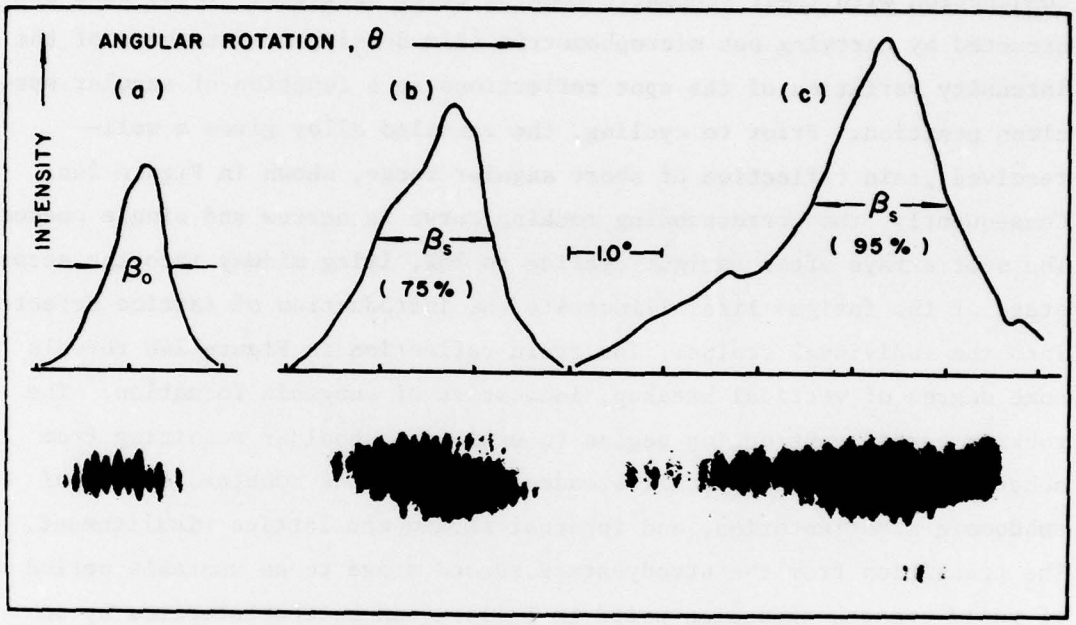


Figure 24. Schematic rocking curves (above) for actual grain reflection arrays (below) recorded during controlled rotation of Al 2024 alloy specimens [Intensity profiles constructed from microphotometric scan of each spot array; sample reflections taken from (222) Debye arcs]: (a) undeformed, annealed, and polished; (b) fatigue cycled to $N/N_f = 0.75$, and (c) cycled to $N/N_f = 0.95$.



Figure 25. Scanning electron micrograph of the flat gage region especially prepared by spark-erosion planing, prior to electropolishing and testing of the specimen. (10X)

no evidence of structural change at the surface. After cycling well into stage II to 75%, however, there emerges some evidence of cyclically induced slip. While the 400X light micrograph of the unetched specimens at 75% (Figure 26a) reveals little or no slip markings, fine slip traces are perceptible for etched specimens at 200X (Figure 27a and 27b) and at 400X (Figure 28a). In contrast, after cycling to 95%, representing the onset of stage III, intersecting bands of densely packed slip traces are found traversing the specimen surface along the entire gage length, as shown in the optical micrographs of etched specimens (Figures 27c, 27d, and 28b). In some localized regions of the gage length, these bands group into packets, producing striation-like features encircling the specimen gage section, shown in the SEM photographs (Figure 29). Reference to the light micrograph for an unetched specimen cycled to 95% (Figure 26b) gives witness to an apparent generation of deep grooves, or persistent slip bands at the surface, also shown in the high-magnification SEM

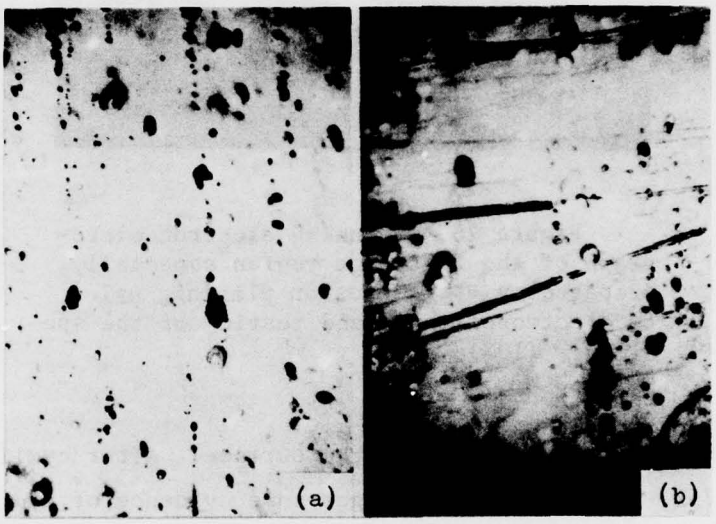


Figure 26. Light micrographs of unetched Al 2024 specimens cycled at ±200 MPa to stages II and III of the fatigue life (400X): (a) 0.75 N/N_f, and (b) 0.95 N/N_f.

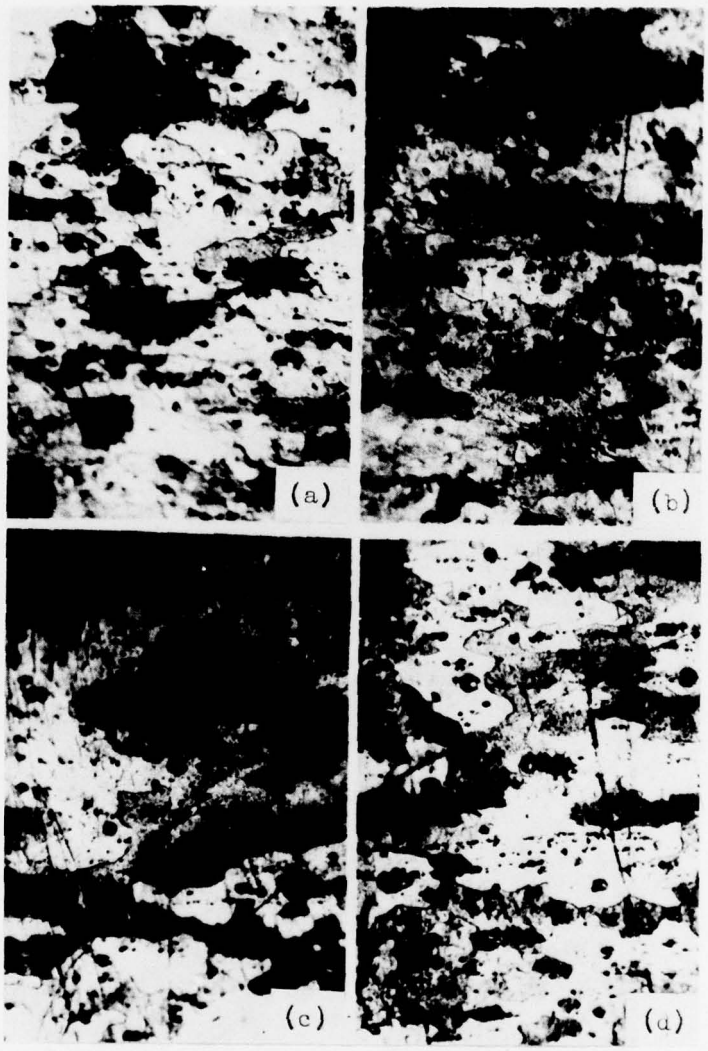


Figure 27. Optical micrographs of etched Al 2024 specimens showing the comparative degrees of slip activity in stages II and III of the life (200X): (a) and (b) 0.75 N/N_f, and (c) and (d) 0.95 N/N_f.

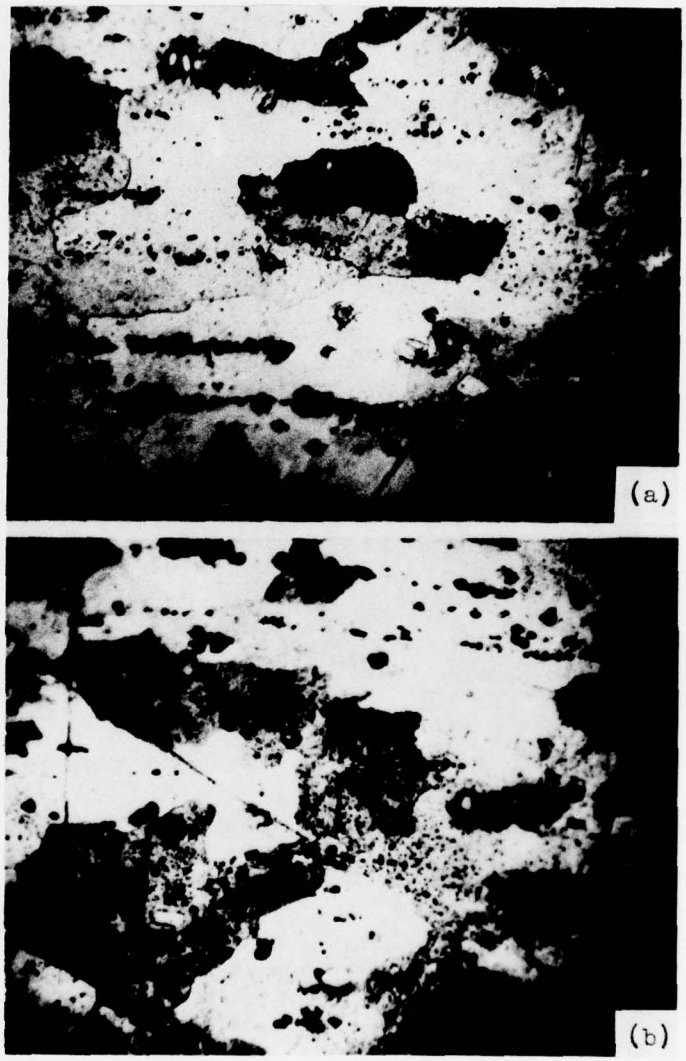


Figure 28. Optical micrographs of etched Al 2024 specimens showing intragranular and transgranular slip traces induced by fatigue cycling (400X): (a) 0.75 N/N_f, and (b) 0.95 N/N_f.

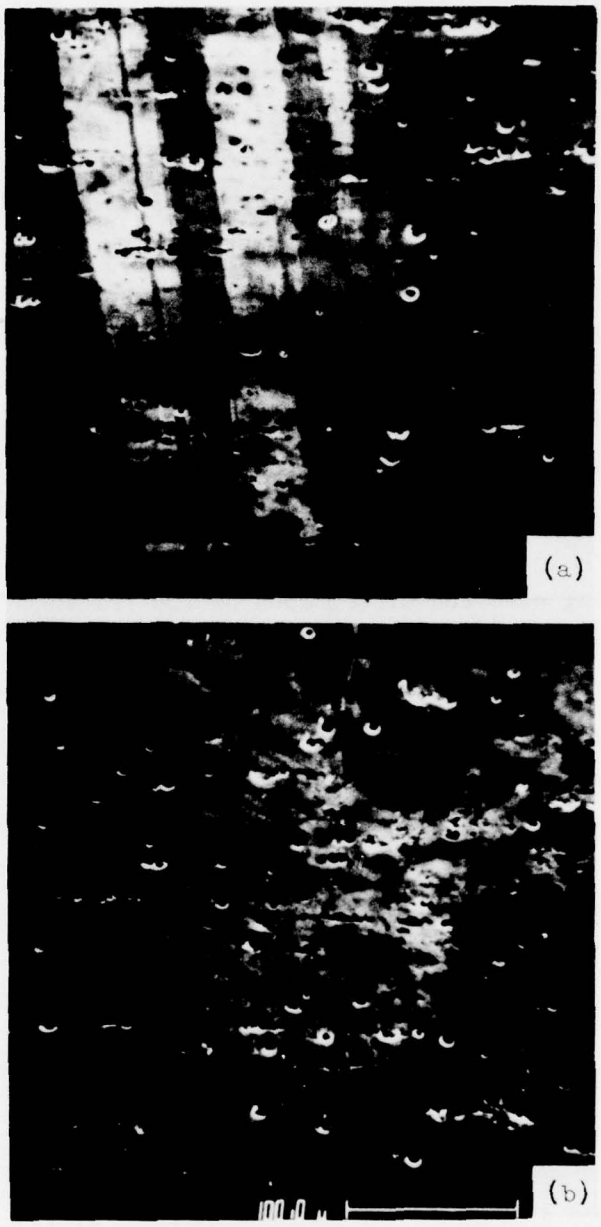


Figure 29. SEM photomicrograph of an Al 2024 specimen cycled to 95% of the fatigue life at ±200 MPa (250X): (a) striations encircling the gage section comprising packets of slip bands, and (b) intersecting bands of densely packed slip traces.

photomicrograph (Figure 30). They eventually assume either an intrusion or extrusion character, as exhibited by the extruded ridge in Figure 31a. Incipient fatigue cracks are nucleated at the PSB's or small etch pits left as a by-product of electropolishing, as shown in Figure 31b. The observation of very fine slip bands for Al 2024 after fatiguing to 75% of the life (Figures 27a and 27b) indicates that they may be removed without any appreciable increase in N_f. In fact, it was found that no slip traces or PSB's could be detected after removal by electropolishing of a surface layer of only 25-μm thickness from specimens cycled 75 or 95% of their lives. Although specimens fatigued to 95% of their lives no doubt contain small cracks (Figure 26b), attempts to identify the existence of perceptible fatigue cracks at 95% of the life by exposure to radioactive Krypton (KET Inspection, performed by Qual-X, Incorporated, Hilliard, Ohio) were unsuccessful.

The scanning electron micrographs of the fracture surface shown in Figures 32 and 33 illustrate the adherence to a typical fatigue failure mode. After fracture is initiated, the sheared surfaces are smoothed by cyclic rubbing, or friction (Figure 33a). At higher magnification (Figure 33b) the resolution of finer topography reveals striations due to crack arrest after the tensile portion of each cycle. Final failure occurs by a ductile rupture mode when the circumferential cracks reduce the effective cross-sectional area sufficiently to produce catastrophic fracture. Small, micron-size dimples are also prevalent on the fracture surface where inclusions may have been ripped free.

3. Response of the Surface and Bulk to Fatigue Cycling

A comprehensive evaluation of the fatigue response in polycrystalline materials should also include x-ray analysis as a function of distance into the specimen interior. In a manner similar to that employed in the single-crystal studies, an incremental polishing technique was used to generate representative depth profiles for the Al 2024 specimens at various fractions of the life. The variation of individual grain halfwidths with the distance from the specimen surface was found to be remarkably similar to the profile exhibited by a fatigued monocrystal.



Figure 30. SEM image of high-relief slip band structure at 0.95 N/N_f. (2000X)

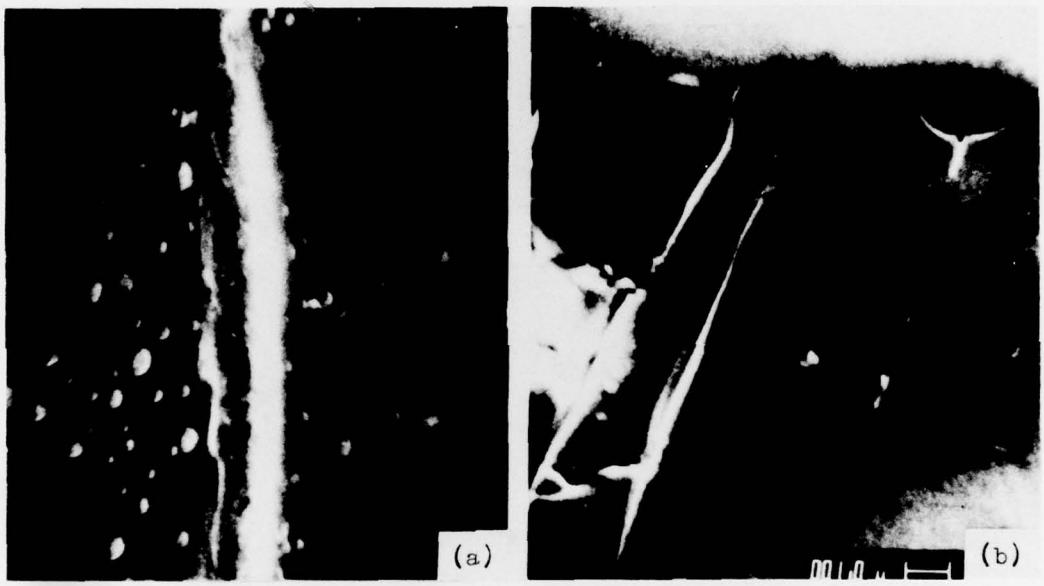


Figure 31. High-magnification SEM photomicrographs of an Al 2024 specimen cycled to 95% of the fatigue life at ±200 MPa, unetched (6000X): (a) extruded ridge from a slip band on the specimen surface; and (b) microcracks nearly normal to the specimen axis, initiated within PSB's and small residual pits from the surface electropolishing.



Figure 32. SEM image of the fracture surface for an Al 2024 fatigue specimen cycled at ±200 MPa (30X)

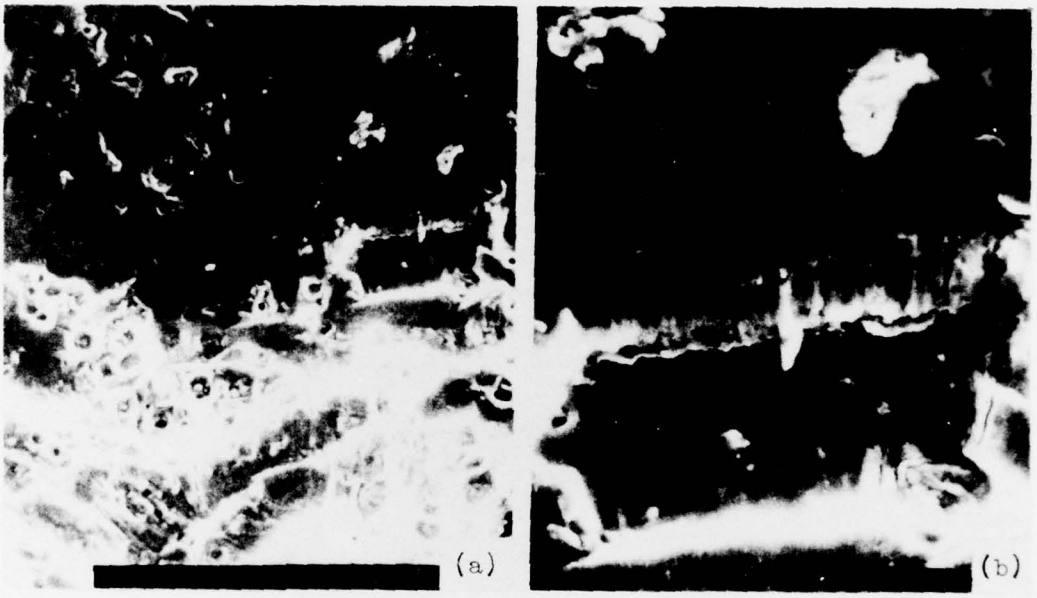


Figure 33. Detail of the fracture surface by SEM photomicroscopy: (a) inclined shear failure region, smoothed by cyclic friction, and ductile rupture in a plane normal to the specimen axis (foreground) (300X); and (b) striations due to fracture arrest after the tensile half-cycles (1000X).

The series of x-ray patterns presented in Figures 34 through 36 were obtained in the preliminary in-depth study. The first pattern, Figure 34, shows the actual grain reflections of the alloy specimens prior to fatigue. The Debye pattern in Figure 34a and the enlarged images of representative grains P in Figure 34b reveal the narrow reflection range expected for the undeformed condition. After fatigue to only 0.15% of the total life at ±100 MPa, or 0.5 $\sigma_{p.l.}$, the resultant breakup of the grains into a highly fragmented subgrain structure is immediately evident in Figure 35. The grains Q, in particular, both display two or more dominant subgrains misoriented with respect to the vertical direction, given by the apparent azimuthal spread or broadening, and in the horizontal direction as given by the relative shift in the multimodal arrays' peak displacements. The overall reflection duration is substantially enhanced as a result of the induced misalignment and internal strain associated with the individual subdomains or particles contributing to the spot arrays. The average halfwidth obtained by microphotometric traversal is about 55 minutes of arc. After removal of a 100-μm surface layer, x-ray analysis discloses a bulk substructure due to fatigue that obviously differs markedly from that produced at the surface. The spot arrays are found to be much narrower in width, measuring about 45 minutes of arc, or nearly the value for undeformed specimens. The substructure, typified by the grains R in Figure 36 reflects a sharp-peaked polygonized configuration. Further layer removals increase the resolution of the relatively unstrained but mutually misoriented reflecting domains constituting the grains in the specimen bulk material.

Table 5 summarizes the quantitative data for this preliminary investigation, in addition to the results of depth profile analysis for cycling at ±200 MPa, or 1.0 $\sigma_{p.l.}$, to 25, 75, and 95% of the total fatigue life. Figure 37 presents a graphical construction of the actual depth profiles. The curve showing the dependence of the average, corrected halfwidths, $\overline{\beta}$, with distance from the surface for 0.15% of the life approximates the shape previously identified for profiles from tensile deformed monocrystals. For this early stage in the cycling sequence, the depth effect is characterized by a simple decreasing halfwidth gradient, with a reduction in

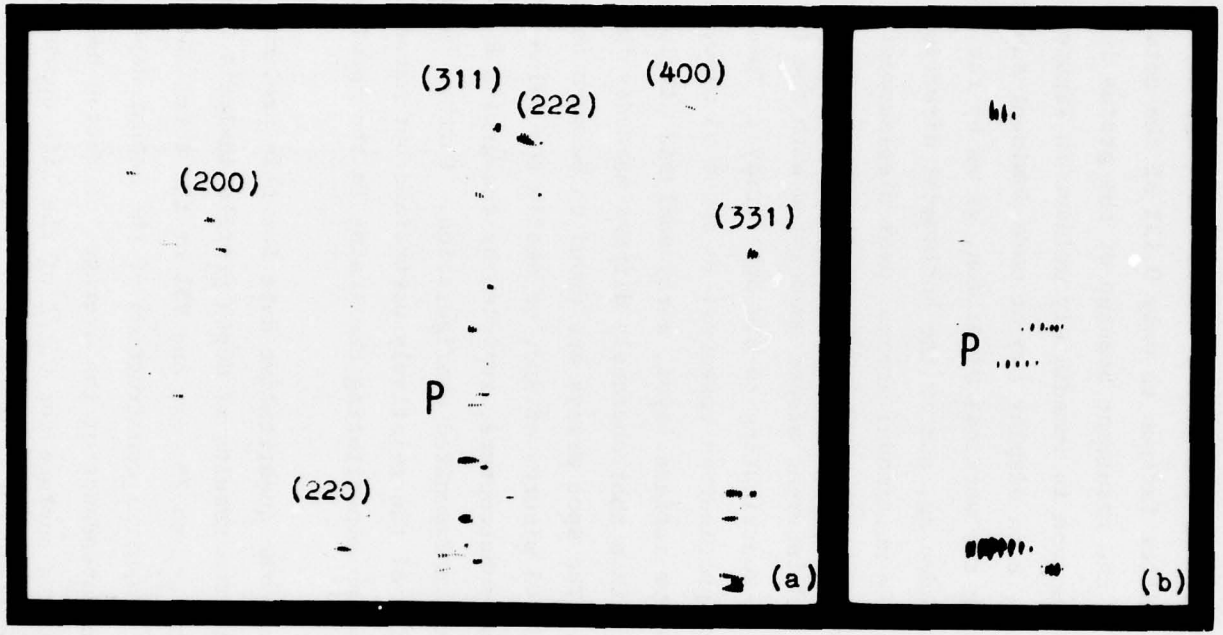


Figure 34. Debye pattern spot arrays exhibiting the reflection range of Al 2024 grains prior to cycling (CuKα monochromated radiation; angular specimen settings 5 minutes of arc): (a) survey of grain reflections, and (b) detail of spot array for grain P.

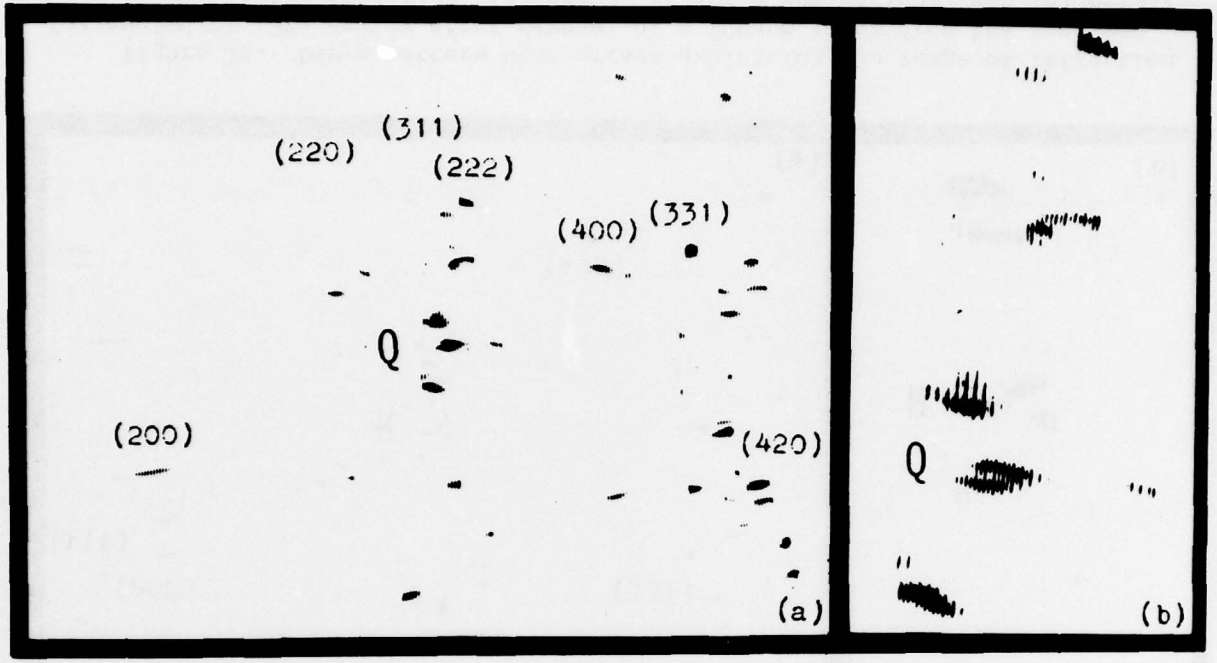


Figure 35. Debye pattern spot arrays exhibiting the reflection range of grains located at the surface of cycled Al 2024 specimens (σ_a = ±100 MPa, N = 10^4): (a) survey of grain reflections, and (b) detail of spot array for grain Q.

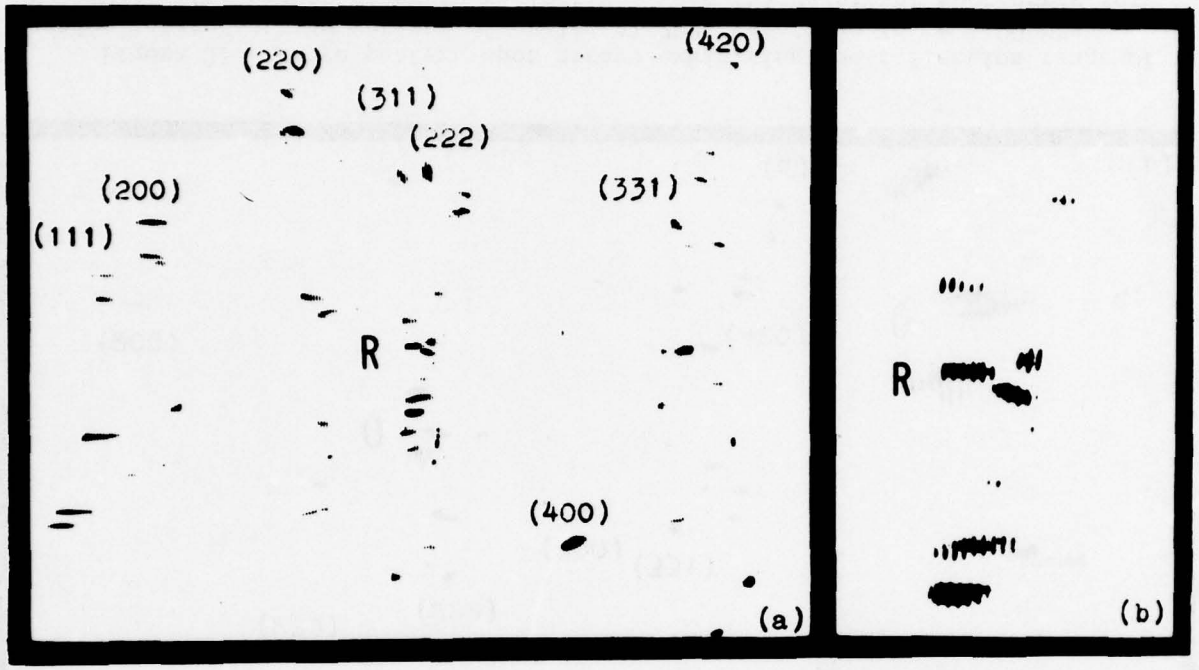


Figure 36. Debye pattern spot arrays exhibiting the range of reflection for cycled Al 2024 grains after removal of a 100-μm layer from the specimen surface by electropolishing: (a) survey of grain reflections, and (b) detail of spot array for grain R.

TABLE 5 - X-RAY ROCKING CURVE DATA FOR DEPTH PROFILE AND RECYCLING STUDIES OF A1 2024, BATCH A

Series Number	N/N_f (%)	σ_a (MPa)	Depth, x (μm) or N/N_f(%)	Measured Half-width, β_x	β_{median}	Corrected Halfwidth, $\overline{\beta}(\beta_o$ = 45.0 min)
1	0.15	100	0 (surface)	53.0 min	55 min	28.0
			100 μm	47.0	45	13.6
			200	46.0	45	9.5
70	25	200	0 (surface)	60.9 min	60 min	41.0
			50 μm	50.2	50	22.2
			150	50.0	50	21.8
			250	52.0	55	26.1
			400	50.5	55	22.9
50	75	200	0 (surface)	73.0 min	70 min	57.5
			50 μm	57.0	55	35.0
			125	55.0	50	31.6
			250	64.5	60	46.2
			400	62.6	60	43.5
	Recycling		0.1%	54.3 min	50	30.4
			1.0	48.2	45	17.3
			3.0	52.0	50	26.1
			5.0	54.2	55	30.2
	Second Depth Profile		0 (new surf.)			
			50 μm	50.2 min	50 min	22.2
			125	48.0	45	16.7
			250	48.5	50	18.1
			400	48.7	50	18.6
			1500 (spec. center)	49.0	50	19.4
80	95	200	0 (surface)	76.7 min	75	62.1
			50 μm	64.8	60	46.6
			100	58.2	55	36.9
			175	65.2	67.5	47.2
			250	69.7	70	53.2
			400	68.1	67.5	51.1
	Recycling		1/2 cycle	69.2 min	70 min	52.6
			0.1%	66.2	65	48.6
			1.0	61.8	60	42.4
			2.0	60.0	60	39.7
			3.0	60.2	60	40.0
			5.0*	64.7	65	46.5

*Followed by cycling to failure at $N = 16.9 \times 10^3$ ~ 80% of normal life.

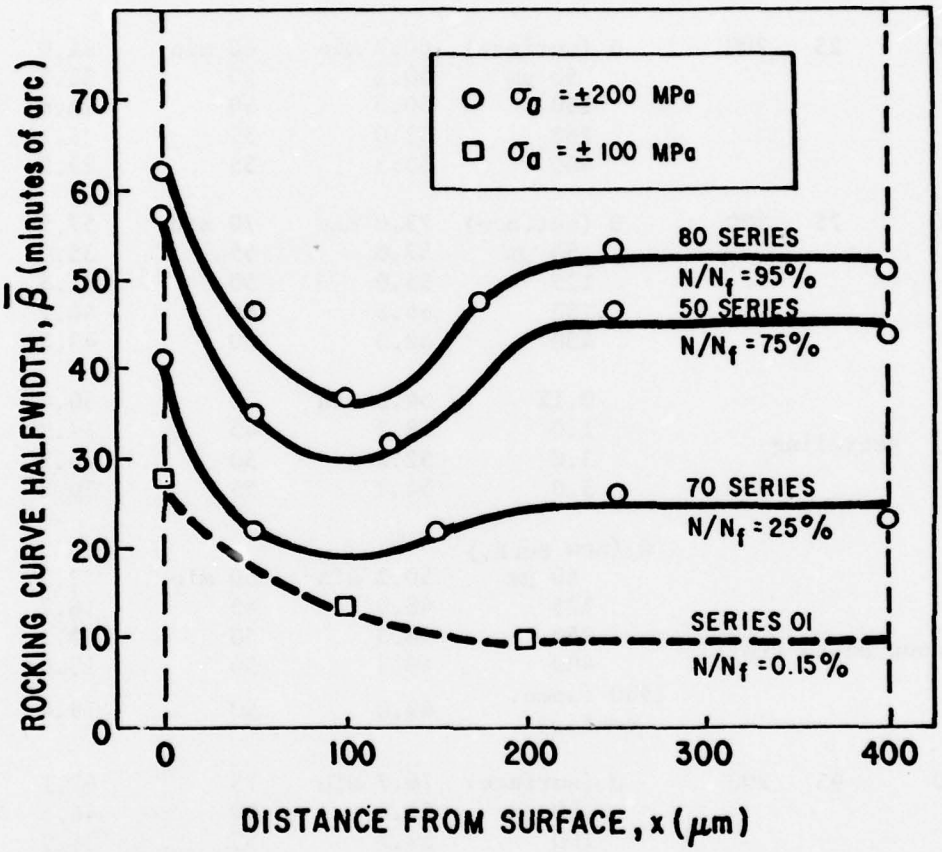


Figure 37. Depth profiles ($\bar{\beta}$ vs depth, x) for various fractions of the total fatigue life of Al 2024 specimens.

corrected breadth value by about a factor of 2.8 from the immediate surface to the bulk, where the halfwidth becomes constant at about 200 μm in depth.

After 5% of the life, the halfwidths over the entire cross section of the specimen are visibly enhanced. However, a shallow well or minimum begins to be perceptible in the sublayer centered at about 100 μm in depth, analogous to the behavior previously observed for the fatigued single crystal in Figure 15. Specimens cycled to still greater fractions of the fatigue life derive both greater halfwidth expansions at all depths and a more pronounced halfwidth well in the subsurface region. It is also evident from Figure 37 that the surface and bulk regions experience significantly different rates of halfwidth expansion during various stages in the fatigue process. The change in the surface halfwidths after 25% represents over half the total change incurred during the entire life, while the bulk values at this stage show a fractional change more nearly equivalent to the actual extent of cycling. At 75%, the surface halfwidths already show signs of saturation, but the bulk values again reveal a consistency with the fraction of life actually expended. Thus, the rapid substructural response inherent particularly to the stage I of surface halfwidth expansion is accompanied by a much more consistent incremental change in the bulk for each fatigue interval, giving a steady increase in measurable "damage" to the bulk throughout the fatigue life.

Also in strict adherence to the behavior observed for single-crystal fatigue is the leveling off of the profiles at a plateau level at 200 μm in depth. For cycling to very low percentages of the fatigue life, the monotonic decline in halfwidths terminates at a constant value at this distance from the surface, which is retained as a transitional region throughout the life during the gradual elevation of the plateau level.

4. Effects of Fatigue Cycling in the Absence of the Surface Layer

The depth profile analysis of cycled alloy specimens provided ample evidence of bulk microstructural changes, especially prevalent at the later stages of the fatigue life. As a consequence of these observations, an effort was made to evaluate the stability of the defect structure

induced in the bulk by removing the surface layer and recycling. In order to insure complete elimination of the surface "debris" layer, the specimens were electropolished to a 400-μm depth. The specimens then featured a uniform halfwidth value over the cross section equal to the bulk plateau value induced by the prior fatigue. Recycling was carried out at the same load amplitude as maintained for the prefatiguing.

Inspection of Figure 38 indicates that, for specimens cycled to 95 and 75% of the average fatigue life, surface removal and recycling causes a dramatic decline in the corrected halfwidth values at the new surface. The halfwidths dip steeply toward the virgin specimen curve width, the 75% specimen exhibiting a faster and stronger recovery phenomenon. For 75% prior fatigue, the halfwidths are reduced by about two-thirds after only 300 cycles, or 1.5% of the normal fatigue life at ±200 MPa. For specimens precycled 95%, the reduction in breadths proceeds more sluggishly to a minimum after 400 cycles, or 2% of the total life. A weaker halfwidth decline by about one-fifth is attained, since by this late stage in the life the specimen surely contains cracks. After passing through a minimum, the halfwidths increase again at a rate nearly equal to that calculated for the stage I portion of previously constructed progressive fatigue curves (see Figure 23), indicating a regeneration of a new highly deformed surface layer.

The composite diagram presented in Figure 39 collects the results from both the depth profile and recycling studies, expressed in terms of the induced changes in excess dislocation density [see Chapter V, Section A.1.a]. Part A of Figure 39 provides depth profiles for the specimens cycled to 75 and 95% of the life, obtained by incremental surface layer removal to a total depth of 400 μm. Part B of Figure 39 again exhibits the effect of the recycling procedure on the defect concentration of the new surface grains which, at the outset, have an inherent imperfection given by the plateau level after prior fatigue. The specimen subjected to 75% prior fatigue was recycled only 5% and then analyzed in depth to reexamine the defect concentration and distribution. The second depth profile for this specimen, Part C of Figure 39, discloses that the recovery phenomenon is not restricted to grains located at the surface, but rather occurs throughout the cross section. Comparison of the profile heights

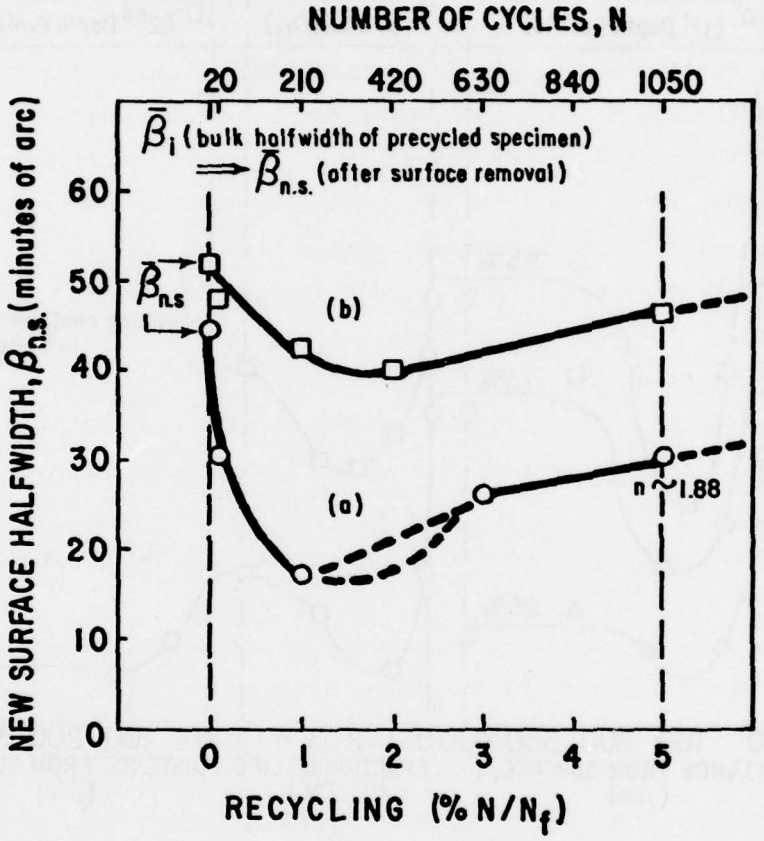


Figure 38. Effect of recycling on the (new) surface halfwidths after removal of a 400-μm surface layer from prefatigued specimens: (a) prior cycling to 0.75 N/N_f, and (b) prior cycling to 0.95 N/N_f.

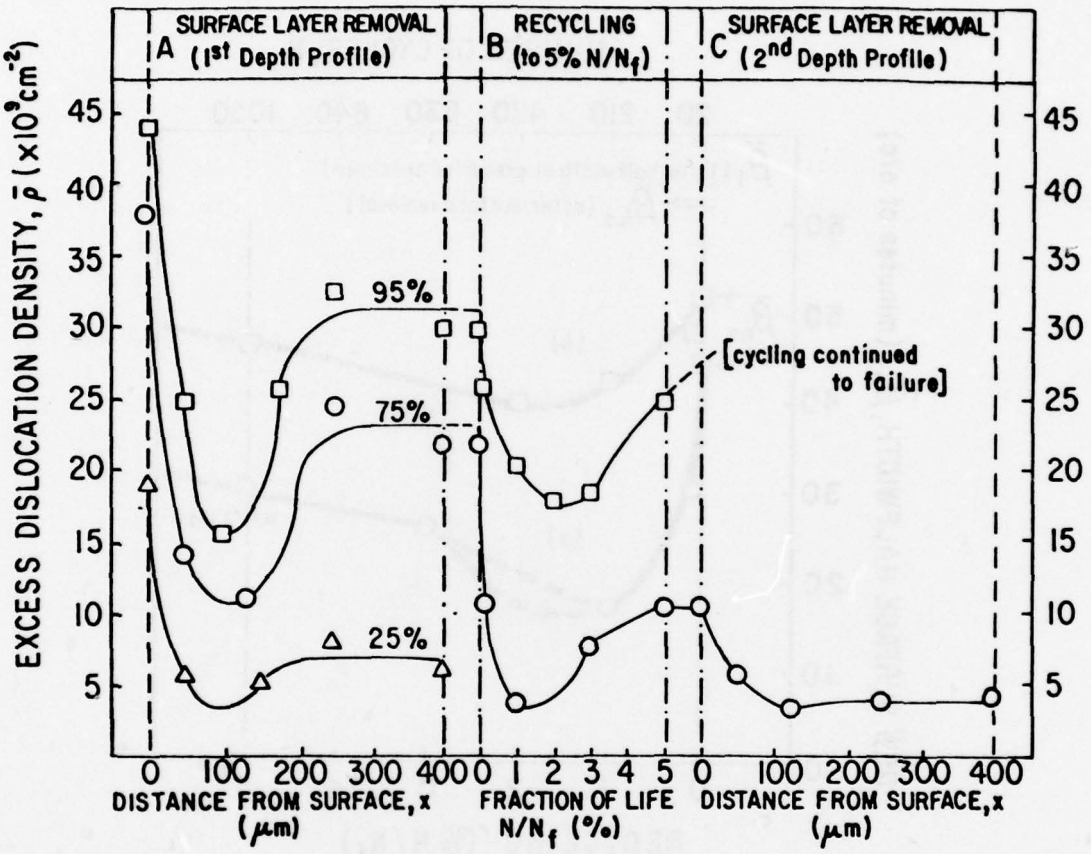


Figure 39. Composite diagram for Al 2024 specimens given prior cycling to 75 and 95% of their fatigue life at ±200 MPa, followed by a surface removal and recycling procedure (A) and (B), and either continued cycling or depth profile analysis (C).

in Parts A and C of Figure 39 confirms the overall substructural recovery. An equivalent surface removal and recycling sequence leads to less dramatic reversal of previous deformation induced by precycling to 95%. To measure the effect of the "treatment" on the fatigue life, instead of interrupting the recycling procedure to obtain a second depth profile, this specimen was simply cycled to failure. The total number of cycles recorded during recycling before failure represents about 80% of the average fatigue life for virgin specimens. The net gain in fatigue resistance achieved as a result of the treatment is thus on the order of 75%, the sum of the fractions of the normal life run prior to and after surface removal, less 100%. Subsequent experiments showed that surface removal promotes near total restoration of the entire life for specimens precycled 75% or less.

5. Effect of Grain Size and Radiation Type on Progressive Fatigue Curves

The final phase of the commercial alloy fatigue investigation was designed to test whether the knowledge of the surface and bulk substructural response to cycling could be put to practical use in terms of fatigue life prediction. This included comparison of the x-ray data for Al 2024 specimens having different grain sizes and inherent halfwidths, and experimentation with x-ray radiations with various penetration capabilities.

a. Comparative X-ray Data for Different Grain Sizes. In order to measure the effect of grain size on the substructural response to fatigue cycling, x-ray rocking curve analysis was applied to the Al 2024, batch B specimens for comparison with the data for the larger grained, batch A specimens tested previously. The proportional limit for monotonic testing for batch B, given in Table 3, was higher than for batch A, and the intrinsic rocking curve width was smaller, following a typical Petch-type relation between the flow stress and the inverse root of the grain size.

The rocking curve analysis employing copper radiation and carried out as a function of the fraction of fatigue life during cycling at ±280 MPa, equivalent to the proportional limit of batch B, is recorded in Table 6. Comparing the data with the incremental fatigue results for batch A

TABLE 6 - X-RAY ROCKING CURVE HALFWIDTHS RECORDED FOR CYCLED Al 2024, BATCH B, EMPLOYING Cu, Mo, AND Cr INCIDENT RADIATION; σ_a = ±280 MPa

No.	% N/N_f	CuKα			MoKα			CrKα		
		$\beta_{meas.}$	β_{median}	$\overline{\beta}$	$\beta_{meas.}$	β_{median}	$\overline{\beta}$	$\beta_{meas.}$	$\overline{\beta}$	$\overline{\beta}_{hkl}$
0	unde-formed (β_o)	20.6 min	21 min	0	22.2 min	21 min	0	26.1 min	0	0
1	5%	25.8	28	15.5	23.2	24	6.7	28.5	11.4	12.1
2	25	34.4	32	27.5	26.1	28	13.7	32.7	19.7	13.8
3	50	36.5	36	30.1	31.6	32	22.4	32.9	20.0	16.2
4	75	37.9	40	31.8	37.1	36	29.7	33.6	21.1	18.6
5	95	40.0	40	34.3	41.3	40	34.8	35.1	23.5	21.1
6	100	47.7	44	36.3						

(see Table 4), the halfwidths throughout the life are found to be on the order of one-half the breadths measured for the larger grain size stock. Since the intrinsic curve width of 20.6 minutes of arc for batch B specimens represents about half that for batch A samples, the corrected halfwidths, $\overline{\beta}$, show a similar correspondence for the two batches. Figure 40 shows the juxtaposition of progressive fatigue curves for the 44- and 33-μm grain size stocks. The defect response of the surface grains, manifested by a three-stage sequence in halfwidth variation with cycling, is very similar for the two batches. In addition, while the magnitudes of the corrected rocking curve widths differ, the slope and extent of the second stage are identical for the two curves. The multistage configuration of the progressive fatigue curves obtained by analysis with copper radiation is thus found to be consistent for both cycling at widely different stress amplitudes and for alloy stock with different grain proportions.

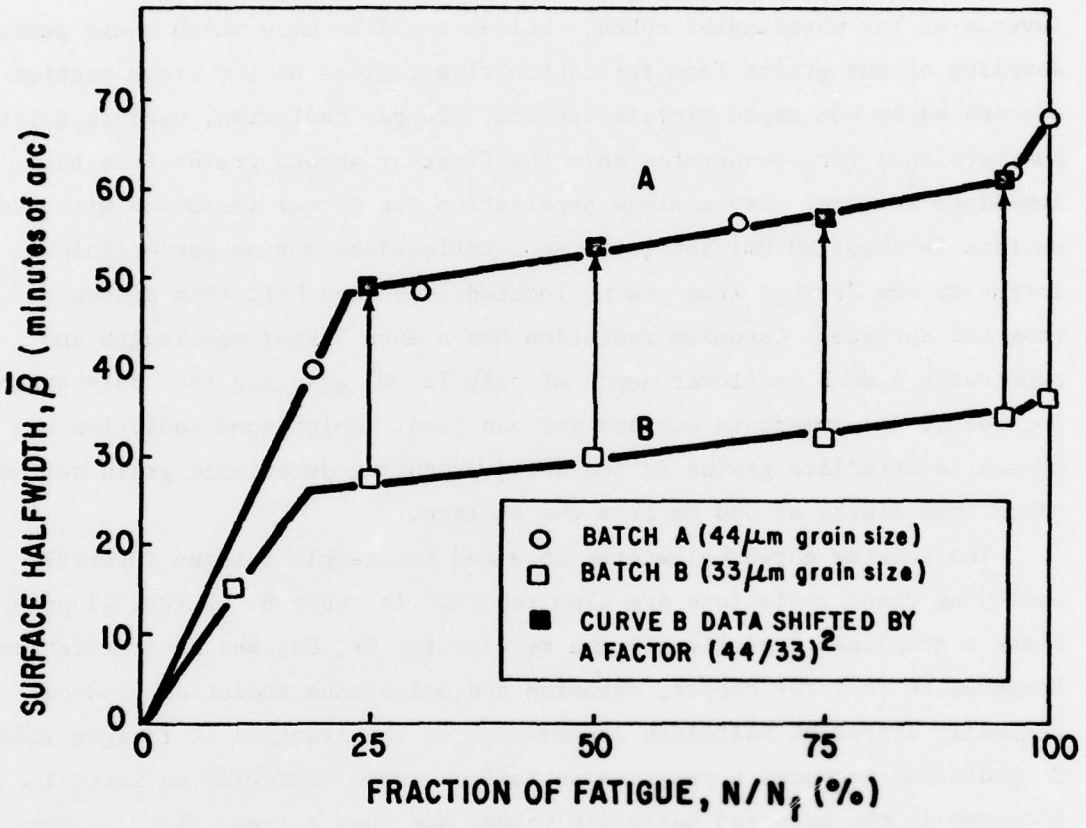


Figure 40. Comparison of progressive fatigue curves for 44- and 33-μm grain size Al 2024, cycled at stress amplitudes equivalent to their respective static proportional limits.

b. X-ray Analysis Employing Cr, Cu, and Mo Radiations. The substructural response of the bulk material as a function of the fatigue life was investigated previously by incremental removal of surface layers to obtain representative depth profiles. To provide a more complete picture of the fatigue response as a function of distance from the surface, analysis was performed nondestructively by using x-ray radiations with different wavelengths. Since the relative penetration capacity is related to the inverse of the wavelengths cubed, choices could be made which would permit sampling of the grains from the distinctive regions of the cross section elucidated by the depth profile studies. Copper radiation, used in all the analyses thus far, penetrates only the first or second grains from the immediate surface. Its maximum penetration for normal incidence with the surface is about 80 μm; thus, the spot reflections having perceptible intensity are derived from grains located less than half this distance from the surface. Chromium radiation has a much larger wavelength and penetrates a much shallower depth of only 12 μm, assuring that only grains located at the immediate surface are analyzed. Molybdenum radiation was chosen to irradiate grains in the bulk, producing detectable grain reflections from depths of 350 μm from the surface.

The rocking curve halfwidths obtained for sample fatigue intervals employing these radiations are also recorded in Table 6. Figure 41 presents a graphical depiction of the results for Cr, Cu, and Mo irradiation. Compared to that for copper, chromium and molybdenum radiation produce radically different halfwidth dependences on the fraction of fatigue life. Cr radiation produces a progressive fatigue curve featuring an initial increase in the measured halfwidth value, and then a long, flat, "saturated" plateau region with negligible slope, as shown in Figure 41a. Given its relatively broader intrinsic halfwidth, β_o, analysis with Cr radiation generates smaller corrected halfwidths, $\overline{\beta}$, during the life than does Cu radiation, as shown in Figure 41b. Analysis with Mo radiation, on the other hand, generates rocking curve breadths as a function of the life fraction which show no tendency to conform to a multiple-stage expansion sequence. Instead, a nearly linear dependence of the curve breadths is obtained from 2.5 to 95% of the fatigue life. The terminal, or critical

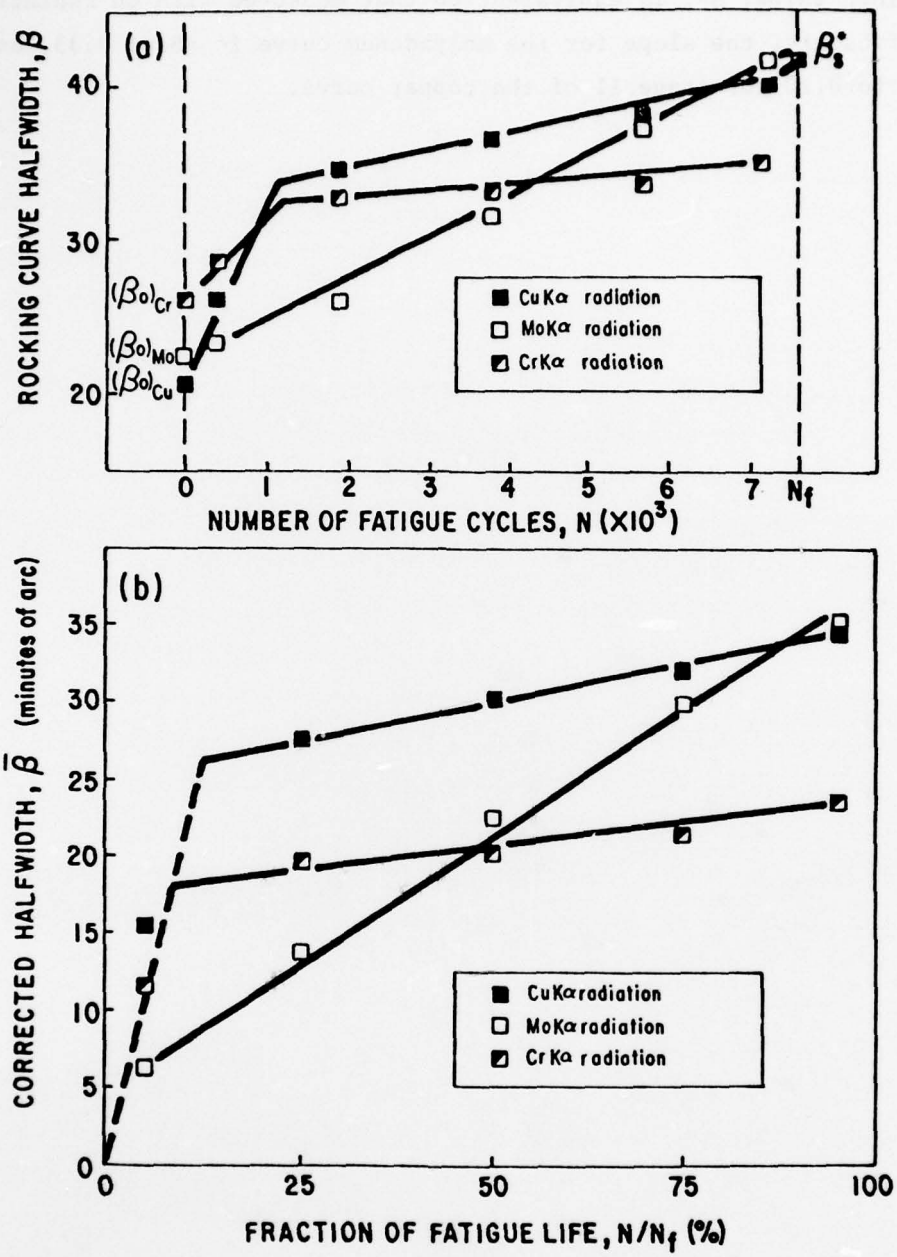


Figure 41. Comparison of progressive fatigue curves for Al 2024, batch B, using x-ray radiations with different maximum penetration depths: (a) measured halfwidth, β, vs N; and (b) halfwidth, $\bar{\beta}$ (corrected for the halfwidth, β_o, of the virgin specimen), vs N/N_f.

halfwidth value, $\overline{\beta}^*$, is equivalent to that measured with Cu radiation. Significantly, the slope for the molybdenum curve is about 0.33, as compared to 0.10 for stage II of the copper curve.

V. DISCUSSION

A. SINGLE-CRYSTAL STUDIES

1. Preferential Surface Layer Work Hardening

The x-ray rocking curve studies and reflection topography investigation of tensile deformed single crystals provided convincing microstructural evidence in support of the preferential surface layer hardening concept. For such diverse materials as silicon, aluminum, and gold subjected to uniaxial monotonic deformation, the rocking curve halfwidths measured at the surface were substantially higher than those of the bulk regions, signifying a decreasing gradient in the concentration of lattice imperfections from the surface to the interior. Topographic imaging of the induced microstructure revealed that the surface layer suffers a pronounced lattice breakup into highly strained and misoriented subdomains as compared to the bulk material.

a. Calculation of the Excess Dislocation Density. In order to be physically meaningful, the change in the rocking curve breadths must be interpreted in terms of microstructural mechanisms directly related to the macroscopic mechanical properties of materials. The correlation of the dislocation configuration in the crystal lattice to both the x-ray reflection peak broadening and the actual deformation response provides the required link between experimental observation and behavior. While calculation of the dislocation density from the x-ray diffraction line breadth is a routine procedure, the assumptions made in the various computational formulations differ. In addition, though dislocations represent intrinsic lattice defects responsible for the substantial reduction in the theoretical strength of an otherwise perfect crystal, their multiplication and interaction also result in the strengthening phenomenon known as work hardening. A measure of their concentration is thus important to evaluating the degree of work hardening incurred during deformative processes.

A comprehensive investigation of strain hardening in metals requires elucidation of the number, distribution, and arrangement of dislocations,

and the interaction among dislocations and with other substructural entities such as stacking faults, vacancies, interstitials, impurity atoms, and precipitates and inclusions. In a deformed metal, it is known that excess dislocations of one sign can be concentrated in a large variety of distinct boundaries producing subdomain tilt or misorientation, or may be homogeneously distributed over local regions to produce a finite lattice curvature[155]. It can be presumed that the x-ray peak breadths are controlled primarily by tilts and/or curvature due to ill-defined walls and dislocation pileups and the dislocations in the domains between them[168,169]. The high local stresses around the dislocation groups, vacancies, and interstitial atoms, and the distortions at the dislocation cores and stacking faults between partials all contribute to the tails of the diffraction peaks. A reduction in the main peak broadening would be expected if the long-range stresses due to pileups and internal subdomain strain were reduced by segregation into sharper boundaries, concomitant with annihilation of excess dislocations of opposite sign. Such a polygonization effect can be associated with the reduction in yield strength, or flow stress, typical for instance to the substructural recovery, reversion of cold work, and strain energy reduction induced by annealing at elevated termperature.

Finally, the computation of the excess dislocation density from the rocking curve halfwidth, assuming a predominance of misorientation tilt and curvature over the particle size effect when the domains are large, depends on the presumed arrangement of the individual domains. Cottrell[170] suggested three possibilities, including a regular alternation in misorientation, successive misorientations of the same sense producing a uniform curvature, and a random succession of positive and negative tilt orientations. The multimodal rocking curves from uniaxially deformed crystals are best approximated by the first or latter configurations. The average misorientation will be near zero, but the local misorientations give rise to rocking curves that are independent of the volume irradiated. This type of defect distribution should apply equally well to the misorientation induced by high static tensile stressing and substructure produced by repeated slip reversals during push-pull fatigue cycling. Breadth differences are thus ascribed to the number of dislocations in the loosely defined walls, their spacing, and their concentration within the subgrains.

According to Hirsch[155], the subcrystals may then be assumed to be misoriented about a mean position, with their normals distributed according to a Gaussian Law (see Figure 45). The tilt angle, α, is given approximately by $\beta/3$. The dislocations are randomly distributed so that there is a 50% change for two dislocations of the same sign being adjacent to one another, and forming a small wall with $\alpha = b/h$, where b is the magnitude of the Burgers vector and h is the wall spacing. The dislocation density, ρ, is then taken as $1/h^2$, and as shown also by Vassamillet and Smoluchowski[168].

$$\rho = 1/h^2 = \beta^2/9b^2.$$

b. Comparison of the Work Hardening Response for Model Materials. Rigorous quantitative comparison of the x-ray results among the three single-crystal species is limited by the differences in test conditions such as temperature and degree of deformation. The qualitative aspect of the microstructural response, namely the dependence of the rocking curve breadths with depth, represented by the depth profiles in Figure 13, is easily perceived to be consistent and material independent. Figure 42a contrasts the "deformation gradients" with depth for the three materials. Here, the gradients are expressed in terms of the absolute excess dislocation densities, ρ, calculated using the Hirsch relationship discussed in the previous section and the halfwidths corrected for the intrinsic imperfection, β. Figure 42b presents the dependence of the excess dislocation densities at each depth, x, to that of the constant bulk value (ρ_x/ρ_i). It can be seen that silicon, which begins with a very low baseline excess dislocation density of 4×10^5 cm^{-2} after annealing and polishing, exhibits a high surface density and the lowest interior density after deformation. This results in a steeper gradient than observed for either aluminum or gold which starts with denser dislocation populations, on the order of 10^8 cm^{-2}, in the virgin state. After deformation, the interior dislocation densities for aluminum and gold are essentially the same, but the aluminum which was subjected to greater plastic strain shows a larger

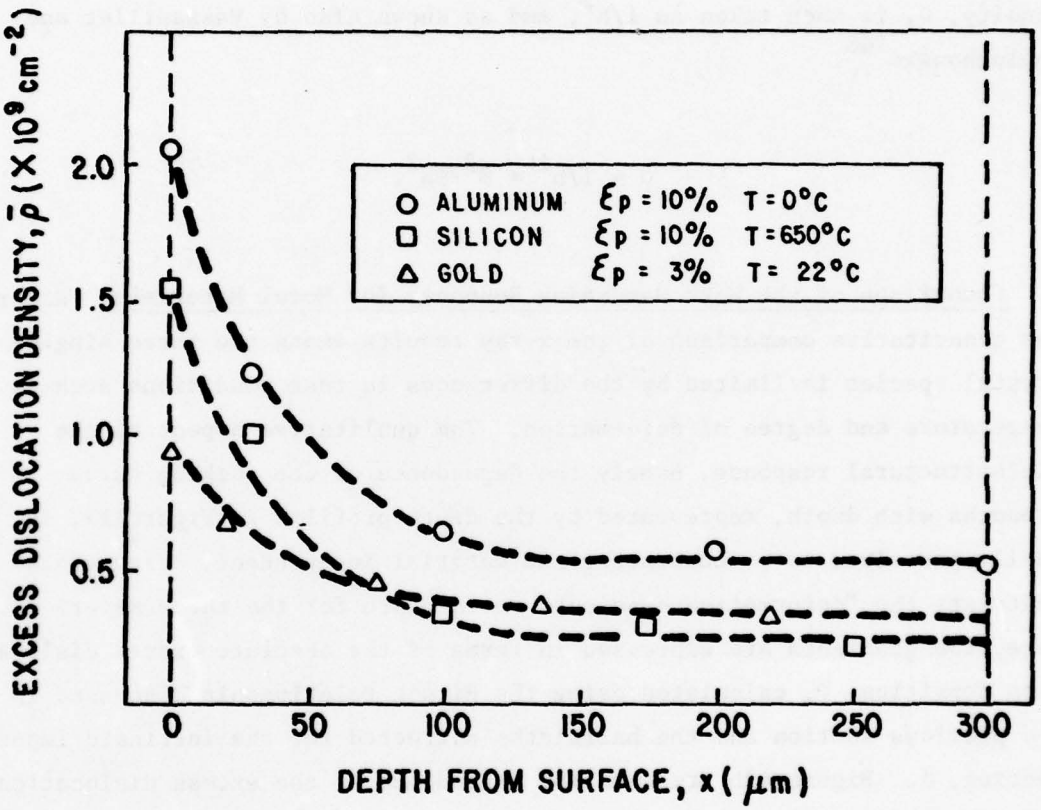


Figure 42a. Experimental gradients of the excess dislocation density with depth from the surface for tensile deformed monocrystals

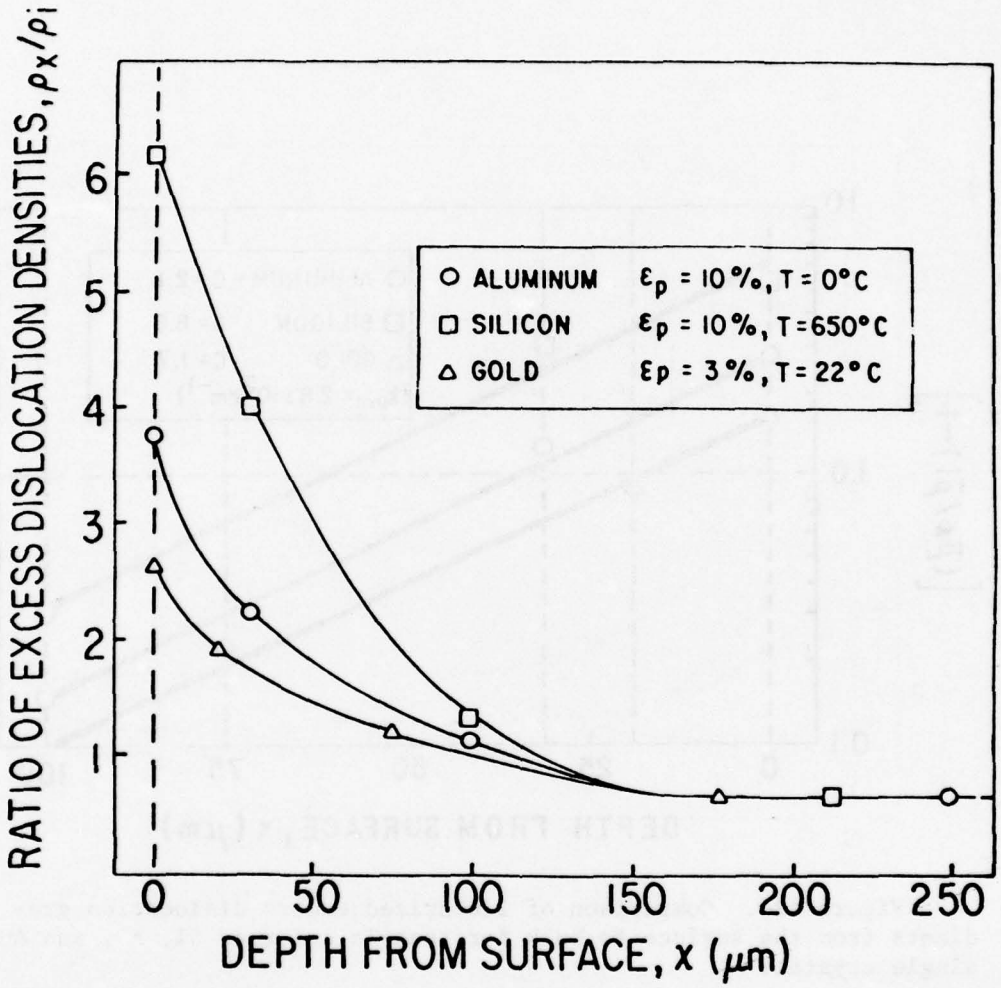


Figure 42b. Ratios of the excess dislocation density at various depths, x, to the constant bulk density, ρ_i, for tensile deformed monocrystals

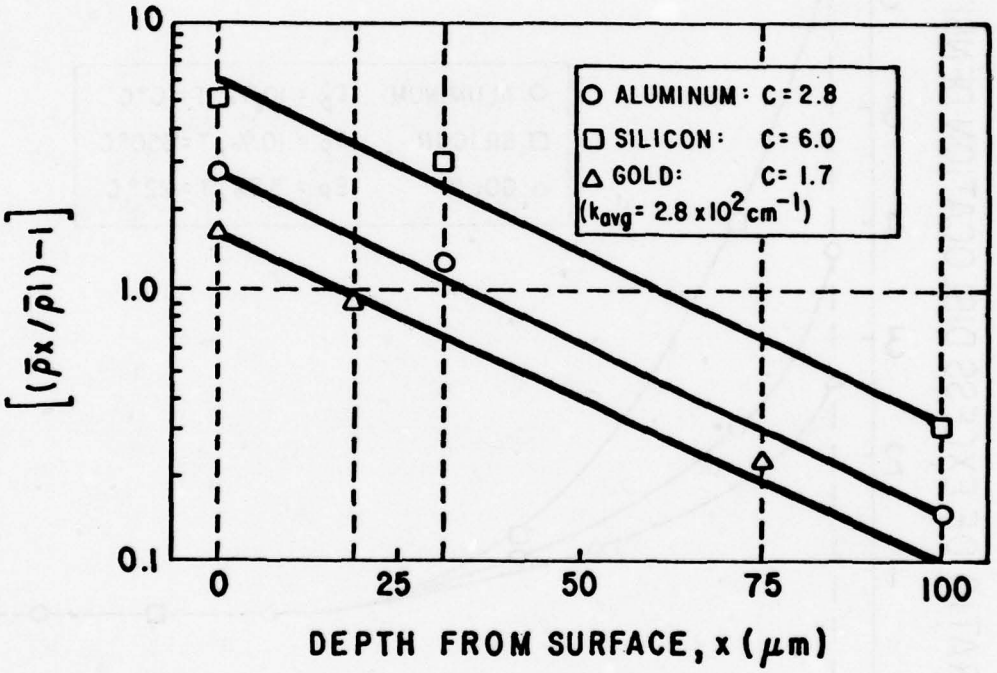


Figure 42c. Comparison of linearized excess dislocation gradients from the surface to bulk for tensile deformed Si, Al, and Au single crystals

surface density and therefore a steeper gradient. The magnitude of dislocation density reduction from the surface to bulk is certainly attributable in part to crystal structure and orientation. The steepness of the silicon curve is likely enhanced by deformation at elevated temperature and the stability of the induced defect configuration at ambient temperature, relative to the fcc metals.

In comparing the results obtained for silicon and aluminum, it is useful to recall the inverse relationship between the ratio of their inherent halfwidths $[\beta_{oAl}/\beta_{oSi}] = 16$, and their relative surface and bulk halfwidth expansions due to deformation $[(\beta_{s,i}/\beta_o)_{Al}/(\beta_{s,i}/\beta_o)_{Si}] = 1/15$, as shown by reference to Table 1. This indicates that there is an insensitivity of absolute halfwidth values measured after any given plastic strain to the intrinsic or baseline halfwidths. In other words, a high degree of initial perfection does not necessarily imply an insufficiency of multiplication sites to produce a high degree of work hardening, especially if the activation of multiplication mechanisms and motion of dislocations is enhanced by testing at an elevated temperature, as was true for the deformation of silicon above the ductile-brittle transition.

The dislocation gradients from the surface to bulk for silicon and aluminum deformed similarly to 10% plastic strain can easily be linearized to facilitate comparison. Russian investigators[171] found that the distribution of dislocation densities determined by a layer-by-layer etching technique applied to ground alkali halide crystals could be described by an equation of the form:

$$\rho(x) = \rho_i + (\rho_s - \rho_i)e^{-kx}, \qquad \text{(i)}$$

where ρ_i is the constant density established at some depth, x_i, and ρ_s is the surface density. Dividing each side of the equation by ρ_i, and taking the logarithms, gives:

$$\ln[(\rho_x/\rho_i) - 1] = \ln[(\rho_s/\rho_i) - 1] - kx \qquad \text{(ii)}$$

$$= \ln C - kx, \qquad \text{(iii)}$$

where $C = (\rho_s/\rho_i) - 1$. Substitution of the x-ray rocking curve data for silicon and aluminum derives curves with almost identical slopes, as shown in Figure 42c. A similar plotting of the data for gold monocrystals, deformed 3% plastically, also results in the same slope, which averages about 2.8×10^2 cm^{-1}. Thus, the k value is apparently material independent, while the value of the intercept, C, for each material is determined by the crystal structure, amount of imposed strain, and deformation temperature.

In comparing the results obtained for aluminum and gold, both fcc metals deformed under multiple glide conditions, the primary variables differentiating their respective profile gradients are material parameters such as comparative work hardening rates and propensities for surface oxidation, and test variables such as deformation extent and temperature. With regard to the role of oxide film formation on the preferential surface work hardening phenomenon, the generation of a decreasing deformation gradient from the surface to bulk after only 3% plastic straining of gold crystals suggests that surface hardening is not appreciably hindered by the absence of an oxide layer. At the very least it can be concluded that the presence of an oxide barrier to block dislocation egression is not a necessary prerequisite for surface hardening, but rather that pileup mechanisms are activated by slip interactions intrinsic to the surface layers of the crystal. Because of the large number of sites of dislocation sources at or near the surface, and because of the immediate interactions of the activated dislocation sources, a barrier effect is created to the egression of the dislocations from the bulk. The role of the surface layers in blocking dislocation egression, independent of a solid surface film, is in accord with the results of Kramer[31, 36].

c. Comparative Surface Layer and Bulk Hardening Rates. The magnitude of the decrease in halfwidths from the surface to bulk is determined by the relative work hardening rates of the two regions. It is appropriate at this point to speculate that there is a direct correspondence between the microscopic evidence of surface layer hardening represented by the x-ray

rocking curve halfwidths, and the mechanical evidence revealed by "surface layer stress" measurements performed by Kramer[64]. The surface layer stress, it is recalled, is defined as the quotient of the difference between the maximum load attained in an initial loading and unloading procedure, and the new flow load obtained after removal of the specimen surface and reloading, over the original cross-sectional area of the specimen, or $\Delta L/A_o$. This value is usually adjusted to reflect the fractional cross-sectional area constituting the work hardened region at the surface. Kramer's investigation showed that the surface layer stress for high purity aluminum and gold and Al single crystals varies with true plastic strain according to the relationship:

$$\sigma_s = C_s \varepsilon_p^{\,n}, \qquad \text{(i)}$$

where C_s is a constant and n is a work hardening exponent equal to that obtained in similar equations for the applied stress. In addition, the mechanisms advanced to describe strain hardening in multiple glide systems systems[172] generally predict a proportionality between the flow stress and the root of the dislocation density of the form:

$$\tau = \tau_o + \alpha G b \rho^{1/2}, \qquad \text{(ii)}$$

where τ_o is the stress required for dislocation motion in the absence of interfering defects, and α depends on the hardening model type. These models ascribe the hindrance to dislocation motion to the cumulative stress, or "back stress," due to piled-up arrays in a common slip plane, to elastic interaction with forest dislocations in an intersecting slip plane, or to drag stresses due to dislocation jogs or resistive line tension between pinning points of dislocation tangles. Since the x-ray rocking curve halfwidth, geometrically related to the lattice misalignment or the spread of subdomain misorientation, is taken to be proportional to $\rho^{1/2}$, there is an implied correspondence between the rates of change of

σ_s, or the resolved shear stress in the surface layer, τ_s, for monocrystals, and the surface halfwidth value, β_s, as a function of strain level. This relationship is implicitly supported by the microbeam experiments on low carbon steel by Taira and Hayaski[150], and by TEM studies of polycrystalline iron by Keh and Weissmann[173]. Within the plastic strain range investigated, it is also apparent that either the strain hardening of the bulk proceeds at a lower rate than at the surface or its activation is delayed until some critical strain level is attained. The latter behavior was found for fcc monocrystals oriented for single glide by Kramer[65], who concluded that the work hardening during stage I deformation was restricted to the surface layer, and τ_i was thus effectively zero. Slip on secondary systems could not start until the applied stress exceeded the sum of the surface stress and the stress required to activate new sources, and the mutual interaction between the surface and bulk during stage II eventually produced a measurable τ_i value. Japanese scientists[23] employed TEM analysis of Al single crystals to show that the surface dislocation density increases preferentially at low strain levels, but saturates after several percentages of plastic strain and is eclipsed by that of the bulk. However, it can be argued that the surface work hardening may actually predominate to greater strain levels, given the rather unjustified disparity in correction factors applied in this study to account for the respective propensities for surface and bulk relaxation.

Regardless of whether the deformation gradients common to all the depth profiles are caused by lower bulk strain hardening rates or by a delay in the initiation of such a response in the core region, the mechanistic explanation of the phenomenon can be reduced simply to a preferred activation of dislocation sources located at or near the surface, and an initially high mobility in conjunction with the high surface multiplication rates. These factors contribute to intense interaction of moving dislocations on multiple slip systems, entanglement, and work hardening in the surface layer. This layer then serves as a trapping or blocking agent, forming a barrier to dislocation egression. In the bulk, however, where the generation and multiplication of dislocations are less favored, the deformation induced increase in excess dislocation density, and at early stages the total dislocation density as well, lags far behind that at the

surface. Other investigators came to similar conclusions using etch-pit techniques for characterization of the dislocation structure in plastically deformed single crystals[25-27].

c. Subdomain Morphologies in the Surface Layer and Bulk Material. The topographic examination of strained single crystals provides further evidence of the preferential interaction of near-surface defects by imaging the resulting "debris." The correlation between the defect configuration and the rocking curve profiles can be modeled as shown in Figure 43. Figure 43a presents typical rocking curve profiles for undeformed, annealed, and polished silicon and aluminum specimens (i) and (ii), and for plastically strained crystals at the surface (iii) and in the bulk (iv). While the profiles for the virgin state of the two crystal species both have very narrow halfwidths, β_o, silicon typically has a much greater intrinsic perfection compared to the polygonized-type lattice of annealed aluminum. Figure 43b shows in schematic form the geometry inherent to reflection topography (i), the "mosaic-block" structure intercepted by and diffracting the crystal-monochromated incident beam (ii), and the distribution of misoriented reflecting domains induced by deformation and contributing to the broad rocking curves at the surface (iii) and narrower, multimodal curves in the bulk (iv). When lattice defects are introduced by deformation, the dislocations accumulated locally break up the lattice into coherently reflecting subdomains, or "particles." The total strain distribution giving rise to the overall halfwidth, β_T, derives principally from these regions of excess dislocation accumulation at the particle boundaries, which determine the misorientation angles between the subdomains. In the drawing, this misorientation is expressed by the angular relationship among respective normals, n_1, n_2, n_3, . . . , n_n. In addition, each lattice domain may suffer the internal generation of excess dislocations as a result of nonuniform or "bending" strain, as well as continuous lattice spacing changes due to the residual strain distribution, which gives rise to the component rocking curves, β_1, β_2, β_3, . . . , β_n, of the subdomains. At the surface of strained crystals, many subdomains reflect simultaneously by virtue of their small size, large population, and persistence over a wide angular range. Hence, the component peaks

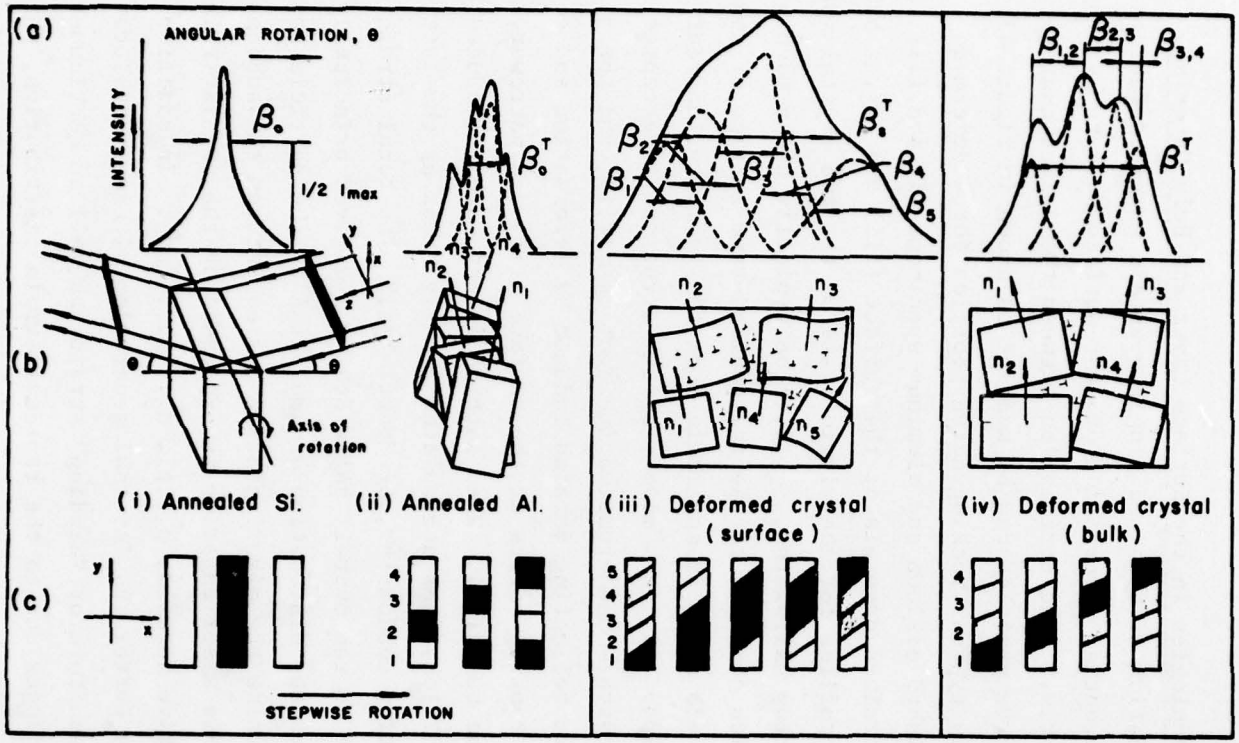


Figure 43. Correlation of x-ray rocking curves, crystal morphology, and topographic images: (a) typical rocking curve profiles; (b) illustration of reflection topography, misoriented subdomains along incident beam length, and statistical distribution of misalignment; and (c) schematic depiction of reflection images recorded during stepwise specimen rotation.

overlap sufficiently to produce a broad, smooth, overall rocking curve. X-ray topography affords an experimental deconvolution of the overall curve so that the internal strain of the contributing subdomains can be evaluated. As the irradiated portion of the crystal shown in Figure 43b (i) is rocked through its ideal reflection condition during the specimen rotation sequence, the topographic images for each angular position, shown in Figure 14 for deformed aluminum crystals and represented in the Figure 43(c) depictions, provide a basis for discriminating among the various lattice domains. In this manner, the reflection durations of the small subdomains can be extracted from the composite curve and analyzed separately. In theory, if the internal strain of the individual reflecting domains is expressed by its standard deviation, S_{is}, and the standard deviation of the misorientations of the particles is denoted by S_{ms}, then:

$$\varepsilon = (S_{is}{}^2 + S_{ms}{}^2)^{1/2},$$

where ε is directly related to the corrected overall rocking curve half-width, β_T, by presuming conformance to a Gaussian distribution [see Appendix C, Sect 3]. The differentiation between the surface layer and bulk substructures induced by plastic deformation is illustrated by Figure 43b (iii and iv). The small, highly strained domains comprising the surface debris exhibit mutual reflection throughout the wide reflection range of the total rocking curve, while in the bulk the larger, more perfect, subdomains reveal less misorientation as displayed by the reduced peak-to-peak distances. The narrow, multipeaked profile is not unlike that of the polygonized virgin aluminum crystals, and its diminished overall breadth from the surface value discloses a smaller excess dislocation density compared to the work hardened surface layer. The topographic elucidation of the surface and bulk substructure can be effectively exploited, therefore, to corroborate the quantitative evidence of preferential surface layer strain hardening.

2. Structural Response of the Surface Layer and Bulk to Fatigue Cycling

As suggested previously, a simple tension test can be visualized as representing the first half-cycle of a tension-compression fatigue cycling sequence, if a zero mean stress is employed and the stress amplitude applied is equal to the maximum stress achieved in the tension test prior to unloading. This affords an evaluation of the change in microstructural response and defect distribution occurring as a result of a transition from monotonic to alternating loading conditions.

a. Comparison of the Depth Profiles for Simple Tension and Push-Pull Fatigue. It has been shown that the initial tensile loading produces a highly deformed surface layer, while the bulk material suffers comparatively little substructural damage. Recalling the curve plotted in Figure 15, it may be observed that the effect of cyclic stress reversals is similar in many respects. The rocking curve measurements for aluminum single crystals cycled at a low stress amplitude indicate that a propensity for preferential surface layer work hardening is retained. Also, analogous to the monotonic behavior, the halfwidths in the bulk exhibit values commensurate to those of the virgin crystal. The depth profile, however, reveals an additional salient feature. In contrast to the simple gradient for monotonic deformation, which attains a constant minimum value at about 200 μm in depth, the curves for fatigued specimens decrease to a minimum halfwidth value at a lesser depth of about 75 μm, and then rise again to a plateau level in the bulk at a typical 200-μm depth. The halfwidth values in the subsurface, profile "well" region fall considerably below the intrinsic halfwidth of the virgin specimen.

It is likely that the unique profile conformation for fatigued specimens is influenced by reversals in the sense of the dislocation motion accompanying the alternating loading sequence. The redistribution of deformation induced defects during the cycling may explain the work hardening response which prevails in the surface layer, as well as the recovery phenomenon which occurs in the subsurface region. The enhanced generation and interaction of dislocations in the surface layer early in the fatigue life would lead to the observed halfwidth expansion. Net motion

of excess dislocations toward the surface would represent an additional contribution to the surface layer dislocation pileup and concomitant work hardening. At the same time, this behavior would promote recovery in the subsurface region, possibly aided by annihilation of excess dislocations by recombination with newly generated defects of opposite sign. Evidently, there is little or no activation of bulk dislocations and/or sufficient cancellation of induced excess dislocations of opposite signs, so as to leave the interior defect concentration unchanged from the value for the undeformed specimen.

b. Cyclically Induced Recovery in the Subsurface Region. The zone of approximately 125-μm thickness characterized by a low degree of lattice imperfection is also distinctive from a structural viewpoint. X-ray topography of the surface, intermediate, and bulk regions provides a qualitative basis for differentiation of the respective substructures. The immediate surface displays highly misoriented and fragmented lattice domains which reflect over a wide range of angles. Earlier studies by Levine and Weissmann[14] disclosed preferential subgrain formation in the interstriation regions at the immediate surface and their later development in the underlying regions. A transition to a corrugated or polygonized structure occurs at 50 to 100 μm in depth. This latter morphology suggests a more uniform and lower energy configuration of positive and negative dislocation arrays typical of a "dipole" or "Taylor" lattice[174]. The excess dislocation density is low, which reduces the lattice curvature inherent to even the virgin crystal, hence deriving smaller measured halfwidths. In the bulk, the more diffuse subdomain images give witness to a reinstitution of the degree of crystal imperfection intrinsic to the original, annealed specimen.

In a single crystal there are no effective sinks for locally distributed excess dislocations of one sign. Whether the excess dislocations are located inside the subdomains or in the boundaries between them, they will always contribute to the composite rocking curve width. Therefore, in order to witness a reduction in the halfwidths, as characterized by the subsurface region generated by low amplitude fatigue, there must be a redistribution of defects, a preferential production of dislocations of the

opposite sign, or both. Comparison of the areas above and below the baseline halfwidth of Figure 15 appears to support a redistribution by migration toward the surface; the area of reduced halfwidth values between 25 and 200 μm in depth compares favorably with the surface region of enhanced halfwidth values. The redistribution and cancellation of defects in the subsurface, aided by cyclically induced vacancy production promoting dislocation climb, would in turn facilitate continued egression from the bulk by providing an unobstructed path for mobile dislocations from the crystal interior.

For this model of in-depth fatigue behavior, the profile "well" region merely forms a transition between the free surface and the vast continuum represented by the bulk of the specimen. Regardless of its specific origin, then, the implication of the low halfwidth region is that the structural response to fatigue cycling constitutes a dynamic interplay between the surface layer and bulk. It will be seen later that the structural response of Al 2024, when cycled at stress amplitudes which ultimately produce fatigue failure, involves a reciprocating buildup of the dislocation densities in both the surface layer and the specimen core.

Two additional comments might also be appropriately offered at this time. First, the work hardening of the surface layer, even at stress amplitudes below the endurance limit, indicates why previous studies identified the introduction of cold work during cycling in both the "safe" and "unsafe" ranges of stress[140], since these x-ray studies were undoubtedly confined to surface analysis. Second, the alternative view that the surface to well-bottom gradient is produced by excess dislocation egression during the electropolishing required to experimentally measure the gradient does not invalidate the proposed interpretation of the profile conformation. As a consequence of the rise to a plateau level further into depth, the polishing process itself cannot be held solely responsible for the observed halfwidth reduction to a minimum value in the subsurface region. A substructural differentiation must exist among the profile-well region and the adjacent surface and bulk regions, and there is very little likelihood that the effect is purely an artifact.

B. Al 2024 ALLOY STUDIES

1. Critical Surface Layer Work Hardening as a Precursor to Cyclic Failure

A tendency for the surface layer to harden preferentially has been shown to occur for both monotonic and fully reversed fatigue stressing of single crystals. Either form of deformation results in a decreasing rocking curve halfwidth gradient from the surface into the interior. Increasing the plastic strain for simple tension, and presumably the number of cycles for fatigue testing, acts to increase the slope of the measured gradient, representing the decrease in excess dislocation density with depth. This can be perceived as a strengthening of the surface layer barrier to dislocation egression from the bulk. The present discussion will be restricted to elucidation of the fatigue response at the immediate surface of a commercial alloy.

The results of incremental fatigue cycling experiments on Al 2024 alloy specimens indicate that work hardening of the surface is not unique to single crystals. The halfwidths measured for grains located at the surface of the alloy specimens are also enhanced by the cyclic stressing. In good agreement with the results of Taira and Hayashi, whose studies employed an x-ray microbeam technique[147,148], a three-stage sequence in the surface hardening response is obtained. This behavior can be briefly summarized as a rapid increase in surface grain halfwidths during the initial 20% of the fatigue life, a more gradual width expansion during the second stage, and a final rapid increase during the last 10% of the life prior to fracture.

a. <u>Effect of Applied Stress Amplitude and Grain Size on the Halfwidths.</u> The shape of the progressive fatigue curves obtained for different stress levels are all similar, differing only in terms of the absolute halfwidth at which the transition from one stage to the next is initiated, as may be concluded by reference to Figure 21. As shown by Figure 23, the magnitude of the surface layer halfwidths at any fraction of the fatigue life is nearly the same for the three stress amplitudes employed. In addition, the surface halfwidth at the ultimate failure is identical for stressing at the disparate levels and is therefore denoted as a critical value, β^*.

In a systematic investigation of the "surface layer stress," defined previously, as a function of the fatigue life for Al 2014-T6, Kramer also showed that a propagating fatigue crack was formed whenever the work hardening in the surface reached a critical value[114]. This parameter was also found to be independent of the stress amplitude and insensitive to prior fatigue history and testing environment. His proposal[111,112] that the cyclically generated surface layer functions in the same way as for single-crystal deformation by opposing the egression of dislocations from the bulk appears applicable to the x-ray results for the Al 2024 alloy as well. Kramer reasoned further that when the barrier becomes sufficiently strong the local stress fields associated with the accumulation of excess dislocations in the surface layer pileups exceed the fracture strength, and cracks are initiated. By utilizing the relation proposed by Friedel[175] to calculate the cumulative stress of a network of pileup groups of n dislocations, the critical halfwidth, β^*, from the rocking curve analysis and critical surface surface stress, σ_s^*, generated during the cycling would enable calculation of the intensification of the applied stress by the pileup. The stress across the pileup, $\tau_p = n\sigma_a/2$, should correspond favorably to the fracture strength of the material.

Presuming a similarity of the critical halfwidth behavior to that of the critical surface layer stress (see Figure 4b), the intermittent and arbitrary changes in the stress amplitude during the cycling process would only affect the rate of approach toward the critical surface dislocation density, ρ_s^*, while leaving its magnitude unchanged. That is to say, the rate of growth of the halfwidths under variable amplitude conditions may be subject to anomalous effects of large decrements in the stress limits, and thus deviate from a linear cumulative damage law, but the end point, β_s^*, would be invariant. This would imply an independence of cyclic history as well as of the particular applied stress for constant amplitude cycling.

The progressive fatigue curves in Figure 40, however, show that a difference in alloy grain size does produce a change in the β_s magnitude. Reference to Table 3 shows that Al 2024 specimens with grain sizes differing by about 25% also have significantly different tensile and fatigue properties. As indicated by its 50% greater intrinsic halfwidth, the

larger grained alloy incorporates a higher degree of imperfection within each grain. As a result, its static proportional limit is correspondingly lower, following a typical relationship of the Hall-Petch type.* The progressive fatigue curves for the two alloy batches, when cycled at their respective proportional limits to insure a comparable degree of net dislocation motion, reveal a difference in the magnitude of the microstructural response for the two grain sizes. Nevertheless, after the rapid saturation hardening of the surface layer during stage I, the relative halfwidth expansions for the two grain sizes vary consistently for the balance of the fatigue life. As depicted in the figure, the curves can be related by a simple shift factor such that $\overline{\beta}_A/\overline{\beta}_B = (d_B/d_A)^2$, where d_A and d_B are the alloy grain diameters. Given the limited scope of these experiments, the formal relationship could be regarded as purely fortuitous. Yet, the similarity in microstructural response during the life suggests that the amount of testing to characterize the fatigue microstructure for different grain sizes may be conveniently reduced by some shift factor of this type.

It is likely that other material variables indicative of intrinsic hardness, such as the precipitate morphology produced by aging treatment and the cold work introduced by prior deformation, will also have predictable effects on the ultimate substructure and associated critical halfwidths induced by subsequent fatigue. The microstructure typical of the saturation stress for annealed and cold worked fcc metals has been found to be equivalent for fcc metals of both planar and wavy slip mode character[8]. The TEM investigation by Greenhut[95] disclosed a similarity in the final cyclically induced cell structure of Al 2024 specimens given various aging treatments. Though the study represented a "bulk" analysis, the processes described may be considered to occur in the surface regions as well, albeit with a greater degree of fragmentation and cell

---

*Based on the premise that the grain boundaries obstruct dislocation slip, since the resultant pileups in the coarser grained alloy contain a greater number of dislocations, a higher stress multiplication is produced in adjacent grains. Thus, a smaller applied stress is required to cause slip to pass through the boundary and induce macroscopic flow.

elongation, and at an earlier fraction of the life. A genuine correspondence of a critical β^* value to incipient fracture for the general case would thus appear to be contingent on the consistency or predictability of its magnitude for various initial conditions of an alloy.

b. Correlation of the Surface Topography to the Three-Stage Fatigue Life. At this juncture, the results pertaining to the x-ray rocking curve analysis and surface microscopy will be collected and listed to better facilitate their integration with the in-depth results discussed in the following section. It is emphasized that the three-stage sequence comprising the fatigue life presented below bears no particular relation to the three stages typically distinguished for the crack propagation process. Such confusion can be avoided if it is remembered that the division of the fatigue response for this investigation is predicated purely on the basis of the behavioral pattern of rocking curve halfwidth expansions exhibited during incremental fatigue. Thus, the behavior as a function of the progressive fatigue cycling can be summarized by the following observations:

Stage I (N/N_f = 0-25%):

The hysteresis loop area decreases initially as mobile dislocations are generated and interact in the surface layer and shifts in the negative displacement direction. The rocking curve halfwidths increase rapidly during this initial stage to a saturation level. No evidence of slip is observed by surface microscopy.

Stage II (N/N_f = 25-95%):

The cyclic stress-strain response indicates a macroscopically steady-stage behavior throughout this period. The rocking curves measured for surface grains display an almost imperceptible increase. Between 75 and 95% of the life, morphological indications of surface damage appear. The slip traces revealed by surface microscopy at about 75% of the life gradually become more densely packed, and at 95% are collected into bands on the surface. Slip band extrusion and incipient cracks are also evident at this late stage of the life and contribute to a growing surface relief.

Stage III (N/N_f = 95-100%):

The hysteresis loops widen just prior to failure as the propagation of fatigue cracks leads to an eventual structural instability[176]. An upturn in the halfwidth curves occurs as the intense dislocation pileup at the surface layer induces cumulative stresses which exceed the barrier strength, microcracks are initiated, and the specimen begins to approach final rupture.

It is evident from this analysis of the surface layer response that none of the experimental characterization techniques can be employed during the transient second stage to predict accurately the remaining fatigue life. The stability of the halfwidths at the surface between 25 and 95% of the life inhibits the evaluation of the total life expended, or total fatigue ductility, or resistance, "used up" after any amount of cycling intermediate to these percentages. The emergence of slip bands and related surface relief are incurred too late in the life to be of any great predictive value. It will be shown in the next section that the in-depth response provides new information which may be utilized in fatigue life prediction.

2. Influence of the Bulk Response on the Fatigue Life and Failure

It has been shown that the surface halfwidths followed a three-stage expansion sequence during the progressive cycling of Al 2024, terminating at a critical halfwidth, β^*, at failure. The rapid excess dislocation generation in the surface layer adequately explained the rapid halfwidth expansion early in the life. A question remained, however, as to what triggered the development of PSB's and incipient cracks which became observable during the prolonged second stage of apparent saturation in the surface hardening response. The depth profiles generated for alloy specimens cycled to increasing fractions of the total life showed that the intensification of the slip markings at the surface might be ascribed to an eventual elevation of the halfwidths in the specimen interior, and hence to a dynamic interplay between the defect structures induced in the surface layer and bulk. The local stress concentration due to cracking at the surface ultimately then causes the final increase of the surface halfwidths prior to failure.

a. Comparison of the Damage Accumulation Rates of the Surface and Bulk. Recalling Figure 37, it is apparent that substructural changes in the grains in the specimen interior become measurable after only a few percentages of the fatigue life. After 25% of the life, a profile "well" becomes distinguishable in the subsurface region, much like that observed for single crystals. As the cycling continues, the well becomes more pronounced as the surface hardening and bulk plateau level increase relative to the minimum halfwidth constituting the well bottom. As disclosed by the figure, the surface and bulk halfwidths exhibit significantly different rates of change during the various stages of the fatigue life. It is evident that the relative halfwidth expansion for the surface layer after only 0.15% of the life by almost 30 minutes of arc represents nearly half of the total increase of 62 minutes computed for the corrected halfwidth over 95% of the life. Additionally, there is little change in β_s during nearly the last quarter of the fatigue life as indicated by the near coincidence of the data for the curves representing 75 and 95% at the surface. The relative expansions in the bulk, on the other hand, exhibit nearly equal increments for each quarter of the life, as is immediately evident from the regular spacings of the plateau levels in Figure 37. Inspection of Table 7 provides a basis for evaluation of the differential surface and bulk halfwidth expansion rates. The incremental change in the surface halfwidth during the initial 0.15% of the fatigue life is 45% of the total change measured during 95% of the life, but there is only a 7% change in this value during the period from 75 to 95% of the life. In the bulk, the corresponding plateau halfwidth values show more consistent incremental changes for each of the fatigue intervals; for each quarter of the life an expansion of 15 to 30% of the total increase over 95% of the life is obtained. A graphical representation of the behavior is provided by Figure 44, which collects the information obtained in both the incremental fatigue studies of the surface layer and the depth profile studies. The halfwidths at the surface increase rapidly, following the broken curve, and disclose a predominance of the work hardening in the surface layer up to about 25% of the fatigue life. During the period from 25 to 95% of the life the surface halfwidths expand more gradually, with a slope of about 0.23. The fatigue response during this intermediate

TABLE 7 - COMPARISON OF RELATIVE HALFWIDTH EXPANSIONS IN THE SURFACE LAYER AND BULK MATERIAL DURING INCREMENTAL FATIGUE CYCLING OF Al 2024 SPECIMENS

Portion of Fatigue Life During Which Halfwidth Expansion Increments Occurred (%)	Incremental Change in Surface Halfwidth, $\bar{\beta}_s$, Relative to Total Expansion During the Fatigue Life (%)	Incremental Change in Bulk Halfwidth, $\bar{\beta}_i$, Relative to Total Expansion During the Fatigue Life (%)
0-0.15	45	18
0.15-25	21	29
25-75	27	40
75-95	7	13
	100	100

stage in the life is apparently influenced more strongly by the enhancement of the bulk halfwidths, as indicated by the steeper gradient exhibited by the solid line, with a slope of about 0.40. It will be seen that this more pronounced gradient obtained for the bulk halfwidth expansion as a function of fatigue life is extremely useful in the prediction of ultimate failure.

b. Dyanmic Interplay of Lattice Defects Generated in the Surface and Bulk. The similarity between the depth profiles of fatigued single crystals and cycled alloy specimens has been amply demonstrated. The mechanistic arguments proposed to explain their distinctive shape must also be similar. As in the case of single-crystal fatigue, the preferential buildup of a work hardened surface layer during the initial fatigue cycles is dictated by the favorable conditions for dislocation multiplication and subsequent interaction inherent to the grains constituting the free surface of polycrystalline specimens. The long-range stresses produced by the cumulative effect of dislocation pileups in these surface grains eventually influence the microplastic response of the bulk material. Thus, the disparity

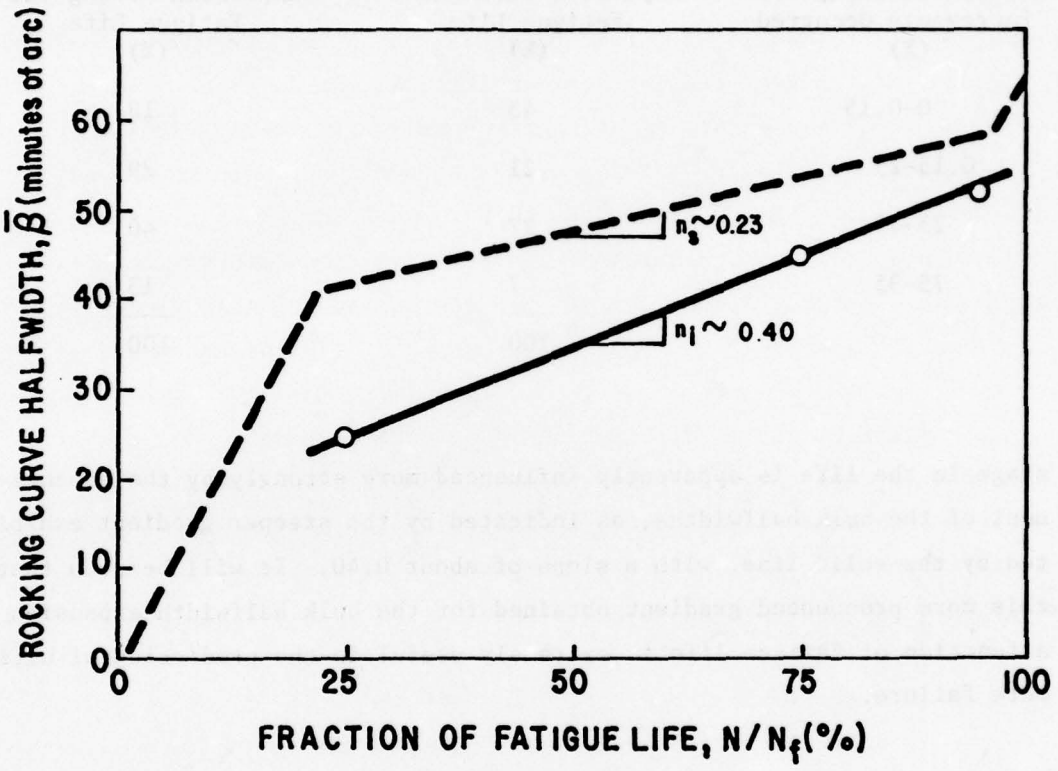


Figure 44. Comparative changes in surface (broken line) and bulk (solid line) halfwidths as a function of fatigue life. Note: Data are extracted from incremental fatigue and depth profile studies of Al 2024, batch A (Figures 23 and 37).

between the excess dislocation density of the surface compared to the bulk is gradually reduced when bulk plasticity is activated by stress intensification in the specimen interior. The stage is therefore set for the dynamic interplay between the surface and bulk on continued cycling. Failure can be linked to the point at which the defect densities of the bulk grains approach those for the surface grains. Viewed as a kind of chain reaction extending from the surface into the bulk, the stress concentrations imposed by localized defect accumulation ultimately exceed the surface barrier strength, causing microcracking at the surface. The argument is supported by the existence of a softer transition region similar to that found for single crystals, centered at about 75 μm in depth and separating the adjacent surface and bulk regions having considerably higher strain energy. The propagation of a crack from the surface into this region would quickly dispel its elastic energy, and additional cycling would be required to regenerate the stress condition for continued growth[114]

The grains located in this transition region, roughly three grain diameters in depth, reveal a substantial reduction in substructural fragmentation, in subdomain misorientation, and in nonuniform strain. The retention of this profile feature throughout the fatigue life must be interpreted in terms of the dynamic interaction of the rapidly hardened surface layer and the delayed plastic response of the bulk, combined with dislocation migration and redistribution effects facilitated by cyclic stress reversal. For polycrystalline metals, there need not be a long-range egression of dislocations from the region either toward the surface or into the bulk, since the grain boundaries represent an effective sink for excess dislocations and thus provide an ideal outlet for the halfwidth reduction in the individual grains. The rapid surface layer hardening and associated dislocation entanglement prevent such a response in surface grains, and long-range stresses emanate into and influence the eventual dislocation generation in interior grains. The complex stress distribution set up by push-pull cycling thus induces a narrow, transitional subsurface region with characteristically low strain energy, whether due to a local propensity for recovery and/or an unfavorable condition for defect generation. Again, the conclusion that

the halfwidth minimum is not due to the surface removal is evident from the observations that a plateau level above the minimum value is always measured after surface removal to greater depths. Thus, a distinction in substructural characteristics among the surface layer, transitional or subsurface region, and the bulk or core material must invariably exist.

There is good consistency among all the depth profiles with respect to the thickness of the hardened surface layer. For both single-crystal and polycrystalline materials, subjected to monotonic or fatigue deformation, the rocking curve width gradient extends universally to a depth of 100 to 150 μm. This typcial depth was also reported by Kramer[24,31] in his extensive investigations of the surface stresses generated by tensile and fatigue deformation. Taira and Hayashi[150] found the surface layer depth corresponded to at least one grain diameter and was independent of applied stress and stress concentration factor (for notched specimens). The combined studies involved specimen configurations ranging from flat plate-like shapes to cylindrical gage sections and cross-sectional area variations of almost thirty times. While experimental evaluation of the size effect on the surface barrier thickness and strength still needs attention, there appears to be little sensitivity in this regard. Viewed essentially as a "skin" or "layer" effect, the hardened free surface of the specimen can be thought of as a discontinuity at the extremity of the cross section, enclosing a core region of variable size but always featuring halfwidths consistent with the plateau value.

3. Instability of the Induced Defect Structure of the Bulk

Prima facie, the observation that the halfwidths increase in the bulk after cycling suggests that fatigue "damage" has occurred in the specimen interior. It might also be suspected that, after the removal of the surface layer, the excess dislocation density as indicated by β would increase with additional cycling.

In contrast to such expectations, however, it is well known[4,66] that the fatigue life of specimens can be prolonged indefinitely if appropriate amounts of metal are removed from the surface at various fatigue intervals. Improvement of fatigue failure resistance in single crystals has also been accomplished by continuous dissolution via an applied anodic current

during deformation[72,82]. Further, it has been shown that after, prolonged fatiguing and surface removal treatment, the fatigue life of the remaining metal was the same as for virgin specimens[104,105]

The x-ray diffraction results obtained for surface removal and recycling of previously fatigued specimens show that a reduction, rather than an increase, in the halfwidths is prompted by the treatment, as seen by reference to Figure 38. It may therefore be proposed that the excess dislocation arrangement in the interior, formed principally during the second stage of the original cycling, is very unstable without the presence of the hardened surface layer. Recalling the composite diagram constructed for the surface removal experiments, Figure 39, it is evident that, for a specimen recycled to 75%, surface layer elimination and recycling to 1.5% causes excess dislocation density reductions throughout the specimen cross section. The incomplete work hardening in the bulk allows a rapid recovery to defect concentrations characteristic of much earlier stages in fatigue life. The second depth profile (Figure 39c) obtained after treatment demonstrates the gradient conformation and excess dislocation density magnitudes typical of virgin specimens cycled to only 5% of the fatigue life. Experiments in which specimens previously cycled to 75% were recycled to failure after surface removal showed near complete restoration of the original fatigue resistance. A considerably prolonged lifetime can be achieved even for specimens subjected to prior fatigue totaling 95% by removing the hardened surface layer before continued cycling. The results indicate, however, that prior fatigue well into the stage II and final third stage produces diminishing returns with respect to fatigue life extension by surface treatment. At these advanced fractions of life, dislocation entanglement in the bulk finally begins to prevent the dislocation mobility required for rearrangement and recovery during recycling in the absence of the surface layer.* After a short

*As in annealing, the reduction in strain energy represented by the high dislocation density is the driving force for recovery, facilitated by the cyclic production of vacancies to enhance dislocation climb. However, as the degree of entanglement in the bulk increases as a result of prior cycling for longer and longer durations, after surface removal, the cyclic stress reversals of subsequent cycling become less capable of releasing the energy stored in the more stable, tightly knitted configurations, hence less recovery.

period of excess dislocation density decline, the magnitude of which depends on the degree of stability in the bulk attained during prior fatigue, all specimens suffer a regeneration of the surface barrier with continued cycling.

Based on this study, the improvements in fatigue failure resistance by intermittent surface removal are ascribed to the removal of the blocking defect structure produced in the surface layer. The life extension is not primarily ascribed, therefore, to the removal of PSB's or microcracks as proposed by Thompson[1,66], or to the blunting of these features as suggested by Hahn and Duquette[72,82]. Rather, it is presumed that, by eliminating the barrier either by actually polishing it away or by reducing its strength via a short-stress-relieving anneal, the interplay between the surface and bulk, by which real "damage" is generated, is effectively postponed. Alden and Backofen[4] proposed that these treatments prior to saturation hardening of single crystals retard the formation of widely spaced bands and prolong the period of random step emergence at the surface. They concluded, therefore, that the onset of "nonhardening" strain is delayed, and rather than representing a recovery or dissipation of damage, the treatment simply promotes homogeneous slip throughout the specimen and less slip concentration at the surface. The theory is similar to the microcrack elimination hypothesis in that it evokes a reduction in surface topographic relief to explain the life extension. The depth profiles after surface removal and recycling indicate to the contrary that a recovery mechanism is operative, and that it is activated in the bulk by the fatigue process itself when the restraint by the surface layer is eliminated. Thus, the apparent contradiction between the evidence of bulk damage provided by the depth profile plateaus, and the complete restoration of the fatigue life once the surface is removed, is resolved by the observed instability or reversibility of this damage engendered by the treatment.

The surface barrier model might also seem to be at variance to the improvement in fatigue performance achieved by prior surface treatments such as shot peening[107] or surface rolling[102,108]. Life extension by these deformative procedures, however, can be speculated to derive from the material "training" phenomenon proposed by Vitovec[103], whose

characterization of the in-depth defect distribution by differential etching rates bears an uncanny resemblance to the depth profiles generated by x-ray rocking curve analysis. His experiments showed that a limited degree of high-amplitude bending fatigue created a favorable predisposition of the material to resist the damage due to subsequent low-amplitude cycling. Much later, Kramer[106] reported an anomalous life extension for commercial alloys given an initial uniaxial straining or a limited number of high-amplitude reversed-stress cycles prior to lower amplitude fatigue (Figure 4b). The speculative proposal regarding such behavior is developed as follows.

The common element in all these treatments is the preferential production of high compressive residual stresses in the surface layers. Taira[116] measured the compressive stresses due to bending fatigue by x-ray methods and found them to be concentrated at the surface (Figure 6) and to increase in magnitude with the cyclic stress level. The prior imposition of significant residual stress impedes the subsequent motion of dislocations, thereby "reinforcing" the strength or resistance to plastic flow of grains oriented so as to be subject to the highest resolved shear stresses or located in the proximity of surface stress raisers. Taira also showed that the gradual decay of the residual stress after its early-life introduction can be associated with failure. The observation that $\sigma_r \rightarrow 0$ at crack initiation (Figure 5) implies that an initial provision of high residual stresses can delay this eventuality. On subsequent fatigue, the response will be more nearly elastic, and the generation and egression of dislocations from the bulk to form critical pileups at the surface will be suppressed. The slower development of surface debris effectively delays the microstructural response in the bulk, and thus the dynamic interplay leading to critical dislocation accumulation is further postponed.

In an annealed material, on the other hand, there is no doubt that the plastic resistance at the surface prior to cycling is initially lower than that in the specimen core.

On application of the load, say in the first half-cycle, the existence of intrinsic surface imperfections cause the state of stress to be the highest there which, combined with image force effects, represent an extremely favorable condition for both dislocation generation and motion. The subsequent entanglement causing the surface work hardening can also be perceived for the first half-cycle, and the barrier formation accelerates rapidly during the initial cycles. The process therefore elicits an earlier bulk response than occurs for metals given a prior surface treatment, and the critical fatigue damage accruement to initiate microcracks proceeds unchecked. It is to be emphasized that it is the introduction of compressive residual stresses, particularly in the surface layer, which prevents or at least delays this response. Thus, the behavior is distinguished from the general "bulk" softening response produced by cycling in uniformly cold worked specimens, which does not necessarily improve fatigue resistance or extend the life.

This hypothesis is also in accord with the dramatic improvement in the fatigue life afforded by a combination of prestraining and surface removal prior to fatigue[40]. The two-step treatment produces a cooperative effect of removing the surface barrier induced by the prior strain, while preserving the beneficial reinforcement aspect of deeper reaching residual stresses, and even facilitates some bulk recovery in the absence of the surface layer. Barrett's conclusion that the cold work introduced by cycling, and elucidated by surface x-ray analysis, may actually be beneficial rather than detrimental[139] takes on new meaning in light of the results from the in-depth x-ray study.

The concept might be extended to include other surface hardening procedures such as surface alloying, or solute hardening, and dispersion hardening as in the nitriding of steels. Even the residual compression induced by machining[102] during

metal component fabrication and surface preparation can be beneficial, provided the final topographic relief is limited.

It may be concluded that surface layer removal treatment can be employed in practice in the form of occasional surface polishing of metal components already in service, or used in conjunction with prestressing to improve the performance potential prior to actual use. The dramatic fatigue life extension such treatment engenders is not ascribed to the removal of microcracks, but rather to a combination of the strain relief due to substructural recovery in the absence of the surface barrier and the reinforcement of the resistance to microplasticity afforded by the compressive residual stresses.

4. Prediction of Fatigue Failure by X-ray Diffraction Analysis

For many years, x-ray diffraction patterns obtained from cyclically stressed alloys have failed to provide clear-cut indications of the impending onset of fatigue failure, nor could they be used to predict, even approximately, the span of the fatigue life[141-145]. Line broadening could be observed after cycling to a small fraction of the total fatigue life, but remained virtually unaltered both in extent and intensity throughout the remainder of the life[116,147,148].

The preliminary DCD investigation using copper radiation gave essentially the same result. Typical three-stage curves, relating the degree of an average grain's halfwidth expansion to the extent of fatigue cycling, were generated in all these experiments. When plotted as a function of the fraction of fatigue life, the results for different stress amplitudes reduced to a single curve. In addition, the data obtained for different grain sizes of the Al 2024 stock produced curves related by a simple Petch-type shift factor. As in previous attempts, however, the prediction of fatigue life at any point along the expansive second stage of the calibration curve was inhibited by the shallow slope characteristically obtained when copper radiation was used to analyze the specimen surface.

a. Prediction of Remaining Life on the Basis of the In-Depth Response. Closer inspection of the study dealing with x-ray analysis of the in-depth microstructural response revealed the emergence of a unique experimental capability to predict the amount of the fatigue life expended. Examination of Figure 44, constructed by plotting the data from the Al 2024 depth profiles as a function of fatigue life, indicates that the solid line representing the expansion in the specimen core gives a steep, nearly linear enhancement. This leads to the conclusion that a sampling of the substructural response from a depth different than that measured by copper radiation might produce a more reliable calibration curve. The use of chromium radiation, which penetrates no more than one grain in depth, obviously does not solve the predicament. Recalling the progressive fatigue curves shown in Figure 41, the slope of the second stage of the life is even less pronounced when the maximum penetration depth is only a few microns. In contrast, application of the penetrating molybdenum radiation, which also irradiates grains located deeper into the bulk of the specimen, gives rise to a straight line that has a sharp incline up to the critical value, β^*. The slope is sufficiently steep that with an accurate calibration curve the $\overline{\beta}$ value can be used to assign the proper fraction of life remaining to a specimen cycled an unknown extent.

The steep, almost single-stage curve results from the added contribution of the defect structure at greater depths to the x-ray analysis. This is revealed by Figure 45. Figure 45a shows the excess dislocation densities computed from the x-ray data obtained using copper and molybdenum radiation, plotted as a function of the fraction of fatigue life. These curves will be analyzed in conjunction with those drawn in Figure 45b. Each of the broken curves in Figure 45b represents the change during the life in the average $\overline{\beta}$ value taken over a particular depth from the surface in Figure 37. The curves were obtained by integrating the depth profiles to various depth limits and dividing the resultant areas by the depth distance to derive the average halfwidth for each layer thickness. These average halfwidths were then used to compute corresponding excess dislocation densities for comparison with the data in Figure 45a. It may be seen that the average $\overline{\rho}$ values for depths of 250, 350, and 1500 μm, corresponding to the beginning of the plateau region of the depth

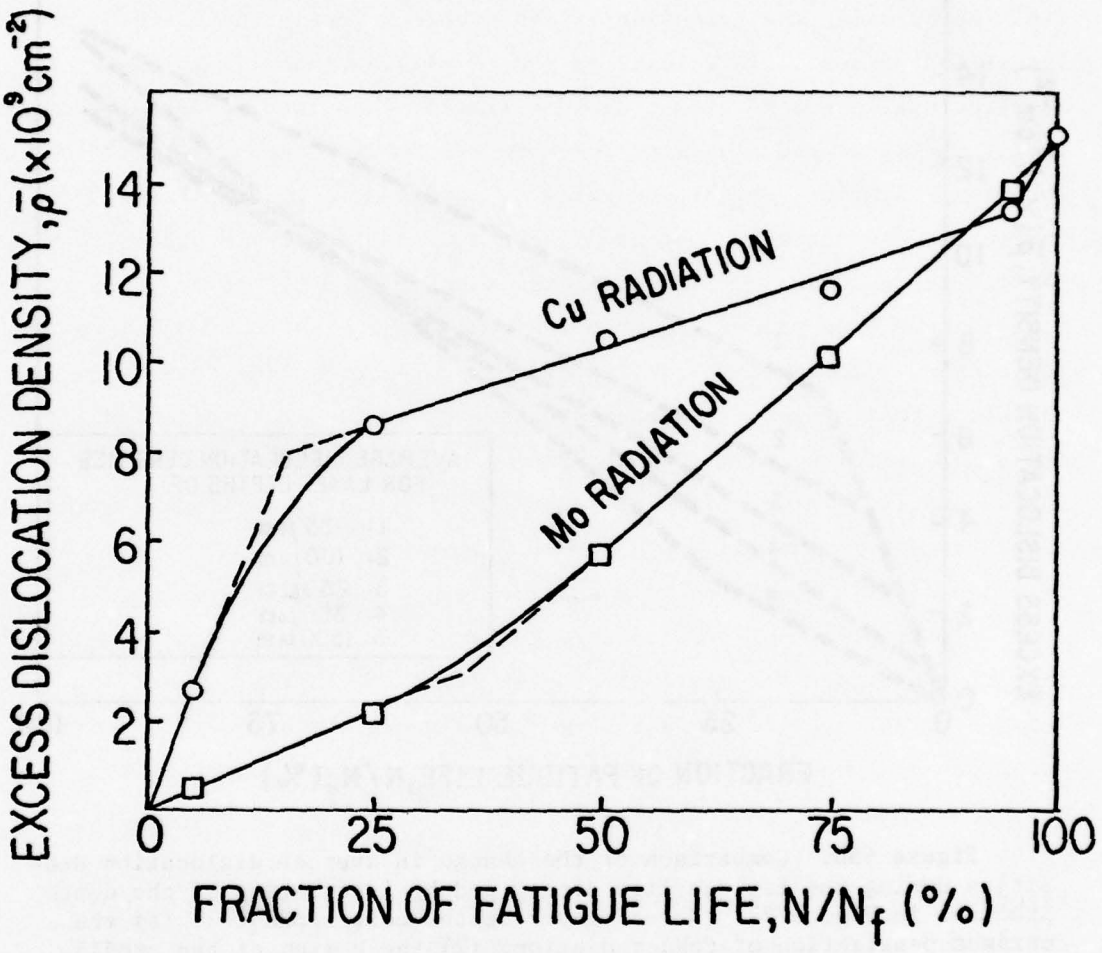


Figure 45a. Comparison of excess dislocation densities measured during the fatigue life by analysis with copper and molybdenum radiations

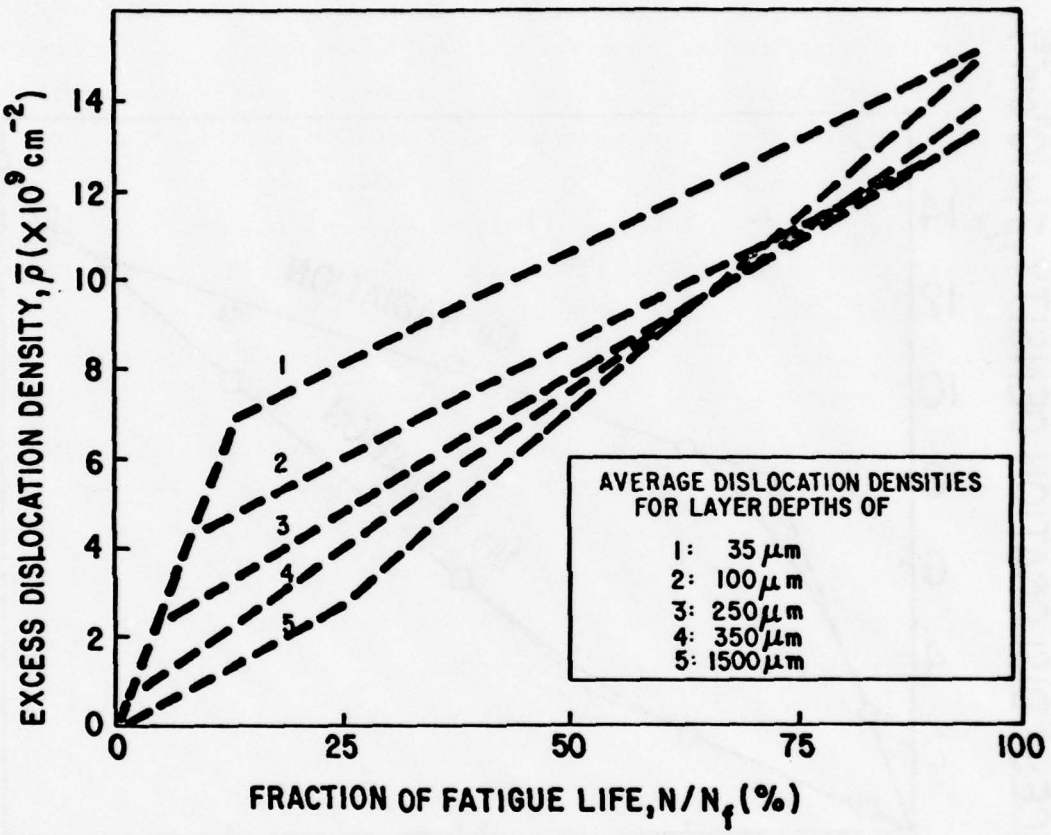


Figure 45b. Comparison of the change in average dislocation densities during the fatigue life determined by integration of the depth profiles in Figure 37. Note: Layer depths correspond to: (a) the maximum penetration of CuKα radiation, (2) the bottom of the profile well, (3) the beginning of the halfwidth plateau region, (4) the maximum penetration of MoKα radiation, and (5) one-half of the specimen diameter, or the specimen center.

profiles, the maximum penetration of Mo radiation, and the center of specimen, respectively, nearly coincide with the experimental curve obtained employing Mo radiation. The average $\bar{\rho}$ values computed from the depth profiles for lesser depths of 35 or 100 μm, which represent the maximum penetration of Cu radiation and the bottom of the profile "well," produce contrasting multistage curves which approximate the magnitude and slope of the experimental curve for the shallow-penetrating Cu radiation.

These studies make evident why, in the past, the x-ray patterns of cycled specimens have been inconclusive in predicting fatigue failure. For virtually the entire life, the rapidly work hardened surface layer belies the damage accumulating in the specimen. If the radiation does not penetrate beyond this surface layer, the slight increase in halfwidth or x-ray line broadening during the expansive second stage of the life falls within the experimental error limits shown in Figure 24. The rapid saturation hardening response of the surface layer therefore acts to both misrepresent and obscure the cyclic progression toward failure. The choice of an appropriate analysis depth, as represented by the thicker layer sampled with molybdenum radiation, however, can produce a much more sensitive broadening dependence on the cyclic extent, and therefore maximize the accuracy of the fatigue life prediction.

Thus, for analysis of a layer extending at least to a depth beyond the minimum of the profile well, or 200 μm, there is a linear dependence:

$$\beta = \beta^*(N/N_f), \qquad \text{(i)}$$

where β^* is the critical value for failure for both the Cu and Mo curves. From the previous study by Kramer[106,114] showing a Basquin-type relation involving the critical surface layer stress, σ_s^* Equation (9), p. 30, the correspondence between β^* and σ_s^* permits derivation of the expression:

$$\beta = (\beta^* N \sigma_a^P)/(\sigma_s^*/k) = \beta^* N \sigma_a^P/\alpha \qquad \text{(ii)}$$

b. Practical X-ray Diffraction Methods for Fatigue Life Prediction. In practice, the halfwidth values for the surface and bulk and for the surface layer alone can all be obtained in a single exposure sequence. Using MoKα radiation, the grain reflections can be recorded on multiple films separated by copper foils of appropriate thicknesses. The first film records the contribution of both surface and bulk, but the second and later films, owing to the suppression of the weak intensities by the interposed copper screen, register only the intense reflections emanating from the surface grains. Alternatively, due to the reflection geometry of the diffraction condition for the cylindrical specimens, i.e., incidence on the curved surface and variable takeoff angle for different reflections, the forward-directed reflections derive principally from the surface layer of about 150 μm in thickness, while the back reflections originate from greater depths up to 350 μm from the surface. This also facilitates the separation of surface and bulk contributions to the x-ray patterns. Finally, a rigidly collimated primary beam from a dual x-ray target, producing both copper and molybdenum radiation, could be employed to obtain an equivalent sampling in the respective Debye patterns of halfwidths from the surface layer and surface and bulk combined. For all these methods, the difference between the average halfwidth for the rapidly work hardened surface layer alone, which approximates β^*, and that for the combined surface and bulk regions may be used to quickly deduce the remaining fatigue life. This exploitation of the convergence of the two curves at the late fractions of the life avoids the tedious generation of numerous calibration curves and failure prediction can be accomplished simply, accurately, and nondestructively.

VI. CONCLUSIONS

A. IMPLICATIONS OF SURFACE WORK HARDENING: THE SURFACE BARRIER CONCEPT

The first two phases of the investigation were designed to characterize the deformation response for tensile and fatigue stressing as a function of the depth into the bulk from the free surface. Direct examination of the deformation induced substructural misorientation and measurement of the defect concentration and distribution by x-ray diffraction methods led to the following conclusions.

1. Monotonic deformation of single crystals belonging to "model" species inevitably produces preferential work hardening in the surface layer as compared to the bulk material.

   a. For silicon crystals pulled at elevated temperature, and plastically strained aluminum crystals, the work hardened surface layer is described quantitatively by a decreasing gradient in excess dislocation density from surface to bulk.

   b. Qualitatively, the deformation induced surface layer comprises a highly misoriented subdomain debris, in comparison to the polygonization-type substructure in the interior, exhibiting considerably less microplasticity.

   c. The experimental evidence suggests that the surface layer work hardening rate is greater than in the specimen core due to preferential generation, multiplication, and interaction of dislocations at the free surface.

   d. The similar gradient obtained for tensile-deformed gold monocrystals indicates that the preferential work hardening of the surface layer does not depend on the formation of a surface oxide layer or film.

2. A special propensity for surface layer work hardening is also measured for aluminum single crystals and Al 2024 alloy specimens subjected to fatigue cycling.

   a. The work hardening of grains located at the surface of alloy specimens displays a three-stage response sequence during the fatigue life:

      (1) Stage I constitutes the first 20 to 25% of the life and features a rapid hardening response at the surface.

(2) Stage II represents a transient period extending to 90 to 95% of the life, during which the surface excess dislocation density exhibits a saturated condition, increasing only very slightly.

(3) Stage III is characterized by another rapid hardening response in the surface layer prior to fracture, concomitant with slip band intrusion and extrusion and incipient microcracking at the alloy surfaces. A critical excess dislocation density is measured at ultimate failure.

b. For the aluminum alloy, the increase in excess dislocation density at the surface as a function of the fraction of fatigue life and the critical value at failure are independent of the stress amplitude. Differences in the cyclically induced increases in excess dislocation density for alloys with various grain sizes are related by a power-law shift factor.

3. When sufficiently high stress amplitudes are applied in the fatigue tests, a plastic response in the bulk of alloy specimens is observed, as evidenced by an increase in the density of excess dislocations of one sign in the core region.

a. Significant microstructural change is incurred in the bulk of specimens cycled beyond about 5% of their life. The defect distribution with depth is consistently characterized by a decreasing excess dislocation gradient from the surface to a minimum at about 100 μm into depth, followed by an increase again to a constant plateau level at a distance of about 200 μm into the bulk.

b. Elucidation of the bulk substructure, by incrementally polishing away the surface layers and analyzing the x-ray rocking curves for each depth, indicates that the bulk "damage" is sustained gradually throughout the life. The preferentially hardened surface layer is proposed to constitute a barrier to moving dislocations. Long-range stresses due to surface dislocation accumulation and pileups emanate into the bulk and initiate the plastic response in the core material. The fatigue behavior can thus be visualized as a dynamic interplay between the surface and bulk regions.

c. Single crystals cycled at stress amplitudes below their endurance limit, while suffering the usual hardening at the surface, incur little or no bulk damage. The subsurface layer centered at 100 μm in depth exhibits

a propensity for recovery, possibly by dislocation migration or redistribution toward the surface, producing a lower excess dislocation density in this region than is intrinsic to the virgin crystal. The negligible introduction of bulk damage at low cyclic stress levels explains why the life span can extend almost indefinitely despite the obvious cold work and hardening induced in the surface layer.

4. The bulk substructure induced by fatigue is extremely unstable upon surface removal and recycling.

a. Previously cycled alloy specimens display a rapid decline in subdomain misorientations and excess dislocation density toward the values intrinsic to virgin specimens when recycled after removal of the originally fatigue hardened surface layer. Specimens precycled up to 75% of their life experience nearly complete regeneration of their full life spans when so treated. Precycling beyond 75% followed by surface removal gives diminishing returns with respect to fatigue life extension.

b. The reversal of bulk damage or recovery phenomenon, resulting from dislocation rearrangement and egression in the absence of the surface barrier, explains the prolonged fatigue lives obtained by continuous or intermittent surface dissolution during the cycling process. The improved fatigue resistance is thus ascribed primarily to the elimination of the blocking action afforded by the surface layer, rather than to the removal of microcracks and other topographic surface relief.

B. IMPORTANCE IN METAL FATIGUE: THE PREDICTION OF FATIGUE FAILURE

The third and final phase of the experimental program was oriented toward exploitation of the practical significance of the in-depth studies. Elucidation of the resultant substructures of the surface and bulk regions of cycled specimens and their dynamic interplay during the fatigue process led to the following conclusions regarding the prediction of fatigue life and failure.

1. Application of shallow-penetrating copper radiation in the x-ray diffraction analysis establishes, for both single crystals and polycrystalline alloys, a long intermediate stage of the fatigue life during which little change can be detected in the saturation level of the surface excess dislocation density. Curves representing the rocking curve

halfwidth expansion, related to the degree of induced lattice misorientation, as a function of the fraction of fatigue life show an exceedingly gradual positive slope during this period. This shallow inclination greatly inhibits proper assignment of the remaining fatigue life for a specimen which has surface halfwidths that fall within the narrow range of magnitude for this portion of the curve. This result explains the inability of previous studies to predict the fatigue life on the basis of x-ray line broadening.

2. The in-depth analysis discloses a steeper single-stage dependence of rocking curve halfwidths of the bulk as a function of the fraction of fatigue life. Integration of the "depth profiles" to obtain the average halfwidth dependence on distance from the surface for incremental fractions of life also results in a single-stage, linear dependence when the average halfwidths are computed for layers of at least 250 μm in depth. A multistage dependence is obtained for shallower layer depths. It is therefore evident that analysis which includes in the measured response to cycling the contribution from greater depths from the surface will result in a more favorable curve for fatigue life prediction.

3. By employing penetrating molybdenum radiation, for which grains located up to 300 to 400 μm in depth contribute to the x-ray pattern, a nearly linear dependence of the average rocking curve breadths on the number of cycles is obtained nondestructively. The concomitant slope enhancement in the cyclic progression toward the critical halfwidth, β^*, for the curves is regarded to be of great practical significance in improving the predictive accuracy for x-ray analysis. The convergence of the progressive fatigue curves for shallow and deeply penetrating radiations to an identical β^* value eliminates the need for numerous calibration curves for fatigue failure prediction. Instead, by sampling the rocking curve widths for the surface and bulk regions independently using x-ray radiation with different wavelengths, or by separating the reflections from the surface and bulk on the basis of relative intensity employing a single penetrating radiation, the comparative halfwidths can be utilized to estimate accurately the expended fatigue life. This simple, nondestructive x-ray diffraction technique for fatigue life prediction evokes a new criterion for cyclically induced failure related not just to the surface damage but to the in-depth response as well.

VII. SUGGESTIONS FOR FUTURE WORK

The primary emphasis of the research program thus far, as born out by the conclusions in the preceding section, was to confirm the preferential hardening in the surface layer during deformation, elucidate the in-depth response, and characterize the progressive accruement of fatigue damage to enhance the capability for failure prediction. The investigation was restricted to a single fatigue mode, namely push-pull, constant amplitude cycling, and the x-ray diffraction analysis was carried out using the sensitive and time-consuming double-crystal diffractometer technique, applicable only under controlled laboratory conditions. Continuing research, therefore, should concentrate on broadening the prediction capability to include a variety of fatigue modes and specimen shapes, sizes, materials, and preparations, as well as on refinement of the experimental analysis for practical and efficient use in the field.

The following list presents a number of suggestions for future work which emerged in the course of the project.

1. Related to elucidation of the surface and bulk deformation response:

   a. Characterization of the work hardening rates, i.e., relative strain hardening exponents for the surface and bulk during plastic deformation in simple tension.

   b. Confirmation as to whether cycling at or below the endurance limit is associated with the absence of damage accrued in the bulk.

   c. Further elucidation of the dislocation density and configuration in the surface and bulk by TEM methods.

   d. Determination of the effect of aggressive environments on progressive surface hardening and its critical value, as in corrosion fatigue.

2. Related to incremental fatigue studies and fatigue life prediction:

   a. Extension of the in-depth and incremental fatigue studies to include additional alloys, grain sizes, degrees of prior cold work, aging treatments, etc.

b. Evaluation of the effects related to specimen size and shape, and to nonideal surface conditions that are inherent to as-machined specimens, on the prediction capability.

c. Comparison of the microstructural response for a variety of fatigue modes and loading configurations such as constant strain-control cycling, nonzero mean stress fatigue, bending fatigue, and variable amplitude cycling.

3. Related to improvement and simplification of the x-ray analysis:

a. Experimentation with a dual target producing both shallow and deeply penetrating radiation.

b. Investigation of the potential for prediction of small grain size metal failure employing traditional line broadening analysis but with deeply penetrating radiation.

c. Adaptation of the double crystal diffractometer for use in the field by application of position-sensitive detectors.

APPENDIX A

DEPTH OF PENETRATION*

Let γ_o and γ_1 represent the angles between the tangent to the specimen surface at any point of incidence, and the primary and reflected beams, respectively. Then the entrance distance, ℓ_o, and the exit diatance, ℓ_1, can be expressed as $x/\sin\gamma_o$ and $x/\sin\gamma_1$, where x is the depth measured in a direction normal to the surface. The reflected intensity is thus given by:

$$I_R = I_R' \exp\left[-\mu x\left(\frac{1}{\sin\gamma_o} + \frac{1}{\sin\gamma_1}\right)\right] \qquad \text{(i)}$$

where I_R' is the reflected intensity when there is no absorption. Setting $\gamma_o = \phi$ and $\gamma_1 = 2\theta - \phi$, for a reflected intensity ratio 1/e, the penetration distance normal to the specimen surface is given by:

$$x = \frac{1}{\mu}\left(\frac{1}{\sin\phi} + \frac{1}{\sin(2\theta-\phi)}\right)^{-1} = \frac{1}{\mu}\left(\frac{\sin\phi\sin(2\theta-\phi)}{\sin(2\theta-\phi)+\sin\theta}\right) \qquad \text{(ii)}$$

1. Tension studies

For the planar single crystals of Si, Al, and Au, the relative penetration distances are:

Silicon: (112) surface orientation, symmetric case,
($\gamma_o = \gamma_1 = \phi = \theta$), x = 24.6 μm

Aluminum: (100) surface orientation, symmetric case,
x = 14.5 μm

Gold: (113) reflection, asymmetric case,
($\gamma_o = \phi = \theta + 11^o$, $\gamma_1 = 2\theta - \phi$),
x = 0.7 μm

for analysis with copper radiation.

---

*See B.D. Cullity, Elements of X-ray Diffraction, Addison-Wesley, Reading, Mass., 1956, pp. 188-89.

2. Fatigue study of aluminum single crystals

The cylindrical specimens were mounted on the goniometer head and translated so as to achieve a glancing incidence of the x-ray beam on the specimen surface. In this way the axis of rotation was positioned to lie in the plane of reflection, and the tendency for precession about the axis was minimized. For the (100) reflection in the parallel setting, the penetration varied from zero [when $\phi = 0^{o}$ and $44.74^{o}(2\theta)$] to 7.25 μm [when $\phi = 22.37\ (\theta)$]. The former condition applied at the extreme right side of the beam width, and the latter approximated the penetration at the left margin of the beam, as illustrated by curve II in Figure A1.

3. Variable penetration studies of Al 2024 alloy

As was true for the single crystals, the penetration into the alloy specimens varied with the incidence position along the curved surfaces, due due to the continuous change in incidence and takeoff angles. The radiation penetration capability was also dependent on the reflection condition for the randomly oriented grains so that the takeoff angle was a function of both position and reflection order. To characterize the distribution of penetration depths, which were inherent to the analysis with each type of x-ray radiation, three representative cases were considered:

Case I: If only reflections normal to the surface tangent are considered, $2\theta = \phi + 90^{o}$, and

$$x = \frac{1}{\mu}\left(\frac{\sin\phi}{1 + \sin\phi}\right) = \frac{1}{\mu}(1 + \csc\phi)^{-1}$$

Case II: If only symmetric reflections ($\gamma_o = \gamma_1$) are considered, $2\theta = 2\phi$, and

$$x = \frac{1}{\mu}\left(\frac{\sin^2\phi}{2\sin\phi}\right)\ \frac{1}{2\mu}\ \sin\phi$$

Case III: If only the reflections $2\theta = 90^{o}$ are considered,

$$x = \frac{1}{\mu}\left(\frac{\sin\phi\cos\phi}{\sin\phi+\cos\phi}\right)$$

The maximum radial penetrations for each radiation type under these conditions are given in Table A1 and illustrated in Figure A1.

TABLE A1 - MAXIMUM RADIAL PENETRATIONS OF MOLYBDENUM, COPPER, AND CHROMIUM RADIATIONS FOR CYCLINDRICAL A1 2024 SPECIMENS

Angle ϕ Between S$_o$ and Surface Tangent	Maximum Radial Penetration into Surface Layer (μm)								
	MoKα: 1/μ=718			CuKα: 1/μ=76.2			CrKα: 1/μ=24.4		
	I	II	III	I	II	III	I	II	III
70°/ Represents Extreme Left Margin of the Beam Width	348	337	180	36.9	35.8	19.1	11.8	11.5	6.1
45°/Represents Nearly the Midpoint of the Beam Width	297	254	254	31.6	26.9	26.9	10.1	8.6	8.6
20°/Represents Right-Hand Portion of the Beam Width	183	123	180	19.4	13.0	19.1	6.2	4.2	6.1

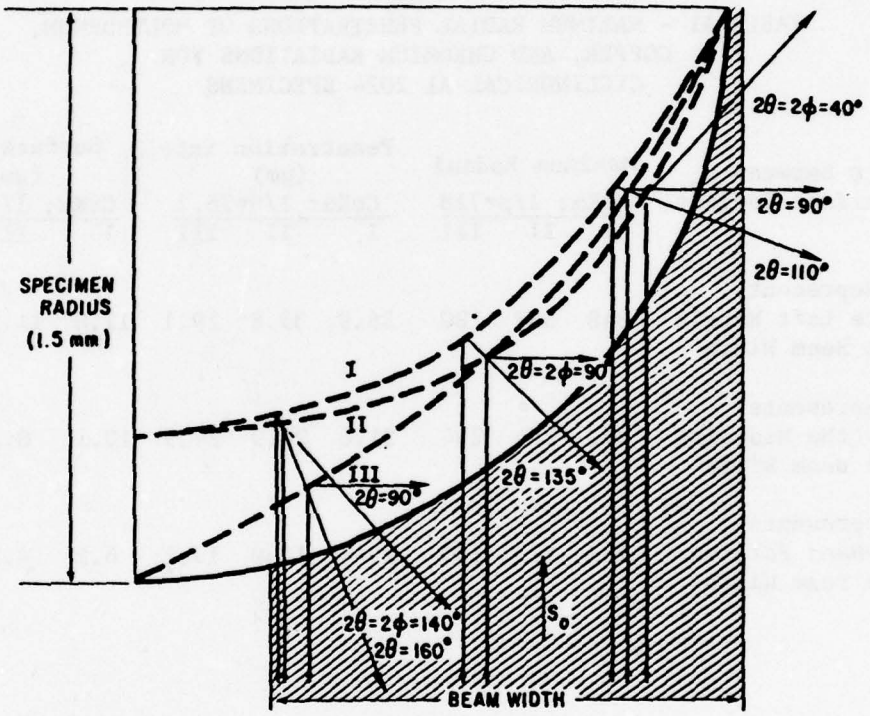


Figure A1. Schematic diagram of radial penetrations for molybdenum, copper, and chromium radiations

APPENDIX B

HORIZONTAL AND AZIMUTHAL BROADENING

This section presents the mathematical formulations used to correct for the instrumental broadening inherent to the horizontal breadth of a spot array in the Debye pattern, and to calculate the width of the marginal distribution along the direction parallel to the rotation axis or azimuthal breadth.

1. Velocity factor and vertical divergence corrections*

Let ψ be the latitude of the reflection measured from the equatorial plane, and ϕ be the longitude measured from the x-axis of the reflecting zone.

Let ε be the angle measured from the center of a unit sphere along a circle of latitude, subtended by a region of the sphere pierced by the misaligned normals of the crystallite.

Then $\Delta\phi_1 = \varepsilon/\cos\psi$ is the angle required to turn this region past a fixed longitude (the velocity correction).

Let $\Delta\phi_2$ be the angle required to turn any point of the region of misalignment through the reflecting zone.

Then $\Delta\phi_2 = \left[K\sin\psi/(\cos^2\psi - \sin^2\theta)^{1/2}\right] + L$, where K is the vertical convergence of the incident beam and L is the horizontal convergence.

The angle of misalignment, ε, in terms of the total angle $\Delta\phi$ through which the reflection is observed is then:

$$\varepsilon = \Delta\phi\cos\psi - \left[\frac{K\sin\psi}{(\cos^2\psi - \sin^2\theta)^{1/2}} + L\right]\cos\psi \qquad \text{(i)}$$

At the equator, $\psi = 0^\circ$, thus $\varepsilon = \Delta\phi - L$.

---

*See A.J. Reis, J.J. Slade, Jr., and S. Weissmann, J. Appl. Phys. 22, 665 (1951), or photometric transformation method by J.J. Slade, Jr., and S. Weissmann, J. Appl. Phys. 23, 323 (1952).

At higher azimuths, the reflection boundaries are ill-defined and correction of the misalignment angle is required. To simplify the calculation, set $\varepsilon = \beta'\cos\psi - Q$, where $Q = 0.67\left[\frac{k\sin\psi}{(\cos^2\psi - \sin^2\theta)^{1/2}} + L\right]\cos\psi$ is the correction factor due to the vertical divergence for the measured halfwidth β'. Now, defining an angle ψ_1, such that $\tan\psi_1 = Y/R$, where Y is the vertical distance of the reflection from the equatorial plane, or line on the film, and R is the radius of the camera, then $\sin\psi_1 = \frac{Y/R}{\left[1+(Y/R)^2\right]^{1/2}}$. Also, since $\sin\psi_1 = 2\sin\theta\sin\psi$, the angle ψ can be expressed directly in terms of the camera parameters so that:

$$\sin\psi = \frac{Y/R}{2\sin\theta\left[1+(Y/R)^2\right]^{1/2}} \qquad \text{(ii)}$$

If the latitude, ψ, is limited to 12°, which corresponds to an angle of about $\pm 15^\circ$ measured with respect to the equatorial line on the film from the point of primary beam incidence, the error due to the vertical divergence for the present investigation varies from 2.2 minutes of arc for the (111) reflection to 4.3 minutes for the (420) reflection. The velocity factor contributes from 1.0 to 1.75 minutes to the breadth of reflections at the azimuthal limit for the respective minimum and maximum halfwidths encountered in this study.

2. Computation of azimuthal breadth*

The vertical marginal distribution of lattice misalignment, is calculated by differentiating equation (ii) above:

$$\psi\Delta\psi = \frac{1}{2\sin\theta}\left\{\frac{1/R}{\left[1+(Y/R)^2\right]^{1/2}} - \frac{Y^2/R^3}{\left[1+(Y/R)^2\right]^{3/2}}\right\}dy, \qquad \text{(iii)}$$

*See S. Weissmann and D. Evans, Acta Cryst. 7, 733 (1954).

$$\Delta\psi = \frac{dY}{Y\left[1+(Y/R)^2\right]} \tan\psi. \qquad \text{(iv)}$$

Thus, for reflections near the equator where $\cos\psi \sim 1$, the azimuthal broadening may be calculated simply by measuring the vertical spread of the spot on the film, dY, less the size of the grain and substituting into $\Delta\psi = \frac{dY}{2\sin\theta R}$.

APPENDIX C

DEYBE PATTERN AND ROCKING CURVE ANALYSIS

This section presents several aspects of the DCD Debye pattern generation and analysis procedure, and a formulation for separating the contributions of internal strain and misorientation to the constituent arrays or rocking curves.

1. Choice of monochromator

In order to minimize the required exposure time or maximize the intensity to allow multiple film exposure, the choice of monochromator for each particular radiation type is determined by the comparative intensity ratios in Table C1.

TABLE C1 - COMPARATIVE INTENSITY RATIOS FOR VARIOUS RADIATION AND MONOCHROMATOR COMBINATIONS

Single-Crystal Monochromator	ρ (g/cm^3)	$\bar{f}_a$ (Taking $\sin\theta/\lambda = 0.159$)	Cu; λ=1.5418Å		Mo; λ= 0.7107		Cr; λ=2.2909	
			$\theta_{(111)}$	$\mu_\ell (cm^{-1})$	$\theta_{(111)}$	μ_ℓ	$\theta_{(111)}$	$\mu\ell$
Silicon	2.33	10.69	14.22	141.1	6.50	15.01	21.40	440.4
Germanium	5.32	27.40	13.65	402.2	6.25	344.7	20.53	1250.
$\frac{(I_m)_{Si}}{(I_m)_{Ge}} \alpha \frac{(f_a^2/2\mu)_{Si}}{(f_a^2/2\mu)_{Ge}}$			0.43		3.50		0.42	

2. Estimation of reflecting grain population

The sample of spot arrays will vary in size for the radiation types as follows:

a. Cu vs Cr:

Ratio of number of Debye arcs recorded, 4/9

Weighting correction for multiplicity, 50/74

Ratio of respective penetration distances, 1/3

Total difference in number of observed reflections, 10:1

b. Cu vs Mo:

Same number of recorded arcs and multiplicity factor

Ratio of penetration distances, 10/1

Ratio of number of crystallites oriented for reflection, 2.5/1 ($N_r^{\cdot} = 2\pi N\alpha\cos\theta/\sin 2\theta \approx k/\sin\theta$)

Total difference in number of observed reflections, 1:25

Table C2 is a partial compilation of the data used in the comparison.

TABLE C2 - X-RAY DIFFRACTION DATA FOR ALUMINUM USING COPPER, MOLYBDENUM, AND CHROMIUM RADIATIONS

Reflection Index (Aluminum)	Relative Intensity* ($CuK\alpha_1$)	Multiplicity	Reflection angle, 2θ (a_o = 4.0494)		
			$CuK\alpha$	$MoK\alpha$	$CrK\alpha$
111	100	8	35.51°	17.48	58.65
200	47	6	44.75	20.22	68.88
220	22	12	65.16	28.74	106.21
311	24	24	78.31	33.84	139.37
222	7	8	82.52	35.39	
400	2	6	99.19	41.10	
331	8	24	112.16	44.98	
420	8	24	116.72	46.21	
422	8	24	137.70	50.92	

*Taken from File Card #4-0787, International Centre for Diffraction Data (JCPDS), Swarthmore, Pa.

3. Separation of broadening contributions to the radial breadth*

The corrected halfwidth of the horizontal range of reflection is composed of the broadening due to the internal strain or misalignment, β_{is}, of the individual subdomains and that caused by their mutual misorientation, β_{ms}, such that:

$$\beta_T = (\beta_{is}^2 + \beta_{ms}^2)^{\frac{1}{2}} \qquad \text{(i)}$$

*See S. Weissman and D. Evans, Acta Crys. 7, 733 (1954).

where β_T is related to a Gaussian distribution of strained subdomains by

$$\beta_T = 2.36\varepsilon = 2.36(S_{is}^2 + S_{ms}^2)^{\frac{1}{2}} . \qquad \text{(ii)}$$

For a well-resolved, multipeaked rocking curve, or physical deconvolution by topographic techniques, the moment method allows computation of the individual components.

First, the integrated intensity is recorded for each rotational position of the specimen, ϕ. The first moments, $\overline{\phi}$, of each peak of the array or rocking curve are used to calculate β_{ms}, such that:

$$\overline{\phi}_1 = \Sigma I_i \phi_i / \Sigma I, \; \overline{\phi}_2 = \Sigma I_j \phi_j / \Sigma I, \text{ etc., and}$$

$$\beta_{ms} = (\overline{\phi}_1 - \overline{\phi}_2) \times \Delta\phi, \qquad \text{(iii)}$$

where $\Delta\phi$ is the shift angle between rotation positions.

The first and second moments, $\overline{\phi^2}$, are used in the calculation of the misalignment within the individual subdomains, β_{is}, such that:

$$\overline{\phi_1^2} = \Sigma I_i \phi_i^2 / \Sigma I, \text{ and } \overline{\phi_2^2} = \Sigma I_j \phi_j^2 / \Sigma I,$$

and thus:

$$(\beta_{is})_1 = [\overline{\phi_1^2} - (\overline{\phi_1})^2]^{\frac{1}{2}} \times \Delta\phi \text{ , and}$$

$$(\beta_{is})_2 = [\overline{\phi_2^2} - (\overline{\phi_2})^2]^{\frac{1}{2}} \times \Delta\phi. \qquad \text{(iv)}$$

REFERENCES

1. N. Thompson, Fracture, John Wiley and Sons, New York, 1959, pp. 354ff.
2. P. J. E. Forsyth and C. A. Stubbington, J. Inst. Metals 85, 339 (1956-57).
3. A. H. Cottrell and D. Hull, Proc. Roy. Soc. 242, 211 (1957).
4. T. H. Alden and W. A. Backofen, Acta Met. 9, 352 (1961).
5. N. Thompson and N. J. Wadsworth, Adv. in Phys. 7, 72 (1958).
6. J. C. Grosskreutz, J. Appl. Phys. 34, 372 (1963).
7. J. T. McGrath and W. J. Bratina, Phil. Mag. 11, 429 (1965).
8. C. E. Feltner and C. Laird, Acta Met. 15, 1633 (1967).
9. W. J. Plumbridge and D. A. Ryder, Met. Rev. 136, 119 (1969).
10. R. L. Segall, P. G. Partridge, and P. B. Hirsch, Phil. Mag. 6, 1493 (1961)
11. J. T. McGrath and G. W. J. Waldron, Phil. Mag. 9, 249 (1964).
12. M. Klesnil and P. Lukáš, J. Iron and Steel Inst. 203, 1043 (1965).
13. E. E. Laufer and W. N. Roberts, Phil. Mag. 14, 65 (1966).
14. E. Levine and S. Weissmann, Trans. Quar. Am. Soc. Metals 61, 128 (1968).
15. J. C. Grosskreutz, Met. Trans. 3, 1255 (1972).
16. J. C. Grosskreutz, 3rd Int. Congr. on Fracture, Munich, Germany (Apr 8-13, 1973).
17. P. A. Rehbinder, Bull. Acad. Sci. URSS, Classe Sci. Chim. 639 (1936).
18. I. R. Kramer, Fundamental Phenomena in Material Sciences, Vol. 3, "Surface Phenomena," Plenum Press, 1966, pp. 171-93.
19. H. Mughrabi, Phys. Stat. Sol. 39, 317 (1970).
20. H. Mughrabi, Phys. Stat. Sol. B44, 391 (1971).
21. J. T. Fourie, Can. J. Phys. 45, 777 (1967).
22. J. T. Fourie, Phil. Mag. 17, 735 (1968).
23. T. Tabata and H. Fujita, J. Phys. Soc. Jap. 32, 1536 (1972).
24. I. R. Kramer, TMS-AIME 233, 1462 (1965).
25. S. Kitajama, "Study of Yielding and Easy Glide Deformation of Highly Perfect Cu Crystals by Using Etch Pit Techniques," Nato Conference cited (Sep 1975).
26. S. Kitajama, H. Tanaka, and H. Kaieda, Trans. J.I.M. 10, 10 (1969).
27. I. R. Kramer and N. Balasubramanian, Acta Met. 21, 695 (1973).
28. K. Sumino and M. Yamamoto, Phys. Soc. Jap. 16, 131 (1961).
29. I. R. Kramer and L. J. Demer, TMS-AIME 221, 780 (1961).

30. I. R. Kramer, TMS-AIME 227, 1003 (1963).
31. I. R. Kramer, TMS-AIME 227, 529 (1963).
32. T. P. Hoar, Corrosion Science 7, 341 (1967).
33. J. T. Fourie, Proc. 4th Int. Conf. on Strength of Metals and Alloys, Nancy, France, 922 (1976).
34. W. T. Brydges, Scripts Met. 2, 557 (1968).
35. I. R. Kramer, discussion of "The Soft Surface Effect in Plastic Deformation and Fatigue of Metals and Alloys," by J. T. Fourie, Corrosion Fatigue, NACE-2, Houston, Tex., 173 (1972).
36. C. Feng and I. R. Kramer, TMS-AIME 233, 1467 (1965).
37. G. Vellaikal and J. Washburn, J. Appl. Phys. 40, 2280 (1969).
38. K. Kolb and E. Macherauch, Phil. Mag. 7, 415 (1962).
39. I. R. Kramer, TMS-AIME 230, 991 (1964)
40. I. R. Kramer, Trans. ASM 62, 521 (1969).
41. R. M. Latanision and R. W. Staehle, Scripta Met. 2, 667 (1968).
42. J. C. Fischer, Trans. AIME 194, 531 (1952).
43. K. Sumino, Phys. Soc. Japan 17, 454 (1962).
44. V. P. Alekhin, O. V. Gusev, V. I. Trefilov, and H. K. Shorshorov, Dokl. Akad. Nauk. SSSR 188, 548 (1969).
45. L. S. Milevskii and I. L. Smol'skii, Sov. Phys. Sol. St. 17, 860 (1975).
46. J. P. Hirth, "The Influence of Surface Structure in Dislocation Nucleation," Tech. Report #2, RF Proj. No. 1386, ONR Contract #495 (26), Ohio St. Univ., Columbus, Ohio (Sep 1962).
47. I. P. Kushnir and E. F. Sidokhin, Sov. Phys. Sol. St. 16, 907 (1974).
48. L. G. Orlov, Sov. Phys. Sol. St. 9, 1836 (1968).
49. J. C. M. Li, J. Aust. Inst. Met. 8, 206 (1963).
50. A. A. Alekseev, S. B. Goryachev, and B. M. Strunin, Sov. Phys. Sol. St. 16, 2310 (1975).
51. R. L. Fleischer, Acta Met. 8, 598 (1960).
52. M. G. Gol'diner, Sov. Phys. Sol. St. 17, 406 (1975).
53. R. L. Fleischer, Acta Met. 8, 32 (1960).
54. D. J. Duquette, Scripta Met. 3, 513 (1969).
55. C. S. Barrett, Acta Met. 1, 2 (1953).
56. R. M. Latanision and R. W. Staehle, Acta Met. 17, 307 (1969).

57. J. Takamura, Mem. Fac. Eng. Kyoto Univ. 18, 255 (1956).
58. M. A. Adams, Acta Met. 6, 327 (1958).
59. B. Chalmers and R. S. Davis, Dislocations and Mechanical Properties of Crystals, John Wiley and Sons, New York, 1957, p. 232.
60. P. A. Rehbinder and E. K. Wenstrom, Byul. Akad. Nauk. SSSR, Classe Sci. Mat. Nat. Ser. Phys. 531 (1937).
61. S. Harper and A. H. Cottrell, Proc. Phys. Soc. (London) B63, 331 (1950).
62. I. R. Kramer, TMS-AIME 221, 989 (1961).
63. I. R. Kramer and C. L. Haehner, Acta Met. 15, 199 (1967).
64. I. R. Kramer, TMS-AIME 239, 1754 (1967).
65. I. R. Kramer, Environment-Sensitive Mechanical Behavior, Gordon and Breach, New York, 1965, pp. 127-46.
66. N. Thompson, N. J. Wadsworth, and N. Louat, Phil. Mag. 1, 113 (1956).
67. J. C. Grosskreutz, ASTM STP 495, 5 (1971).
68. W. A. Wood, ASTM Symposium on Basic Mechanisms in Fatigue, 110 (1959).
69. W. A. Wood and R. L. Segall, Bull. Inst. Metals 3, 160 (1957).
70. J. T. McGrath and R. C. A. Thurston, Trans. AIME 227, 645 (1963).
71. P. B. Hirsch, P. G. Partridge, and R. L. Segall, Phil. Mag. 4, 721 (1959).
72. H. Hahn and D. J. Duquette, Proc. 4th Int. Conf. on Strengths of Metals and Alloys, Nancy, France, 916 (1976).
73. P. Lukáš and M. Klesnil, Phys. Stat. Sol. 37, 833 (1970).
74. H. D. Nine, J. Appl. Phys. 38, 1678 (1967).
75. H. D. Nine and D. Kulmann-Wilsdorf, Can. J. Phys. 45, 865 (1967).
76. D. S. Kemsley, Phil. Mag. 2, 131 (1957).
77. D. S. Kemsley, J. Inst. Met. 85, 153 (1956-57).
78. C. Laird and G. C. Smith, Phil. Mag. 8, 1945 (1963).
79. R. C. Boettner, C. Laird, and A. J. McEvily, TMS-AIME 233, 379 (1965).
80. D. F. Watt, J. D. Embury, and R. K. Ham, Phil. Mag. 17, 199 (1968).
81. V. M. Goritskii, V. S. Ivanova, L. G. Orlov, and V. F. Terent'ev, Sov. Phys. Dokl. 17, 776 (1973).
82. H. Hahn and D. J. Duquette, Acta Met. 26, 279 (1978).
83. N. M. Grinberg and E. N. Aleksenko, translated from Problemy Prochnosti 5, 40 (1977).
84. M. C. Lu and S. Weissmann, Mat. Sci. and Eng'g. 32, 41 (1978).
85. R. B. Davies, Nature 174, 980 (1954).

86. M. S. Paterson, Acta Met. 3, 491 (1955).
87. P. J. E. Forsyth and C. A. Stubbington, J. Inst Met. 80, 181 (1951-52).
88. T. Broom and R. K. Ham, Proc. Roy. Soc. (London), A251, 186 (1959).
89. D. S. Kemsley and M. S. Paterson, Acta Met. 8, 453 (1960).
90. C. E. Feltner, Acta Met. 11, 817 (1963).
91. M. H. Raymond and L. F. Coffin, Acta Met. 11, 801 (1963).
92. T. H. H. Pian and R. D'Amato, "Low-Cycle Fatigue of Notched and Unnotched Specimens of 2024 Al Alloy Under Axial Loading," Wright Air Dev. Center, Tech. Note #58-27 (1958).
93. P. Lukáš and M. Klesnil, Czech. J. Phys. B14, 600 (1964).
94. C. E. Feltner, "A Debris Mechanism of Cyclic Strain Hardening of FCC Metals," Report, Scientific Lab., Ford Motor Co., Dearborn, Mich (1964).
95. V. A. Greenhut, Ph.D. thesis, Rutgers Univ. Coll. of Eng. (1970).
96. C. E. Feltner and R. W. Landgraf, "Selecting Materials to Resist Low Cycle Fatigue," Report, Scientific Lab., Ford Motor Co., Dearborn, Mich (Feb 16, 1969).
97. P. J. E. Forsyth, J. Aust. Inst. Met. 12, 931 (1964).
98. C. Laird and G. Thomas, "On Fatigue-Induced Reversion and Overaging in Dispersion Strengthened Alloy Systems," Ford Motor Co., Dearborn, Mich (Jan 18, 1967).
99. S. Weissmann, A. Shrier, and V. Greenhut, Trans. ASM 59, 709 (1966).
100. S. Weissmann, V. Greenhut, and B. K. Park, Trans. J.I.M. 9, 1004 (1968).
101. J. T. Fourie, Corrosion Fatigue, NACE-2, Houston, Tex. 164 (1972).
102. A. S. Argon, Corrosion Fatigue, NACE-2, Houston, Tex. 176 (1972)
103. Von F. Vitovec, Berg-und-Hüttenmännische Monatshefte 97, 3 (1952).
104. I. R. Kramer, Trans. ASM 62, 521 (1969).
105. I. R. Kramer and A. Kumar, Met. Trans. 3, 1223 (1972).
106. I. R. Kramer, Proc. ICM-II, Boston, Mass., 812 (1976).
107. B. D. Boggs and J. G. Byrne, Met. Trans. 4, 2153 (1973).
108. M. Origima, Trans. Jap. Inst. Metals 10, 182 (1969)
109. D. Broek, "Some Contributions of Electron Fractography to the Theory of Fracture," Report, Nat. Aerospace Lab., The Netherlands, NLR TR 72029 U (1972).
110. K. U. Snowden, Phil. Mag. 14, 1019 (1966).
111. H. Shen, S. Podlaseck, and I. R. Kramer, Acta Met. 14, 341 (1966).

112. H. Shen and I. R. Kramer, Trans. Int. Vac. Met. Conf., 263 (1967).
113. I. R. Kramer and A. Kumar, Corrosion Fatigue, NACE-2, Houston, Tex. 146 (1972).
114. I. R. Kramer, Met. Trans. 5, 1735 (1974).
115. A. N. Stroh, Adv. in Physics, 6, 418 (1957).
116. S. Taira and K. Hayashi, Proc. 9th Jap. Congr. on Testing Materials 1 (1966).
117. S. Taira, K. Tanaka, and T. Tanabe, Proc. 13th Jap. Congr. on Materials Research, 14 (1970).
118. C. Laird and D. J. Duquette, Corrosion Fatigue, NACE-2, Houston, Tex. 12 (1972).
119. O. H. Basquin, Proc. ASTM 10, 625 (1910).
120. L. F. Coffin, Jr., Trans. ASME 76, 931 (1954).
121. S. S. Manson, NACE, Tech Note 2933 (1954).
122. J. Morrow, ASTM STP 378, 45 (1965).
123. J. S. Santner and M. E. Fine, Scripta Met. 11, 159 (1977).
124. F. A. McClintock, A. S. Argon, eds., Mechanical Behavior of Materials, Addison-Wesley, Reading, Mass., 1966, pp. 588-604.
125. P. Watson and T. H. Topper, Exper. Mechanics, p. 11 (Jan 1972).
126. A. Palmgren, "Die Lebensdauer von Kugellagern," ZVD 68, 339 (1924).
127. M. A. Miner, J. Appl. Mech. 12, A-159 (1945).
128. R. P. Haywood, Proc. Colloq. Fatigue, Stockholm, Springer, Berlin, 92-102 (1956).
129. S. Taira, T. Goto, and Y. Nakano, 12th Jap. Congr. on Materials Research, 8 (1969).
130. R. Glocker and E. Osswald, Z. Techn. Phys. 16, 237 (1935).
131. A. L. Christenson and R. S. Rowland, Trans. ASM 45, 638 (1953).
132. C. G. Darwin, Phil. Mag. 27, 675 (1914).
133. B. E. Warren and B. L. Averbach, J. Appl. Phys. 21, 595 (1950).
134. M. S. Paterson, J. Appl. Phys. 23, 499 (1952).
135. W. H. Hall, Proc. Phys. Soc. (London) 62, 741 (1949).
136. W. A. Wood, Phil. Mag. 15, 553 (1933).
137. W. A. Wood, Proc. Phys. Soc. 52, 110 (1940).
138. H. J. Gough and W. A. Wood, Proc. Roy. Soc. A154, 510 (1936).
139. C. S. Barrett, Structure of Metals; Crystallogr. Methods, Principles and Data, 1st Ed., McGraw-Hill, New York, 1943, pp. 363-80.

140. C. S. Barrett, Metals and Alloys 8, 13 (1937).
141. R. G. Spencer and J. W. Marshall, J. Appl. Phys. 12, 191 (1941).
142. J. A. Bennett, J. Research NBS 46, 457 (1951).
143. W. J. Love, "Structural Changes in Ingot Iron Caused by Plastic and Repeated Stressing," Proj. NR-031-005, Dept. T.A.M., Univ. of Illinois (1952).
144. R. J. Hartmann and E. Macherauch, Z. Metallk'de.54, 197 (1963).
145. R. M. N. Pelloux, "The Dislocation Distribution in Face-Centered Cubic Metals After Fatigue," Boeing Scientific Res. Lab., Seattle, Wash., D1-82-0304 (1963).
146. G. Sachs and V. Weiss, Z. Metallk'de. 53, 37 (1962).
147. S. Taira and K. Hayashi, JSTM Jap. 12, 894 (1963).
148. S. Taira and K. Hayashi, 7th Jap. Congr. on Testing Materials 38 (1964).
149. P. B. Hirsch, Acta Cryst. 5, 172 (1952).
150. S. Taira and K. Hayashi, Bull. JSME 9, 627 (1966).
151. K. G. Lynn, C. M. Wan, R. W. Ure, and J. G. Byrne, Phys. Stat. Sol. A22, 731 (1974).
152. L. Handfield, M. N. Bassim, and J. I. Dickson, "Etude de la Deformation Plastique et de la Fatigue du Titane par l'Emission Acoustique, CIM, Montreal, Canada, cited (Aug 1978).
153. C. J. Beevers and M. D. Halliday, Czeck J. Phys. B19, 343 (1969).
154. A. Shrier, J. P. Wallace, J. J. Slade, Jr., and S. Weissmann, Acta Met. 11, 779 (1963).
155. P. B. Hirsch, "Mosaic Structure," Progress in Metal Physics 6, 236 (1956).
156. M. Renninger, Z. Krist. 89, 344 (1934).
157. J. Intrater and S. Weissmann, Acta Cryst. 7, 729 (1954).
158. A. J. Reis, J. J. Slade, Jr., and S. Weissmann, J. Appl. Phys. 22, 665 (1951).
159. J. J. Slade, Jr., and S. Weissman, J. Appl. Phys. 23, 323 (1952).
160. S. Weissmann and D. L. Evans, Acta Cryst. 7, 733 (1954).
161. S. Weissmann, J. Appl. Phys. 27, 389 (1956).
162. S. Weissmann, L. A. Gorman, and L. Zwell, J. Appl. Phys. 33, 3131 (1962).

163. S. Weissmann, J. Appl. Phys. 27, 1335 (1956).

164. F. Garofalo, L. Zwell, A. S. Keh, and S. Weissmann, Acta Met. 9, 721 (1961).

165. R. Strickler and G. R. Booker, "TEM Investigation of Removal of Mech. Polishing Damage by Chem. Polishing," Scientific Paper 63-148-546-P5, Westinghouse Res. Labs., Pittsburgh, Pa. (1963).

166. ASTM Standards, Part 31, Philadelphia, Pa., (1965), p. 222.

167. S. Weissmann, "Lattice Inhomogeneities and Substructures in Crystalline Materials," Eng'g. Res. Bull. #39, Rutgers Univ. Coll. of Eng. (1956).

168. L. F. Vassamillet and R. Smoluchowski, J. Appl. Phys. 30, 418 (1959).

169. G. K. Williamson and W. H. Hall, Acta Met. 1, 22 (1958).

170. A. Cottrell, Dislocations and Plastic Flow, Clarendon Press, Oxford (1953).

171. G. I. Belykh, G. M. Pyatigorskiĭ, and E. I. Raĭkhel's, Sov. Phys. Sol. St. 18, 161 (1976).

172. W. Hayden, W. G. Moffett, and John Wulff, The Structure and Properties of Materials, Vol. III, "Mechanical Behavior," John Wiley and Sons, New York, 1965, pp. 123-29.

173. A. S. Keh and S. Weissmann, Electron Microscopy and Strength of Materials, John Wiley and Sons, New York, 1963, p. 231.

174. G. I. Taylor, Proc. Roy. Soc. A145, 388 (1934).

175. J. Friedel, Dislocations, Pergamon Press, New York, 1967, p. 273.

176. N. H. Polakowski and E. J. Ripling, Strength and Structure of Engineering Materials, Prentice Hall, Englewood Cliffs, N. J., 1966, pp. 494-500.

INITIAL DISTRIBUTION

Copies	
2	CNR 1 Code 465 1 Code 471
4	NRL 1 Code 6300 1 Code 6311 1 Code 6380 1 Code 6385
2	NAVAIR (AIR 320)
1	Naval Air Development Center Naval Materials Center Warminste, PA 18974 Attn: Dr. F.W. Williams (Code 606)
5	NAVSEA 1 SEA 035 1 SEA 05D 1 SEA 323 2 SEA 99612
12	DTIC
1	Air Force Materials Laboratory Wright-Patterson AF Base Dayton, OH 45433 (Attn: Dr. H. Burte)
1	National Bureau of Standards Washington, DC 20234 (Attn: Dr. Jerome Kruger)
1	Case Western Reserve Mechanical and Aerospace Engineering Cleveland, OH 44106 (Attn: S.S. Manson)
1	University of Connecticut Storrs, CT 06268 (Attn: Dr. A.J. Evily)
2	Johns Hopkins University School of Engineering Baltimore, MD 21218 (Attn: Dr. R. Green, R. Pond)

Copies	
1	Lehigh University 327 Sinclair Lab., Bldg 7 Bethlehem, PA 18015 (Attn: Dr. R.P. Wei)
1	University of Maryland Dept. of Chemical Eng. College Park, MD 20740 (Attn: Dr. R. Arsenault)
3	Massachusetts Institute of Technology Cambridge, MA 02139 (Attn: Dr. R. Latanison) Dr. N. Saka Dr. M. Cohen
1	Northwestern University Evanston, IL 60201 (Attn: Dr. J.B. Cohen)
1	Ohio State University Met. Engr. Dept. 116 W. 19th Avenue Columbus, OH 43210 (Attn: John P. Hirth)
1	Polytechnic Inst of New York 333 Jay Street Brooklyn, NY 11201 (Attn: Dr. H. Margolin)
1	Renssalaer Polytechnic Inst Troy, NY 12181 (Attn: Dr. D.J. Duquette)
1	University of Rochester Dept. of Mechanical Engr. Rochester, NY 14627 (Attn: Dr. James C. Li)
10	Rutgers University Piscataway, NJ 08854 (Attn: Dr. W. Weissmann)

Copies		CENTER DISTRIBUTION	
		Copies	Code
2	Syracuse University Link Hall Syracuse, NY 13210 (Attn: Dr. Y. Oshida) Dr. Volker Weise	2	012
		2	17
1	University of Virginia Dept. of Applied Sciences Charlottsville, VA 22904 (Attn: Dr. D. K. Wilsdorf)	1	28
		1	280
		15	2802
1	Ford Motor Company Central Research Lab. Detroit, Michigan 48226 (Attn: J.J. Harwood)	2	281
		6	282
		10	5211.1 Rept Dist
		1	522.1 Library (C)
		1	522.2 Library (A)
		2	5231 Office Services

